A NUMERICAL INVESTIGATION OF THE GLOBAL STABILITY OF SHIP ROLL: INVARIANT MANIFOLDS, MELNIKOV'S METHOD, AND TRANSIENT BASINS

by

Marc Alan Kreider

Thesis submitted to the Faculty of the

Virginia Polytechnic Institute and State University

in partial fulfillment of the requirements for the degree of

Master of Science

in

Engineering Mechanics

APPROVED:

Ali H. Nayfeh, Chairman

Scott L. Hendricks

Dean T. Mook

July 1992

Blacksburg, Virginia

C.2

A NUMERICAL INVESTIGATION OF THE GLOBAL STABILITY OF SHIP ROLL: INVARIANT MANIFOLDS, MELNIKOV'S METHOD, AND TRANSIENT BASINS

by

Marc Alan Kreider

Ali H. Nayfeh, Chairman

Engineering Mechanics

(ABSTRACT)

A parametrically forced, single-degree-of-freedom equation modelling ship roll is investigated through the numerical study of invariant manifolds, Melnikov's method, and transient basins. The calculation of the manifolds is facilitated through the development of a sophisticated algorithm for approximating the locations of the saddle points of the Poincaré map. For selected fixed values of the restoring-moment and damping parameters (the "base case"), the manifolds of the saddles of the Poincaré map are repeatedly computed for increasingly higher excitation amplitudes until homoclinic, heteroclinic, and mixed manifold intersections are observed. The critical amplitudes at which these tangles first occur are accurately predicted by Melnikov's method, verifying its viability as a tool for analyzing ship roll. Corresponding transient basins indicate that fractally mixed regions of stable and unstable initial conditions appear with the onset of transverse manifold intersections. For parametric forcing, the fractal areas are symmetric about the origin and do not significantly affect the integrity of the safe region near the origin. Test cases involving external or combined external-plus-parametric excitation result in asymmetric transient basins and, following the appearance of manifold tangling, a catastrophic reduction of the safe area. Lastly, Melnikov's method is used to perform a parameter study that indicates the effects of varying the restoring-moment and damping coefficients on the critical excitation level.

Acknowledgements

Over the two years spanned by this research, many people have earned my gratitude and thanks. My advisor, Dr. Ali H. Nayfeh, is due my appreciation for providing the initial direction for the project and a wealth of essential nonlinear-dynamics background, as well as considerable financial support. I also want to thank Dr. Dean T. Mook and Dr. Scott L. Hendricks for donating the time required to be members of my committee. Special thanks to Dr. Marwan Bikdash for his technical assistance in solving the frustrating saddle-point problem, for his general mathematical expertise, and for his writing reviews, not to mention the late-night company. Dr. Balakumar Balachandran also added numerous insights during the project, particularly regarding transient basins. I should not leave out Dr. Ashraf Abou-Rayan for his help with the analog computer (unfortunately not of use here!), the invaluable assistance of Kyoyul Oh, who generously donated much of his time as the system manager for our Apollo workstation, or Tony Anderson for his help with Dataplot. Also deserving my gratitude is Ms. Sally Shrader for her kindness and willingness to help with almost anything. On a less technical note, I express thanks to my other friends in the department, including Sarah Whitlock, Mahmood Tabaddor, Keith Yates, Erik Panzer, and my brother Wayne. Last, but certainly not least are my parents, who have continually given their love and encouragement throughout my academic career. (This research was sponsored in large part by the Office of Naval Research under contract # N00014-90-J-1149.)

Table of Contents

1. Introduction **1**

1.1 History of the Ship-Roll Problem 2

1.1.1 The Roll Equation 2

1.1.2 Invariant Manifolds, Melnikov's Method, and Transient Basins 5

1.2 Methodology 6

1.2.1 Scope 6

1.2.2 Contributions 7

2. The Single-Degree-of-Freedom Roll Equation **9**

2.1 Formulation 9

2.2 Elementary Dynamics Techniques 17

2.2.1 State-Space Form 17

2.2.2 The Phase Plane 19

2.2.2.1 Fixed Points 19

2.2.2.2 Separatrices 25

3. Invariant Manifolds in the Poincaré Section **26**

3.1 Background: Poincaré Maps, Limit Sets, Manifolds 26
3.2 Utility of Invariant Manifolds 30
3.3 Numerical Computation of Manifolds 32
3.3.1 Linearized Approximations to the Saddle Points 32
3.3.2 Refined Saddle-Point Approximation: Hooke-Jeeves Algorithm 34
3.3.2.1 Standard Algorithm 34
3.3.2.2 Additions to the Standard Algorithm 36
3.3.2.3 Multiple Approximations 39
3.3.3 Manifold Generation 43
3.3.4 Computed Manifolds: Examples 45

4. Application of Melnikov's Method 48
4.1 Derivation of the Melnikov Function 49
4.2 Calculation of the Melnikov Function 57
4.2.1 Homoclinic Tangles 57
4.2.2 Heteroclinic Tangles 58
4.2.3 Mixed Tangles 60
4.3 Examples of Melnikov Computations 63

5. Results for the Ship-Roll Model 66
5.1 Base Case 67
5.1.1 Determination of Parameter Values 67
5.1.2 Invariant Manifold Computation (Base Case) 69
5.1.3 Melnikov Analysis (Base Case) 77
5.1.4 Transient-Basin Analysis (Base Case) 83
5.1.4.1 Appearance of Fractal Geometry 83
5.1.4.2 Stability Implications for Ship Roll 95
5.2 Parameter Study 101

5.2.1 Base-Case Values 103
5.2.2 Low Values 108
5.2.3 High Values 113
5.2.4 Verification of Parameter Study 113

6. Review and Conclusion 122
6.1 Results and Implications 123
6.2 Recommendations for Further Study 125

References 127

Appendix A. Saddle-Point Algorithm: Pseudo-Code 130
Main Program 131
Subroutine ITERATE 132
Subroutine INTLZ 134
Subroutine HJ 135

Vita 137

List of Illustrations

Figure 2.1. Degrees of Freedom of a Ship 10
Figure 2.2. The 3-2-1 Euler-Angle Sequence 12
Figure 2.3. Simple Mass-Spring System 20
Figure 2.4. Phase Plane for Harmonic Oscillator 21
Figure 2.5. Conservative Phase Portrait for the Ship-Roll Model 22
Figure 2.6. Damped, Unforced Phase Portrait for the Ship-Roll Model 23
Figure 3.1. Definition of the Poincaré Section 27
Figure 3.2. Manifolds of the Roll Equation 29
Figure 3.3. Schematic of a Transverse Manifold Intersection 31
Figure 3.4. The Hooke-Jeeves Algorithm 37
Figure 3.5. Phase Space Near a Saddle Point 40
Figure 3.6. Possible Displacements for an Iterate of the Poincaré Map 41
Figure 3.7. Parker and Chua's Algorithm 44
Figure 3.8. Invariant Manifolds: Test Case ($F = 0.11$) 46
Figure 3.9. Invariant Manifolds: Test Case ($F = 0.19$) 47
Figure 4.1. Unperturbed Invariant Manifold 51
Figure 4.2. Manifolds in the Poincaré Section 52
Figure 4.3. Time-Dependent Distance Function 53
Figure 4.4. Approximate Homoclinic Trajectory 59
Figure 4.5. Approximate Heteroclinic Trajectories 61
Figure 4.6. Unperturbed Trajectory Used for Predicting Mixed Tangles 62

Figure 4.7. Melnikov Function for the Duffing Equation (F = 0.19) 64
Figure 4.8. Melnikov Function for the Duffing Equation (F = 0.11) 65
Figure 5.1. Manifolds without Transverse Intersections 70
Figure 5.2. Manifolds with Pending Homoclinic Intersections 71
Figure 5.3. Onset of Homoclinic Intersections in the Manifolds 72
Figure 5.4. Well-Developed Homoclinic Manifold Intersections 73
Figure 5.5. Onset of Mixed Manifold Intersections 75
Figure 5.6. Onset of Heteroclinic Manifold Intersections 76
Figure 5.7. Homoclinic Melnikov Function (h = 0.05) 78
Figure 5.8. Homoclinic Melnikov Function (h = 0.08) 79
Figure 5.9. Homoclinic Melnikov Function (h = 0.085) 80
Figure 5.10. Heteroclinic Melnikov Function (h = 0.32) 81
Figure 5.11. Heteroclinic Melnikov Function (h = 0.34) 82
Figure 5.12. Mixed Melnikov Function (h = 0.21) 84
Figure 5.13. Mixed Melnikov Function (h = 0.215) 85
Figure 5.14. Homoclinic Transient Basin (Base Case, h = 0.07) 88
Figure 5.15. Homoclinic Transient Basin (Base Case, h = 0.09) 89
Figure 5.16. Heteroclinic Transient Basin (Base Case, h = 0.25) 90
Figure 5.17. Heteroclinic Transient Basin (Base Case, h = 0.32) 91
Figure 5.18. Heteroclinic Transient Basin (Base Case, h = 0.35) 92
Figure 5.19. Heteroclinic Transient Basin (Base Case, h = 0.50) 93
Figure 5.20. Heteroclinic Transient Basin (Base Case, h = 2.00) 94
Figure 5.21. Manifolds for External Forcing (Base Case, h = 0.23) 97
Figure 5.22. Transient Basin for External Forcing (Base Case, h = 0.23) 98
Figure 5.23. Transient Basin for External Forcing (Base Case, h = 0.30) 99
Figure 5.24. Transient Basin for External Forcing (Base Case, h = 0.40) 100
Figure 5.25. Transient Basin for Combined Forcing (Base Case, h(e) = 0.20 and h(p) = 0.25) 102
Figure 5.26. Effect of the Cubic Restoring-Moment Coefficient (BC) 104

Figure 5.27. Effect of the Quintic Restoring-Moment Coefficient (BC) 105
Figure 5.28. Effect of the Linear Damping Coefficient (BC) 106
Figure 5.29. Effect of the Cubic Damping Coefficient (BC) 107
Figure 5.30. Effect of the Cubic Restoring-Moment Coefficient (LOW) 109
Figure 5.31. Effect of the Quintic Restoring-Moment Coefficient (LOW) 110
Figure 5.32. Effect of the Linear Damping Coefficient (LOW) 111
Figure 5.33. Effect of the Cubic Damping Coefficient (LOW) 112
Figure 5.34. Effect of the Cubic Restoring-Moment Coefficient (HIGH) 114
Figure 5.35. Effect of the Quintic Restoring-Moment Coefficient (HIGH) 115
Figure 5.36. Effect of the Linear Damping Coefficient (HIGH) 116
Figure 5.37. Effect of the Cubic Damping Coefficient (HIGH) 117
Figure 5.38. Heteroclinic Transient Basin (Low Values, h = 0.15) 118
Figure 5.39. Heteroclinic Transient Basin (Low Values, h = 0.18) 119
Figure 5.40. Heteroclinic Transient Basin (High Values, h = 0.73) 120
Figure 5.41. Heteroclinic Transient Basin (High Values, h = 0.77) 121

1. Introduction

For a number of decades, the motion of sea vessels has sparked increasing interest among mathematicians, scientists, and engineers. The general problem of precisely describing the motion of a ship under the influence of a realistic sea involves a complex and dynamically rich system. An important part of solving this problem consists of predicting when large-amplitude motions or even capsize will occur. Such knowledge would be an aid to naval architects, who could then design vessels not capable of producing unwanted responses.

As a step toward preventing ship capsize, this thesis has two primary goals. The first is the development of robust numerical routines that compute invariant manifolds and employ Melnikov's criterion, both useful in the global-stability analysis of many dynamic phenomena, including ship roll. The second is the application of these routines, together with the concept of what are called "transient basins," to a single-degree-of-freedom equation modelling the roll of a ship subjected to the periodic forcing of ocean waves. In the process, the accuracy of Melnikov's method is verified, leading to an investigation of the effects of varying the parameters of the roll equation on ship stability. The following sections comprise a background of the ship-roll problem and a detailed explanation of the methodology employed in the current research.

1.1 History of the Ship-Roll Problem

1.1.1 The Roll Equation

Modelling the roll of ships dates at least back to Euler in the 18th century. Making several simplifying restrictions, such as still water, Euler reduced the equation of motion to the form that describes a simple pendulum. Gradual advances climaxed with Froude's theory of a rolling vessel in a seaway (Froude [1861]), which was later "recognized as a classic" (Blagoveshchensky [1962]).

Although the motion of an unconstrained rigid body such as a ship is fully described by a system of six differential equations, early researchers assumed that roll could be modelled with a single equation. This practice has endured; current researchers generally model ship roll with the equation

$$\ddot{\phi} + G(\dot{\phi}) + F(\phi) = H(\phi,t) \qquad [1.1]$$

where

ϕ = roll angle

$F(\phi)$ = restoring moment

$G(\dot{\phi})$ = damping

$H(\phi,t)$ = excitation

The restoring moment depends primarily on ship geometry; in the earliest models, it was also assumed to depend linearly on the roll angle. More recently, however, the use of nonlinear terms in $F(\phi)$ has become widespread. Wright and Marshfield [1980] published results showing that a cubic nonlinearity in the restoring moment yields predictions of steady-state solutions that compare "reasonably well" with experimental data. Several years later, Nayfeh and Khdeir [1986a]

demonstrated an improved predictive capacity with the addition of a quintic term to the model of the restoring moment.

The roll-damping term $G(\dot{\phi})$ can be attributed mostly to two causes: frictional interaction between water and the ship hull and pressure changes generated by eddies formed by the hull and bilge keels (Myrhaug [1981]). The mathematical form of this term has been studied extensively, beginning with a model devised by Froude and used for more than a century (Haddara [1984]). A typical expression for this model, known commonly as a linear-plus-quadratic damping model (LPQD), is

$$G(\dot{\phi}) = \mu_1\dot{\phi} + \mu_2\dot{\phi}\,|\,\dot{\phi}\,| \qquad [1.2]$$

For mathematical convenience, a number of researchers replace the quadratic term with a cubic one ($\mu_3\dot{\phi}^3$), resulting in a linear-plus-cubic damping model (LPCD). In using what he calls a "functional series approach to rolling," Dalzell [1978] instituted the LPCD model, obtaining analytic predictions that fit experimental observations "about as well as (sometimes better than) the linear-plus-quadratic model." Haddara [1984] drew a similar conclusion, stating that "within the range and scatter of available data, damping form has little or no effect on the [analytically predicted] rolling response." At the present time, investigators are using both models largely because no one has established a theoretical basis for preferring one model over the other.

Ship-roll dynamicists have also considered different possibilities for the functional form of the excitation function $H(\phi,t)$. Although a realistic sea would perhaps be adequately modelled with a truncated Fourier series (in which the various amplitudes and frequencies represent different wave shapes), most contemporary researchers for convenience select a single sinusoidal function. If the sinusoid multiplies the roll angle or the roll velocity, the excitation is called parametric; otherwise it is termed external. Physically, external forcing arises from a regular wave train impacting the ship broadside (a "beam sea"). In contrast, parametric excitation can be the result of nonlinear heave-roll or pitch-roll coupling in the original system of differential equations of motion (Tondl and Nabergoj [1990]). A second cause of parametric forcing is the time-varying behavior of the

metacentric height (a distance depending on the center of gravity and the location of the resultant buoyancy force (Rawson and Tupper [1976])), especially in longitudinal seas.

Recent research on the single-degree-of-freedom roll equation has included the effects of both types of excitation. Wright and Marshfield [1980] used both analytical and experimental methods to study the effects of external forcing. Nayfeh and Khdeir [1986a] employed sophisticated perturbation methods to produce quite accurate analytical solutions to an externally forced roll equation of a similar form, yielding a qualitative description of roll behavior. They extended their work by including a nonzero bias angle in the governing roll equation (Nayfeh and Khdeir [1986b]). In his dissertation, Falzarano [1990] used several analytical and geometric methods to study externally forced ship roll.

A number of other papers have focused on parametric excitation. Paulling and Rosenberg [1959] developed mathematical representations of the heave-roll and pitch-roll couplings that can generate parametric forcing. A short time later, Paulling [1961] modelled parametrically excited roll due to a longitudinal sea. An extension of this research (Paulling, Kastner, and Schaffran [1972]) comprised a purely experimental approach to both longitudinal and quartering seas as they pertain to ship roll. Eventually, parametric forcing was applied to a single-degree-of-freedom ship-roll equation; one example is found in the work of Blocki [1980], who derived an equation of this form in detail. Further research includes that of Féat and Jones [1981], who carried out a generalized theoretical analysis of stability in the presence of parametric excitation. Sánchez [1989] and Sánchez and Nayfeh [1990] applied perturbation techniques and Floquet theory to generate a qualitative description of roll and roll stability for a parametrically forced model. Another, somewhat different approach was employed by Tondl and Nabergoj [1990], who modelled ship roll with simple mechanical models consisting of rigid rods, springs, and dashpots. The great variety of approaches sampled here has probably occurred because the range of conditions for which each of the studies is valid has yet to be concretely established experimentally.

1.1.2 Invariant Manifolds, Melnikov's Method, and Transient Basins

Many of the techniques mentioned in the last section provide solutions to particular problems related to ship roll. However, few of them yield much information on the global stability of the ship (i.e., the stability of a ship for a wide range of initial conditions). An analytical tool that does provide global-stability characteristics is the study of *invariant manifolds*. The transverse intersection of these special curves indicates that the division between regions of stable and unstable initial conditions in the corresponding transient basin has been transformed from a continuous curve to a fractal boundary. In addition, the stable region of the transient basin may begin to erode, meaning that a smaller area of initial conditions can be considered safe from capsize. However, computing invariant manifolds is computationally expensive. In order to avoid this inconvenience, a perturbation technique known as Melnikov's method may be used to estimate when manifold intersections begin to occur.

Melnikov [1963] developed his technique almost 30 years ago, but many applications of his method have appeared quite recently. Li and Moon [1990] used it to develop a criterion for manifold intersections for a three-well potential oscillator governed by an equation similar to the much-used ship roll equation. Falzarano [1990] and Falzarano and Troesch [1990] examined invariant manifold intersections and also used Melnikov's method to analyze a ship with a cubic restoring moment.

Analysis of transient basins provides directly the stability information implied by the other two methods. The procedure consists of calculating the trajectories associated with a large number of initial conditions in a selected region of the phase space and labelling each as stable or unstable according to a predetermined criterion. The size and shape of the "safe" (stable) area is useful in describing the global stability of the system. Thompson, Rainey, and Soliman [1990] and Thompson [1991] have recently employed transient-basin analysis to study a ship-roll model possessing a quadratic restoring moment and linear damping.

1.2 Methodology

1.2.1 Scope

The most general ship-dynamics problem involves an excitation caused by a realistic sea, meaning that random, unpredictable factors must be taken into account before the problem is fully defined (e.g., Roberts [1982]). Models of such a sea might include a superposition of periodic terms (representing waves of differing lengths and amplitudes) as well as stochastic excitation. Moreover, a complete description of rigid-body ship motion must incorporate six degrees of freedom: three translational displacements (usually surge, sway, and heave) and three rotational displacements (usually roll, pitch, and yaw). Without any restrictions, the six governing equations are coupled, meaning that roll is potentially influenced by the five remaining degrees of freedom (Falzarano and Troesch [1990]).

Barring any simplifications, the general case described above must almost always be treated with purely numerical techniques. For instance, a specific ship in a given sea may be analyzed for a given set of initial conditions by numerically integrating the system of six equations of motion. While this procedure yields a prediction of what might occur for that one situation (e.g., acceptable stable motion or capsize), little insight into the global-stability characteristics of the dynamic system is gained by examining only isolated cases (Wright and Marshfield [1980]).

The analytical methods that provide this global information (e.g., invariant manifolds, Melnikov's method, transient basins) are difficult if not impossible to apply to the general case. As a consequence, the problem of a ship moving in a realistic sea is in this thesis modelled roughly with the single-degree-of-freedom roll equation introduced in the last section. The restoring moment is approximated with an odd, quintic polynomial, and the damping is modelled with the LPCD function. With the exception of a brief analysis in Chapter 5, only parametric excitation is considered.

1.2.2 Contributions

The broad goal underlying this research is the prevention of vessel capsize. Analysis of the restricted model defined by the single-degree-of-freedom equation is an indirect means to that goal. Nevertheless, the study of invariant manifolds and use of Melnikov's method and transient basins in the context of such a model provides global-stability features not available for the more complete model associated with the six-dimensional system. Thus, it is hoped that the work undertaken here will prove helpful as a tool for others seeking to improve the predictive value of the single-degree-of-freedom equation. The main contributions of this thesis include the following:

- the development of a FORTRAN algorithm for accurately approximating the saddle points of a Poincaré map, which are used in calculating invariant manifolds

- a partial validation of Melnikov's method for predicting homoclinic, heteroclinic, and mixed homoclinic-heteroclinic manifold intersections

- a detailed study of the parametrically forced ship-roll model through transient-basin analysis

- a parameter study (facilitated by Melnikov's method) that revealed the individual effects of the restoring-moment and damping coefficients on critical excitation amplitude

The remaining chapters chronicle the development of these advances. In Chapter 2, the specific form of the single-degree-of-freedom ship-roll equation is derived and discussed. The first part of Chapter 3 includes an introduction to invariant manifolds and an explanation of the significance of transverse manifold intersections. The latter portion of the chapter contains the algorithm used to locate acceptable saddle-point approximations and a brief discussion of Parker and Chua's algorithm, which is employed to generate the manifolds. Chapter 4 is an in-depth exposition of Melnikov's method. Due to the complexity of the mathematics, a derivation of the Melnikov function introduces the topic. The method is then applied to the ship-roll equation

developed in Chapter 2, with attention to homoclinic, heteroclinic, and mixed manifold intersections. Chapter 5 includes results for the ship-roll model. For a selected set of parameter values (the "base case"), invariant manifolds are calculated, Melnikov's method is used to predict transverse manifold intersections, and transient basins are computed. The symmetric nature of the transient basins warranted a brief examination of external and combined external-plus-parametric excitation. Lastly, the base-case values were varied in such a way that the individual effects of the restoring-moment and damping coefficients could be determined. The final chapter contains a summary of the results and their implications as well as some suggestions for related future work.

2. The Single-Degree-of-Freedom Roll Equation

The purpose of this chapter is twofold. First, the single-degree-of-freedom roll equation is derived from the original system of six differential equations that describe any rigid body in motion. Second, some elementary dynamics techniques are applied to the roll equation to provide a foundation for the invariant-manifold and Melnikov analyses undertaken in Chapters 3 and 4.

2.1 Formulation

The unconstrained rigid-body motion of a ship is fully described by six degrees of freedom, which usually consist of three translational displacements and three angular displacements. For convenience, the displacements are often replaced by their corresponding velocities in the governing equations of motion. The standard set of three translational velocities and three angular velocities is depicted in Figure 2.1. These six variables are specified in a body-fixed coordinate system, meaning that the heave velocity, for example, is not necessarily vertical because the ship may take on an arbitrary orientation. The body-fixed coordinates, like the variables, are selected to reduce the complexity of the equations of motion.

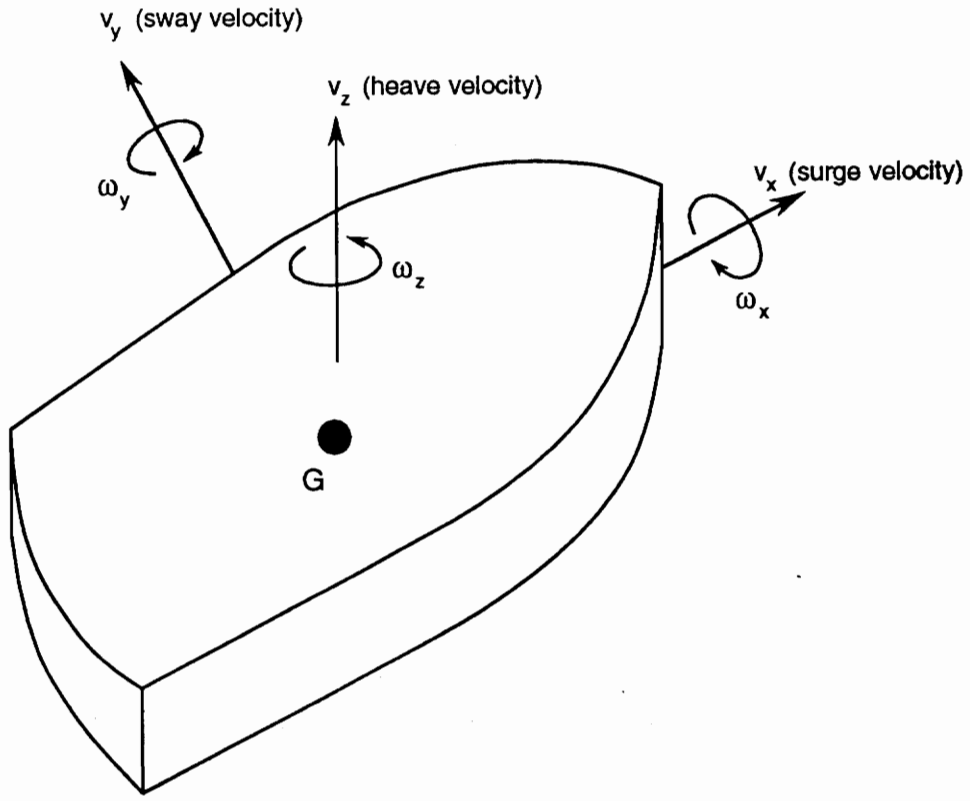

Figure 2.1. Degrees of Freedom of a Ship: Labelled on the schematic of a ship are three translational velocities (v_x, v_y, v_z) and three angular velocities (ω_x, ω_y, ω_z) in body-fixed coordinates (originating at the center of mass, G). These six variables fully describe the motion.

The variable of primary interest, roll (ϕ), is not pictured in the figure because the roll in general is not a rotation about any of the body-fixed axes, but rather one of three Euler angles. Euler angles are a sequence of specified angular displacements from an initial orientation. Their time derivatives can be related to the body-fixed angular velocities (ω_x, ω_y, ω_z); after integration of this relationship, the body-fixed coordinates are related to the original inertial coordinates, orienting the ship. Since finite rotations do not commute, the chosen sequence of angles affects the form of the relationship. The Euler-angle set selected here is yaw-pitch-roll ($\psi - \theta - \phi$), a 3-2-1 sequence. This means that successive rotations are executed about the initial z-axis, the new y-axis, and then the new x-axis. The three rotations are shown graphically in Figure 2.2. The Euler-angle equations in this case have the following form:

$$\omega_x = \dot{\phi} - \dot{\psi} \sin\theta \qquad [2.1]$$

$$\omega_y = \dot{\theta} \cos\phi + \dot{\psi} \cos\theta \sin\phi \qquad [2.2]$$

$$\omega_z = -\dot{\theta} \sin\phi + \dot{\psi} \cos\theta \cos\phi \qquad [2.3]$$

Derivations of Euler-angle equations appear in many dynamics references (e.g., Kane, Likins, and Levinson [1983]).

The six-degree-of-freedom equations of motion for a ship can be written with the use of a straightforward Newtonian approach; a number of researchers, including Abkowitz [1964], have derived the general form. Here, we choose to put the equations of motion in a form resembling that used by Falzarano [1990]:

$$m(\dot{v}_x + \omega_y v_z - \omega_z v_y - x_G(\omega_y^2 + \omega_z^2) + z_G(\omega_x\omega_z + \dot{\omega}_y)) = F_x \qquad [2.4]$$

$$m(\dot{v}_y + \omega_z v_x - \omega_x v_z + x_G(\omega_x\omega_y + \dot{\omega}_z) + z_G(\omega_y\omega_z - \dot{\omega}_x)) = F_y \qquad [2.5]$$

$$m(\dot{v}_z + \omega_x v_y - \omega_y v_x + x_G(\omega_z\omega_x - \dot{\omega}_y) - z_G(\omega_x^2 + \omega_y^2)) = F_z \qquad [2.6]$$

$$I_{xx}\dot{\omega}_x - (I_{yy} - I_{zz})\omega_y\omega_z - I_{zx}(\dot{\omega}_z + \omega_x\omega_y) - mz_G(\dot{v}_y + \omega_z v_x - \omega_x v_z) = M_x \qquad [2.7]$$

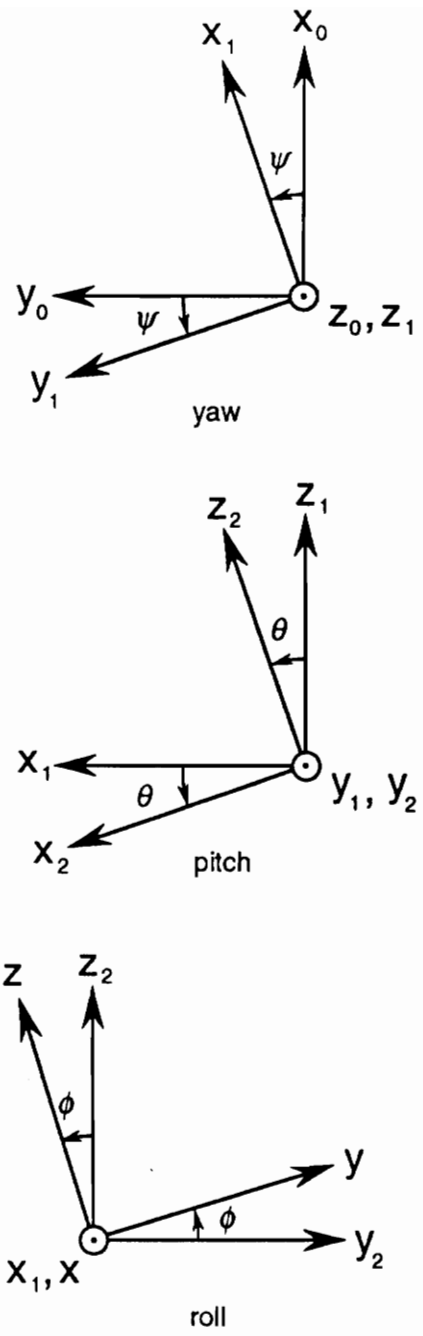

Figure 2.2. The 3-2-1 Euler-Angle Sequence: Pictured are the three successive rotations (yaw, pitch, roll) that produce the body-fixed (x-y-z) system from an inertial (x_0-y_0-z_0) system, in which x_0 and y_0 are horizontal and z_0 is vertical.

$$I_{yy}\dot{\omega}_y - (I_{zz} - I_{xx})\omega_z\omega_x - I_{zx}(\omega_z^2 - \omega_x^2) + mz_G(\dot{v}_x + \omega_y v_z - \omega_z v_y)$$

$$- mx_G(\dot{v}_z + \omega_x v_y - \omega_y v_x) = M_y \qquad [2.8]$$

$$I_{zz}\dot{\omega}_z - (I_{xx} - I_{yy})\omega_x\omega_y - I_{zx}(\dot{\omega}_x - \omega_y\omega_z) + mx_G(\dot{v}_y + \omega_z v_x - \omega_x v_z) = M_z \qquad [2.9]$$

where

m = mass of the ship

x, y, z = body-fixed coordinate system; displacements along these directions

I_{xx}, I_{yy}, I_{zz} = moments of inertia of the ship in the body-fixed system

I_{xy}, I_{yz}, I_{zx} = products of inertia of the ship in the body-fixed system

x_G, y_G, z_G = coordinates of the center of mass of the ship in the body-fixed system

v_x, v_y, v_z = translational velocities in the body-fixed system

$\omega_x, \omega_y, \omega_z$ = angular velocities in the body-fixed system

F_x, F_y, F_z = components of the resultant external force in the body-fixed system

M_x, M_y, M_z = components of the resultant external moment in the body-fixed system

The most direct approach to analyzing the governing system consists of numerically solving the equations of motion and the Euler-angle equations simultaneously, resulting in the angular orientation of the ship. This solution would yield a correct response for the completely arbitrary motion of a ship to the extent that the force and moment terms can be represented accurately. However, because the solution to the governing equations must be obtained numerically, only one specific ship under the action of one particular sea could be analyzed at a time. The computation involved in such an enterprise is substantial, and general dynamical trends could only be discovered by selecting, with few guidelines, a large number of different cases.

Applying knowledge of typical, realistic ship motions in order to simplify the governing system is a preferable alternative. To accomplish this goal, we examine the procedure employed in the

work of Blocki [1980]. The surge, sway, and yaw are taken to be $O(\delta^2)$, or the order of δ^2, where $\delta \ll 1$. The heave and pitch are constrained to be $O(\delta)$, while the roll is allowed to be even larger ($O(1)$). The same ordering applies to the the first and second time derivatives of these variables. Then the surge, sway, and yaw are set equal to zero, since they usually have little bearing on ship stability. In addition, the origin of the x-y-z coordinate system is selected to coincide with the center of mass, G. Lastly, only ships that have a plane of approximate symmetry coincident with the x-z plane are considered, meaning that the product of inertia I_{zx} is nearly zero. With these restrictions, the remaining nontrivial equations of motion, Equations [2.6-2.8], become

$$m\dot{v}_z = F_z \qquad [2.10]$$

$$I_{xx}\dot{\omega}_x - (I_{yy} - I_{zz})\omega_y\omega_z = M_x \qquad [2.11]$$

$$I_{yy}\dot{\omega}_y - (I_{zz} - I_{xx})\omega_z\omega_x = M_y \qquad [2.12]$$

Substituting two-term Taylor expansions of the Euler-angle relationships (Equations [2.1-2.3]) into the modified equations of motion, [2.10-2.12], and keeping only terms $O(\delta)$ or larger results in

$$m\ddot{z} = F_z \qquad [2.13]$$

$$I_{xx}\ddot{\phi} = M_x \qquad [2.14]$$

$$I_{yy}\ddot{\theta} = -I_{yy}\left(\frac{1}{2}\ddot{\theta}\phi^2 + \theta\phi\dot{\phi}\right) + (I_{zz} - I_{xx})\dot{\theta}\dot{\phi}\left(\phi - \frac{1}{6}\phi^3\right) = M_y \qquad [2.15]$$

The external force and moments in Equations [2.13-2.15] may be written as functions of the displacements, their derivatives, and time. The details of this development are somewhat laborious and not crucial for our purposes; they are consequently omitted. The interested reader should consult Blocki [1980]. If it is further assumed that the pitch angle is negligible, then the following system of differential equations representing coupled heave-roll motions may be written as

$$\ddot{z} + 2\delta_z \dot{z} + \omega_z{}^2 z = \overline{Z}(t) \qquad [2.16]$$

$$\ddot{\phi} + 2\delta_\phi(1 + \frac{e_1}{\omega_\phi{}^2}\dot{\phi}^2 + ...)\dot{\phi} + \omega_\phi{}^2(1 - \varepsilon_1\phi^2 - \varepsilon_2\phi^4 - ...)\phi - \frac{1}{2}K_{\phi z}\phi z = \overline{K}(t) \qquad [2.17]$$

where

$e_1, ...$ = dimensionless coefficients of nonlinear damping

$\varepsilon_1, \varepsilon_2, ...$ = dimensionless coefficients of nonlinear stiffness

$\delta_\phi, \omega_\phi{}^2$ = dimensional scaling coefficients

$K_{\phi z}$ = coefficient of static heave-roll coupling

$\overline{Z}(t)$ = excitation of heave (assumed to be harmonic)

$\overline{K}(t)$ = external excitation of roll

The first of the pair is uncoupled from roll and may be solved and substituted into the second. The coefficients of each term are redefined for convenience, resulting in the simplified form

$$\ddot{\phi} + \omega_0{}^2\phi + \alpha_3\phi^3 + \alpha_5\phi^5 + \mu_1\dot{\phi} + \mu_3\dot{\phi}^3 + h\phi\cos(\Omega t) = \overline{K}(t) \qquad [2.18]$$

Thus, one form of the single-degree-of-freedom model discussed in the first chapter has been derived. Note that the $h\phi\cos(\Omega t)$ term represents parametric forcing, which in this case is caused by coupling of heave and roll. The term on the right side, $\overline{K}(t)$, represents an external excitation. As was mentioned earlier, the linear-plus-cubic damping model and an odd, quintic polynomial for the restoring moment are chosen; other terms are dropped.

Before proceeding to analyze Equation [2.18], we should review the assumptions that allowed us to derive this model of ship rolling:

- Surge, sway, and yaw are negligible.

- Pitch and heave can be appreciable, but are smaller than roll. This restriction allows the roll angle to represent the approximate displacement of the ship deck from a horizontal orientation.

- $O(\delta^2)$ terms can be dropped.

- The ship has a plane of approximate symmetry.

- External moments and forces are each expressible as the sum of a function of displacements and their derivatives and an explicit function of time.

- External forces and moments are differentiable functions and thus expandable in Taylor series.

- Any couplings in the equations of motion involve only the variables, not their time derivatives.

- Pitch does not occur.

- Heave is excited only by simple harmonic forcing.

- The restoring moment and damping are adequately modelled by an odd, quintic polynomial and a linear-plus-cubic polynomial, respectively.

The justification for employing these restrictions remains somewhat ad hoc. Tondl and Nabergoj [1990] make this point well, realizing that a simplified mathematical model "may produce considerably wrong predictions and lead to unreliable results for design purposes." Consequently, any results from an approximate model such as ours should be tempered with caution.

2.2 *Elementary Dynamics Techniques*

In preparation for applying invariant-manifold analysis and Melnikov's method to ship roll, we now perform an initial dynamical analysis of the model described by Equation [2.18]. Anticipating the large amount of numerical work to come, we first place the equation in state-space form. Then, to reveal some fundamental characteristics of the model, we introduce the concept of the phase plane and its features.

2.2.1 State-Space Form

If we eliminate the external-excitation term, Equation [2.18] becomes

$$\ddot{\phi} + {\omega_0}^2\phi + \alpha_3\phi^3 + \alpha_5\phi^5 + \mu_1\dot{\phi} + \mu_3\dot{\phi}^3 + h\phi\cos(\Omega t) = 0 \qquad [2.19]$$

where

ϕ = roll angle

ω_0 = linear natural frequency

α_3 = cubic restoring-moment coefficient

α_5 = quintic restoring-moment coefficient

μ_1 = linear damping coefficient

μ_3 = cubic damping coefficient

h = amplitude of parametric excitation

Ω = frequency of parametric excitation

Although this form is convenient from the standpoint that its terms have direct physical interpretations, it is customary to rewrite a second-order (or higher) differential equation as a system of first-order equations. Such a system is computationally efficient and is often termed *state-space form.* The state-space form of Equation [2.19] may be written as

$$\dot{\underline{x}} = \underline{f}(\underline{x}) + \varepsilon \underline{g}(\underline{x},t) \qquad [2.20]$$

where

$$\underline{x} \equiv \begin{bmatrix} x_1 \\ x_2 \end{bmatrix} \equiv \begin{bmatrix} \phi \\ \dot{\phi} \end{bmatrix}$$

$$\dot{\underline{x}} \equiv \begin{bmatrix} \dot{x}_1 \\ \dot{x}_2 \end{bmatrix}$$

$$\underline{f}(\underline{x}) = \begin{bmatrix} x_2 \\ -\omega_0{}^2 x_1 - \alpha_3 x_1{}^3 - \alpha_5 x_1{}^5 \end{bmatrix}$$

$$\underline{g}(\underline{x},t) = \begin{bmatrix} 0 \\ -\mu_1 x_2 - \mu_3 x_2{}^3 - h x_1 \cos(\Omega t) \end{bmatrix}$$

$$\varepsilon = 1$$

The solution of Equation [2.20] with initial conditions $\underline{x}(t_0) = \underline{x}_0$ is denoted by $\underline{x} = \underline{x}(t; \underline{x}_0, t_0)$. Although the insertion of the parameter ε in the right-hand side of the equation may seem arbitrary at this stage, it will be necessary for the application of Melnikov's method and is thus introduced here.

2.2.2 The Phase Plane

A useful byproduct of state-space form is the phase plane, a two-dimensional graph of a variable and its time derivative. For Equation [2.19], the phase plane depicts the relationship between ϕ and $\dot{\phi}$ (or equivalently, x_1 and x_2). Phase-plane plots can reveal more clearly the basic character of the system than simple time histories of the variables or their derivatives can.

To illustrate, consider a simple example: a mass attached to a spring and moving in a horizontal plane as depicted in Figure 2.3. The equation of motion is, of course, $\ddot{x} + \frac{k}{m}x = 0$. Curves in the phase plane are generated using the per unit mass potential energy function for the system: $V = \frac{k}{2m}x^2$. As shown in Figure 2.4, this function creates a *potential well*, meaning that for any given energy level $V_0 > 0$, there exist periodic oscillatory solutions. Curves in the phase plane clearly reveal the periodic nature of the solution, as they will all be closed, in this case elliptical in shape. For successively larger values of potential energy, the ellipses increase in size. Each of the curves is termed a *trajectory*, and the set of curves is collectively called a *phase portrait.*

As a first step in analyzing the ship-roll model, Equation [2.19], damping and forcing are removed to make the system conservative. The corresponding potential energy diagram and phase portrait are illustrated in Figure 2.5. When damping is added to the conservative system, the closed orbits are broken, resulting in the phase portrait in Figure 2.6. Two important features of the phase portraits are known as fixed points and separatrices.

2.2.2.1 Fixed Points

One of the most important characteristics of any dynamical system comprises the presence and location of equilibrium positions, or *fixed points.* For a rolling ship, such a point represents a fixed orientation of the ship; if the orientation is an intended one (i.e., the roll angle is not too extreme), then such a dynamic condition is desirable, as no unexpected motions (including capsize) can occur.

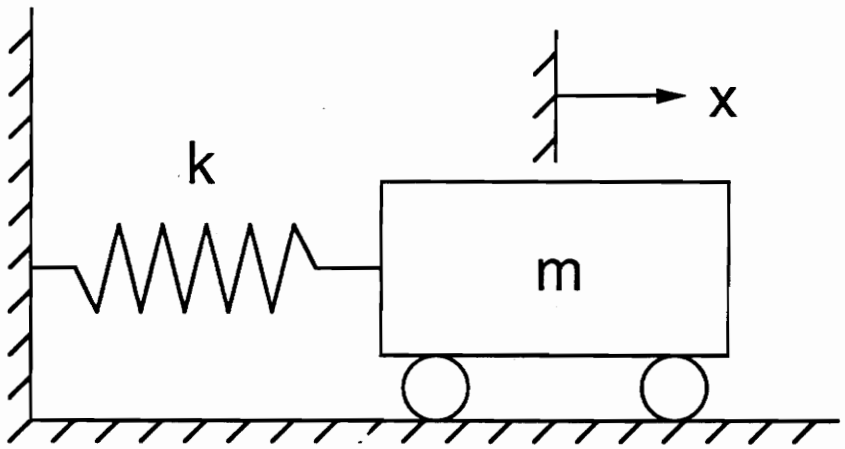

Figure 2.3. Simple Mass-Spring System: The mass is assumed to act as a rigid body, the spring is linear, and all crosshatched surfaces are frictionless and inertially fixed.

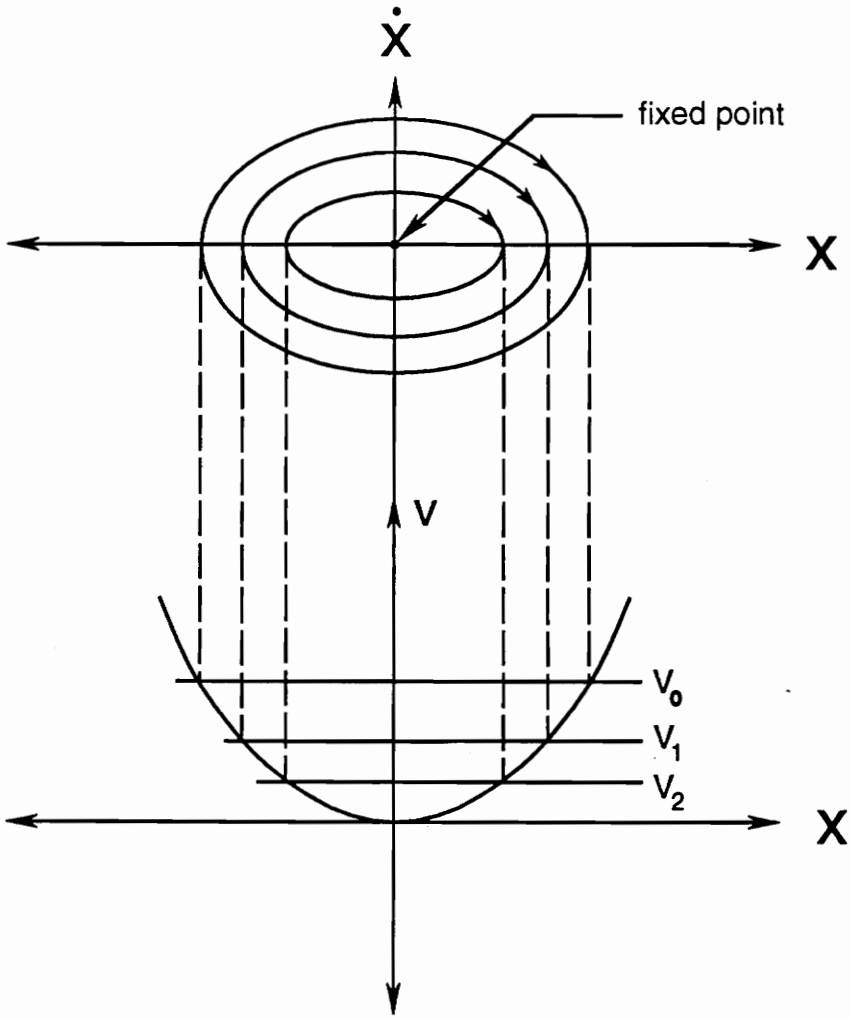

Figure 2.4. Phase Plane for Harmonic Oscillator: Pictured above is the potential energy function associated with the mass-spring system of Figure 2.3. A different phase trajectory corresponds to each distinct energy level (kinetic plus potential) possessed by the system. Note that the fixed-point or degenerate solution is indicated by a minimum-energy state.

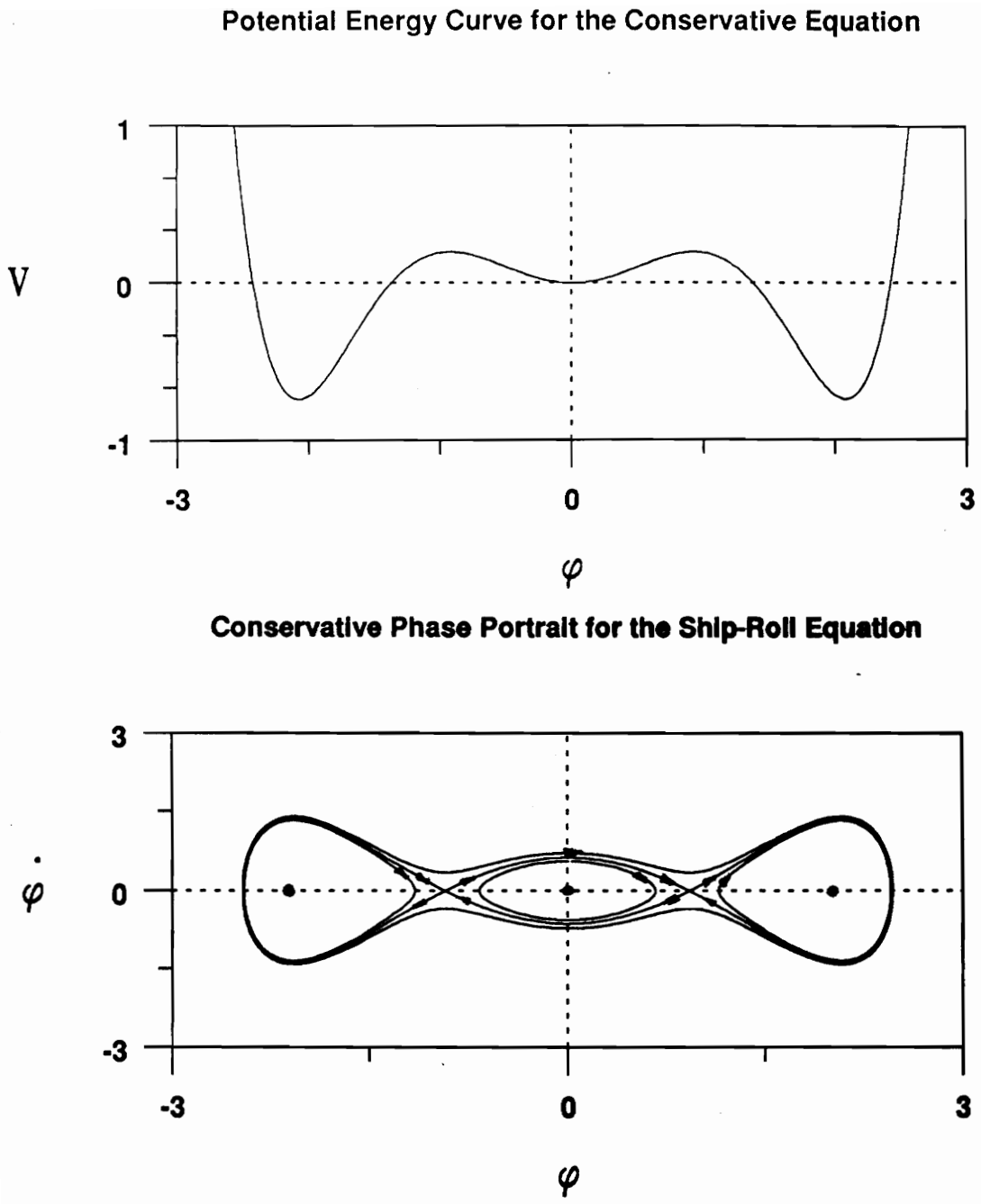

Figure 2.5. **Conservative Phase Portrait for the Ship-Roll Model:** The potential energy diagram for the conservative system appears in the top picture; the companion phase portrait is shown in the lower illustration.

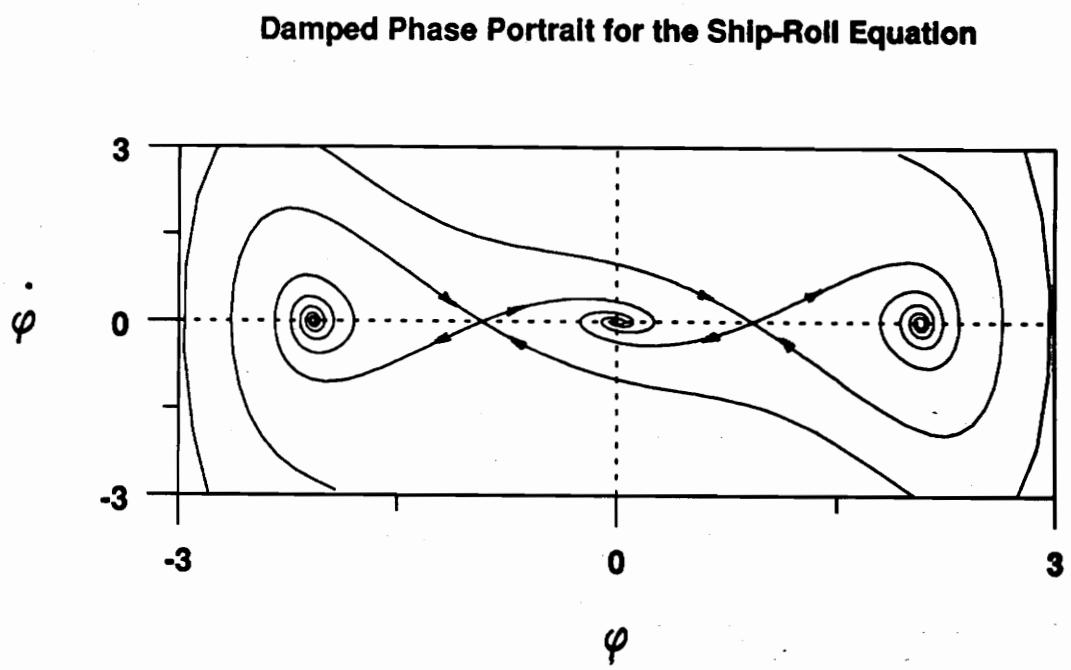

Figure 2.6. **Damped, Unforced Phase Portrait for the Ship-Roll Model:** The phase portrait for the damped, unforced form of the ship-roll model exhibits broken orbits.

The fixed points in the phase plane are degenerate trajectories and appear as single points. For illustration, again examine the phase portrait in Figure 2.5; the governing equation of this simplified system (in this case, a conservative one) is

$$\ddot{\phi} + {\omega_0}^2\phi + \alpha_3\phi^3 + \alpha_5\phi^5 = 0 \qquad [2.21]$$

The fixed points may be determined analytically by equating $\dot{\phi}$ and $\ddot{\phi}$ to zero, yielding

$$\begin{aligned} \dot{\phi} &\equiv \dot{x}_{c_1} = x_{c_2} = 0 \\ \ddot{\phi} &\equiv \dot{x}_{c_2} = -{\omega_0}^2 x_{c_1} - \alpha_3 {x_{c_1}}^3 - \alpha_5 {x_{c_1}}^5 = 0 \end{aligned} \qquad [2.22]$$

Application of the quadratic formula to the second equation results in closed-form expressions for the roots, which are

$$\begin{aligned} x_{c_1} &= 0, \pm\sqrt{\frac{-\alpha_3 \pm \sqrt{{\alpha_3}^2 - 4\alpha_5{\omega_0}^2}}{2\alpha_5}} \\ x_{c_2} &= 0 \end{aligned} \qquad [2.23]$$

For the double-subscripted quantities, the first subscript ("c") indicates the conservative equation and the second subscript denotes the vector component.

Further examination of the phase portrait in Figure 2.5 reveals the presence of two distinct types of fixed point. The origin and the extreme left and right equilibria are known as *centers* (or *foci*, in the presence of damping), while the other two are called saddle points. Centers and foci in two-dimensional phase space are identified with a linearized system (about the equilibrium position) that contains two eigenvalues having nonpositive real parts. Saddle points are associated with a linearization having one positive and one negative eigenvalue (Wiggins [1990]). As a consequence,

foci are stable equilibria that often act as attractors, centers are marginally stable equilibria, and saddles are nonstable fixed points that are intersected only by four special trajectories. When forcing is present in the model, fixed points in the phase plane in general no longer exist. However, a properly defined Poincaré map can possess fixed points, as is described in the next chapter.

2.2.2.2 Separatrices

An important feature of some conservative phase portraits comprises the special trajectories intersecting at the saddle points. These curves are known as *separatrices* because they divide the phase space into regions of qualitatively different behavior. Observe again the phase portrait in Figure 2.5. Trajectories originating inside any of the three areas enclosed by the separatrices remain inside that area. In contrast, curves beginning outside these three areas encircle all of the separatrices. (For the sake of completeness, we note here that the separatrices for a nonconservative system consist only of the trajectories that approach the saddles as time increases.)

Further inspection of Figure 2.5 reveals that conservative separatrices may be classified according to their origination and termination. If a separatrix begins and ends at the same saddle point, it is referred to as a *homoclinic orbit*. However, if a separatrix begins at one saddle point and ends at another, it is termed a *heteroclinic trajectory*. Two heteroclinic trajectories forming an enclosed area are collectively called a *heteroclinic orbit*.

Conservative separatrices not only divide the phase space of the conservative system, but can also be used to predict transverse manifold intersections and the corresponding fractal transient basins associated with a forced form of the same equation. The following two chapters include the development of the techniques necessary for making these predictions.

3. Invariant Manifolds in the Poincaré Section

3.1 Background: Poincaré Maps, Limit Sets, Manifolds

The construction of a map often requires the discretization of a continuous variable. When that variable is the time t, then the map is usually known as a *Poincaré map*. For the ship-roll model described by Equation [2.19], the discretization of time results in the conversion of the continuous-time trajectories $\underline{x}(t; \underline{x}_0, t_0)$ to the discrete points $\underline{x}_i = \underline{x}(t_0 + i\tau; \underline{x}_0, t_0)$, $i \in \mathbb{Z}$, where $\underline{x}$ is the state vector introduced in Chapter 2, $\underline{x}_0$ and t_0 are the initial state and initial time, respectively, and τ is the sampling period. Given this discretization, a Poincaré map is defined as the relationship between successive points and is expressible as $P(\underline{x}_i) = \underline{x}_{i+1}$. The specification of the initial time t_0 determines what is called the *Poincaré section*, which is a two-dimensional depiction of the iterates of a Poincaré map P. Thus, Equation [2.19] can be described with an infinite number of Poincaré maps and corresponding Poincaré sections associated with distinct values of t_0. Two iterates of a generic Poincaré map corresponding to a particular Poincaré section are shown in Figure 3.1.

A *limit set* can be defined for both continuous-time and discrete-time systems. A continuous-time limit set is the locus of state-space points which some trajectories $\underline{x}(t; \underline{x}_0, t_0)$ approach arbitrarily closely as t tends to either positive or negative infinity. A discrete-time limit

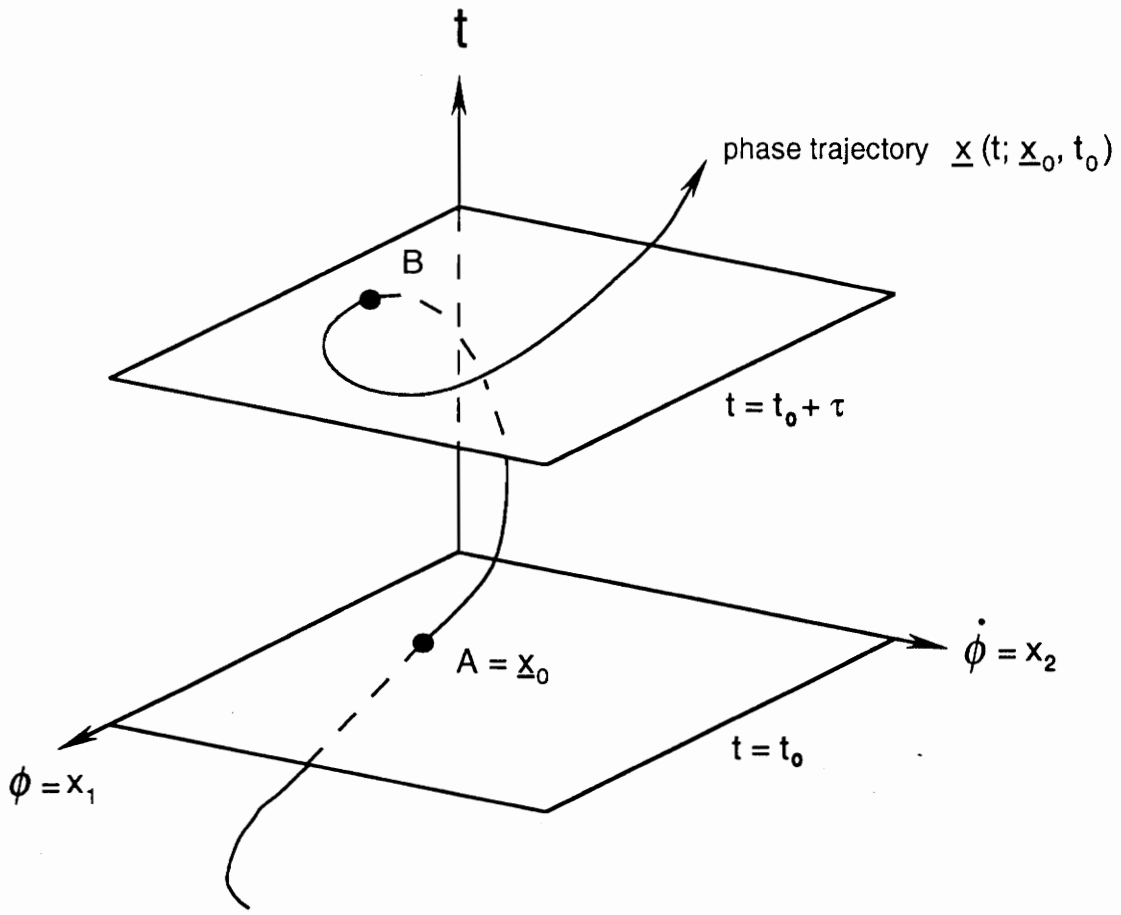

Figure 3.1. Definition of the Poincaré Section: The Poincaré section corresponding to a particular Poincaré map consists of the points A, B, etc. Conventionally, the points on the section are collapsed onto a single plane for simpler presentation.

set, on the other hand, is the locus of state-space points which some iterates $(\underline{x}(t_0 + i\tau; \underline{x}_0, t_0), i \in \mathbb{Z})$ of a map approach arbitrarily closely as i grows positively or negatively infinite. Familiar examples of limit sets include fixed points and periodic orbits. In this chapter, the limit sets of concern are the saddle points of a Poincaré map describing Equation [2.19].

Invariant manifolds can also be defined for both continuous-time and discrete-time systems. The invariant manifolds of a given limit set for a continuous-time system consist of all trajectories $\underline{x}(t; \underline{x}_0, t_0)$ that approach the limit set. Similarly, the invariant manifolds of a limit set for a discrete-time system comprise all iterates $(\underline{x}(t_0 + i\tau; \underline{x}_0, t_0), i \in \mathbb{Z})$ of a map that converge to that limit set as $i \to \pm\infty$. (In future references to invariant manifolds, the modifier *invariant* will often be omitted for brevity but is always understood.) As might be anticipated, *stable* manifolds approach limit sets when t (or i) tends to positive infinity, and *unstable* manifolds approach limit sets when t (or i) tends to negative infinity.

For the ship-roll model, Equation [2.19], we will consider the manifolds of the saddle points of a Poincaré map for a specified Poincaré section. These two-dimensional (discrete-time) manifolds are actually a subset of the three-dimensional continuous-time manifolds associated with the periodic orbits traced out by the saddle point of the Poincaré map as the section t_0 is varied. This geometry is illustrated schematically in Figure 3.2; the manifolds of the saddles of the Poincaré map for a particular Poincaré section appear as the intersection of the three-dimensional manifolds with a horizontal plane corresponding to the value of t_0. In this context, the value chosen for t_0 is unimportant because all Poincaré sections for a given type of Poincaré map are topologically conjugate (Arrowsmith and Place [1990]). Each discrete-time manifold "W" in Figure 3.2 is given a subscript ("A" or "B") to denote the associated saddle point and a superscript ("u" or "s") to indicate whether the manifold is stable or unstable. The additional superscripts divide each manifold into two parts, one of which extends to the right from the saddle point ("+") and another which extends to the left ("-"). Each of these parts is termed a *half-manifold.*

The appearance of manifolds is qualitatively identical to phase portraits. However, phase portraits represent only a single trajectory. In contrast, each discrete-time manifold is composed of a countably infinite number of iterates (under P) of an uncountable infinity of points (each of

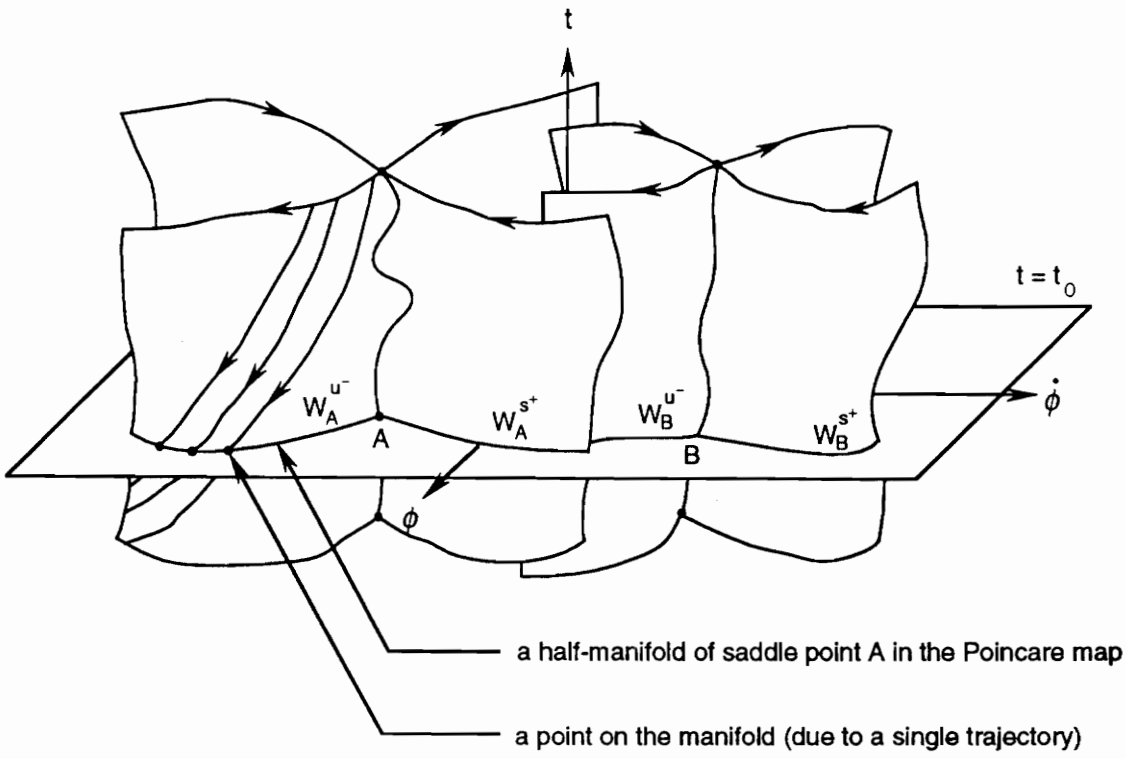

Figure 3.2. Manifolds of the Roll Equation: A schematic of the invariant manifolds of the saddle points of the Poincaré map for the roll equation, [2.18], is pictured for the section $t = t_0$.

which lies on a different trajectory). Care should be taken not to confuse phase portraits and manifolds as they have distinctly different meanings.

3.2 *Utility of Invariant Manifolds*

The study of invariant manifolds is particularly useful for those damped, forced dynamic systems that possess at least one homoclinic or heteroclinic orbit in the *conservative* phase plane. For the sake of simplicity, we describe such systems as "orbital." For orbital systems, the qualitative characteristics of the invariant manifolds associated with the saddle point(s) reveal a significant amount of information about the dynamics in the region of phase space surrounding the manifolds. Such information is crucial to avoiding undesirable dynamic behavior.

The conservative form of the single-degree-of-freedom roll model, Equation [2.21], has two homoclinic orbits and one heteroclinic orbit, meaning that the damped, forced form, Equation [2.19], represents an orbital dynamic system as we defined it. It has been shown that when the invariant manifolds of the saddle points of a Poincaré map describing an orbital system intersect transversely, sensitive dependence on initial conditions occurs in a small neighborhood near the intersections. Additionally, the respective regions of initial conditions in phase space that result in stable and unstable trajectories (collectively called a "transient basin" or a "basin-boundary diagram") become fractally divided in a neighborhood of the phase space surrounding the intersections. The mathematics involved in the proof of this fact are quite involved; the interested reader should refer to Moser [1973] and Wiggins [1990] among others, for a detailed treatment. For clarity, a qualitative illustration of a transverse intersection of the manifolds of a saddle point for a generic map is presented in Figure 3.3.

In the context of a rolling ship, the importance of intersecting manifolds is best appreciated by considering two closely spaced initial conditions near the intersections. One of these initial conditions may tend toward a stable small-amplitude periodic solution (i.e., acceptable rocking)

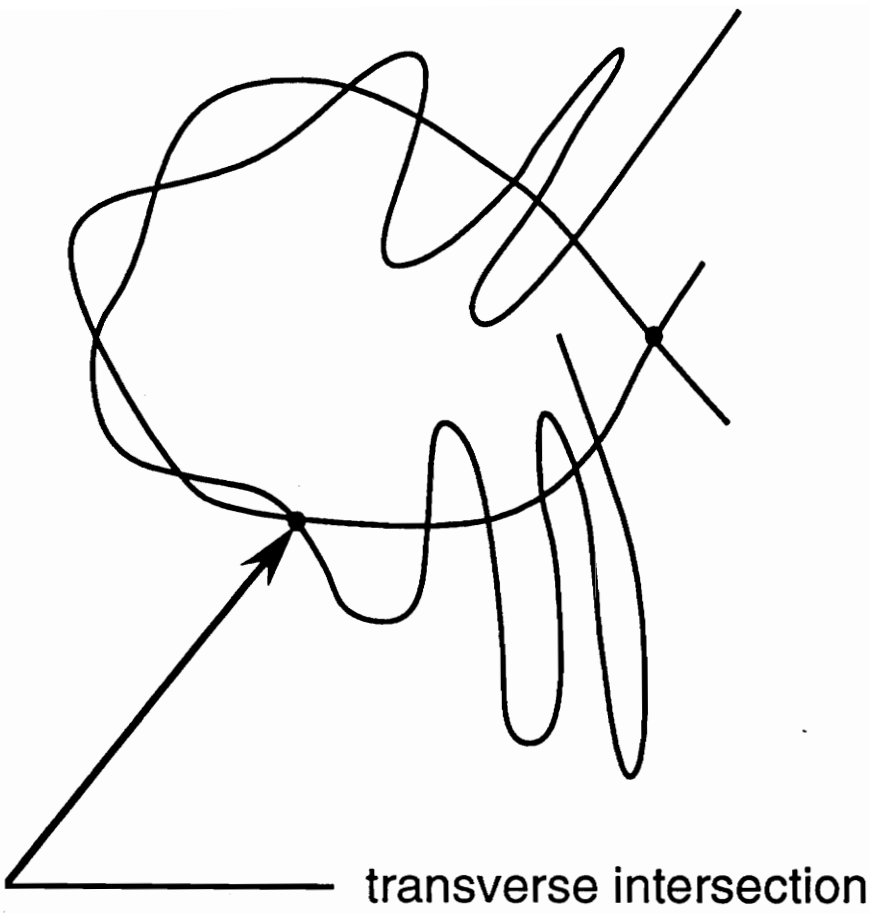

Figure 3.3. Schematic of a Transverse Manifold Intersection

while the other may result in a solution that exhibits large roll displacements (i.e., capsize). Because the phase space containing the two points is fractal, predicting which initial condition will produce what response is nearly impossible. This unpredictability makes operation of a vessel in this region of the phase space dangerous and preferably avoided.

3.3 Numerical Computation of Manifolds

The intersection of the stable and unstable manifolds of the saddle points in a Poincaré map may be directly observed by numerically computing the manifolds. In this work, the algorithm of Parker and Chua [1989] is applied to Equation [2.19] to generate the manifolds of interest. The entire procedure is detailed in the following sections, including the unexpected problem of accurately approximating the saddle points.

Although the exact location of the perturbed saddles is not in itself exceedingly important, the viability of the manifold-generating algorithm depends on the precise specification of these points. We first attempt to approximate the saddle points using a standard linearization technique. This approach proved inadequate. Consequently, we introduce a rather sophisticated search algorithm based on a method developed by Hooke and Jeeves to approximate the saddles with sufficient accuracy.

3.3.1 Linearized Approximations to the Saddle Points

Before using the aforementioned algorithm to compute the manifolds, we must find approximations to the saddle points of the Poincaré map describing Equation [2.19]. For future reference, the exact locations of the saddles are denoted by $\underline{x}^*$. As a first step, we characterize the local behavior of the Poincaré map in the neighborhood of the saddle point of the conservative

system, $\underline{x}_c^*$, by expanding about that point. We recall that the conservative system may be expressed as

$$\dot{\underline{x}} = \underline{f}(\underline{x}) + \varepsilon \underline{g}(\underline{x},t) \qquad [3.1]$$

where

$$\underline{f}(\underline{x}) = \begin{bmatrix} x_2 \\ -x_1 - \alpha_3 x_1^{\,3} - \alpha_5 x_1^{\,5} \end{bmatrix}$$

$$\underline{g}(\underline{x},t) = \begin{bmatrix} 0 \\ -\mu_1 x_2 - \mu_3 x_2^{\,3} - h_1 x_1 \cos(\Omega t) \end{bmatrix}$$

$$\underline{x} \equiv \begin{bmatrix} x_1 \\ x_2 \end{bmatrix} \equiv \begin{bmatrix} \phi \\ \dot{\phi} \end{bmatrix}$$

$$\varepsilon = 1$$

If we expand about the unperturbed saddle point $\underline{x}_c^*$, use the notation $\underline{x}_t(t) = \underline{x}_c^* + \underline{u}(t)$, and substitute into Equation [3.1], we obtain

$$\dot{\underline{u}} = \nabla \underline{f}(\underline{x}_c^*)\underline{u} + \underline{g}(\underline{x}_c^*,t) + \ldots \qquad [3.2]$$

If we neglect higher-order terms, the result is a linear, first-order, nonhomogeneous differential equation with constant coefficients that may be solved analytically using an integrating factor. If we subsequently realize that a fixed point of the Poincaré map requires that $\underline{u}(t_0) = \underline{u}(t_0 + T)$, then the perturbed saddle can be approximated according to (Li and Moon [1990])

$$\underline{x}_\varepsilon - \underline{x}_c^* = \varepsilon \left[I - e^{\nabla \underline{f}(\underline{x}_c^*)T} \right]^{-1} \int_{t_0}^{t_0+T} e^{\nabla \underline{f}(\underline{x}_c^*)(t_0+T-\tau)} \underline{g}(\underline{x}_c^*, \tau)\, d\tau + \ldots \qquad [3.3]$$

where t_0 specifies the Poincaré section and T is the period of the excitation. The above expression may be computed numerically for the ship-roll equation. Unfortunately, the use of this approximation in the algorithm to be described in Section 3.3.3 is inadequate, indicating that an even more accurate estimate of $\underline{x}^*$ is required.

3.3.2 Refined Saddle-Point Approximation: Hooke-Jeeves Algorithm

The failure of the linearized approximation to generate an acceptable estimate of the saddle points reflects the extreme sensitivity of this Poincaré map near the saddle points. In other words, points in close proximity to the saddles move quickly away as time passes. For example, a point only hundredths or even thousandths of a unit distant from the true saddle point might move a full unit away from the saddle point under one iteration of the map. This behavior causes Newton-Raphson iteration, a standard fixed-point technique, to converge not to the saddles, but to the stable fixed points of the system.

3.3.2.1 Standard Algorithm

As a result, a more effective scheme must be chosen. Because of its simplicity and general applicability to nonlinear systems, we implement the search algorithm credited to Hooke and Jeeves (Avriel [1976]). The necessary numerical integration is carried out using the variable-step fifth- and sixth-order double precision IMSL routine DIVPRK (IMSL [1989]). This search technique may be used to locate the minimum or maximum of an arbitrary function; in this case, the function of interest is the distance (in the phase space) between successive iterates of the Poincaré map. We proceed with a brief outline of the technique. (The interested reader will note that Appendix A contains pseudo-code for the standard algorithm described in this section as well as for the modifications presented in the next two sections.)

First, we define a function $F(\underline{x}) = \|P(\underline{x}) - \underline{x}\| \geq 0$, which is the distance between a point in the Poincaré section and its iterate under the Poincaré map P. This function has a global minimum (equal to zero) only at the fixed points of P (i.e., $F(\underline{x}^*) = 0 \Leftrightarrow P(\underline{x}^*) = \underline{x}^*$). Because F has a value of zero for the saddle points, and because the trajectories that terminate at the saddles approach them asymptotically, a good approximation to the saddles will have a small value of F. Thus, if F is sufficiently small, then a satisfactory approximation has been found.

The algorithm starts with a rough estimate for $\underline{x}^*$; we select the linearized estimate $\underline{x}_L$ as computed in Section 3.3.1. This starting point is also called the first *base point*. The first step consists of moving a prescribed distance Δ along the $+x_1$-axis and comparing the value of F at this new point with the value of F at the base point. If the move *increases* F (a bad move), then a move Δ along the $-x_1$-axis is taken from the base point, where F is also calculated. If the value of F at this point is smaller than at the base point, it is accepted as the *horizontal temporary point* corresponding to the first base point. On the other hand, if the first move decreases F (a good move), then that point is immediately accepted as the horizontal temporary point for the first base point, meaning that the check to the left of the base point is unnecessary. A final possibility is that the value of F is smaller at the base point than at either of the two other points. In that case, the horizontal temporary point is defined as the base point itself. This procedure is known as a series of exploratory moves; it is repeated for the x_2-direction, beginning at the horizontal temporary point and culminating in the second base point. To summarize, we note that any exploratory move is successful if it decreases the value of F and unsuccessful if it increases F.

If the second base point coincides with the first, then all of the exploratory moves were unsuccessful, indicating that the step size Δ should be reduced and the exploratory-move sequence repeated. However, if the second base point is distinct from the first, then a *pattern move*, which consists of adding the vector difference between the two base points to the *second* base point, is executed.

The algorithm continues with the exploratory-move sequence, resulting in another base point. If the new base point has a smaller value of F than the old one, the previous pattern move is deemed successful, warranting another a pattern move. This procedure continues until one of two

situations arises. The first possibility is that a base point is reached for which the value of F is greater than that for the previous base point. In other words, the most recent pattern move is judged to be unsuccessful. In this case, the exploratory-move sequence starts again from the prior base point. The second condition that might occur is the satisfaction of the criterion for success (i.e., F is sufficiently close to zero), meaning that the search terminates.

Consider the example in Figure 3.4. The illustration contains two iterations of the exploratory-move pattern-move sequence. The base points are labelled with b_i, the horizontal temporary points with t_i^h, and the results of pattern moves with PM_i. Note that although the initial step size (Δ) might not change, pattern moves can grow in size if a particular direction is preferred; for example, the second pattern move in the figure is larger than the first one.

Two problems may cause the algorithm to fail. In one case, the step size Δ might become excessively small as a result of successive reductions, making exploratory and pattern moves essentially meaningless and causing the search to stall far from the desired approximation. In another instance, the search might seek out one of the stable fixed points rather than the saddle point. These shortcomings are now addressed.

3.3.2.2 Additions to the Standard Algorithm

Both of the aforementioned problems prompt the same question: how can the search continue now that the algorithm has failed? One possible answer is application of the algorithm with a different initial guess. Yet how can a new guess be intelligently formulated? Because the linearized estimate $\underline{x}_i$ is the only approximation available, we randomly select a point inside a square box centered at $\underline{x}_i$ as the new starting point for the Hooke-Jeeves search. If the search fails again, we choose a new point inside the box. To refine this procedure, we move the center of the box to a new location whenever the search algorithm finds a nearby point with a smaller value of F than for $\underline{x}_i$.

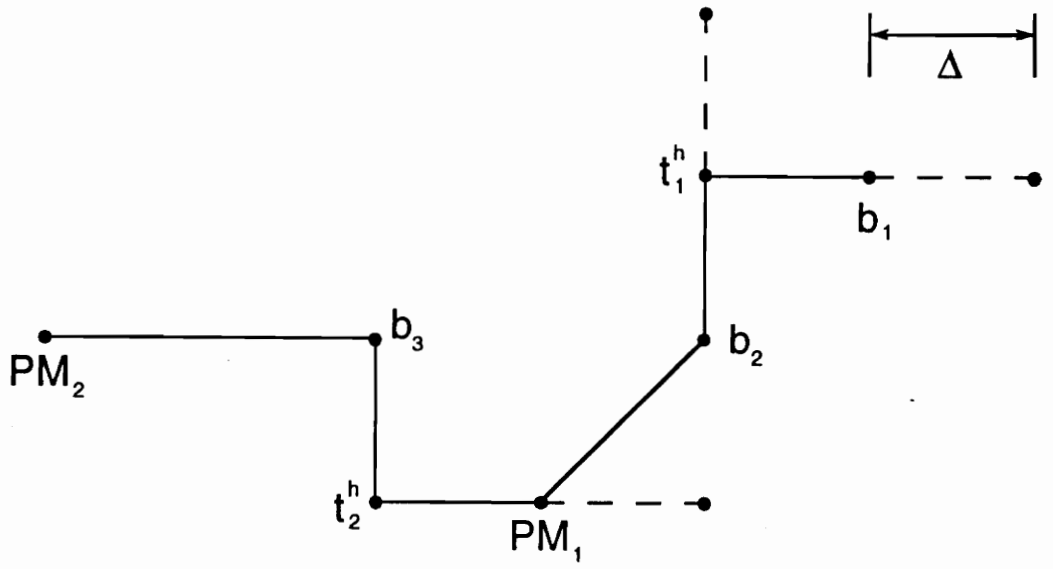

Figure 3.4. The Hooke-Jeeves Algorithm: Alternating sets of exploratory and pattern moves are executed in the process of finding the minimum of a function. The step size is labelled Δ. The base points are labelled with b_i, the horizontal temporary points with t_i^h, and the results of pattern moves with PM_i. The dashed lines indicate failed exploratory moves.

Another refinement concerns the parameter ε, which was introduced in Chapter 2. Although we initially set the value to one, it proves useful in searching for the saddles to start with a small value of ε. In the application of the Hooke-Jeeves algorithm, ε is gradually increased from zero to one, with the saddles determined for one value of ε used as initial guesses for the next larger value of ε. This "softening" technique seems to improve the effectivess of the search. Generally, a greater number of intermediate ε-values results in more reliability but less efficiency.

The success of the modified algorithm is strongly dependent on two parameters: the size of the box (inside which the guesses were selected) and the initial step size Δ. Large boxes tend to cause the search to converge on the stable fixed points rather than on the saddle. With small boxes, the search occasionally seeks out what would appear to be a local minimum for F; successive values for F become closer together, eventually converging to a nonzero value. Then, because the box is too small, all of the random guesses tend to converge to this unsatisfactory local minimum. The choice of an initial value for Δ creates much the same pattern: large values induce the search to jump to another fixed point and small values make the search proceed too slowly or ineffectively to be efficient. These qualitative observations are made using trial and error; no *a priori* knowledge indicates what effects the two parameters might have.

An attempt was made to automate the search process for many values of the different system parameters (i.e., the cubic and quintic restoring-moment coefficients, the damping coefficients, and the excitation). Through variation of the box size and the initial step size, it was anticipated that acceptable saddle-point approximations could be generated without any user interaction. However, the changing sensitivity of the Poincaré map frequently causes the automation either to fail entirely or to take an impractically long time to run. Consequently, separate cases must be run interactively with trial-and-error combinations of box size and step size until success is achieved.

3.3.2.3 *Multiple Approximations*

Another difficult issue involves the location of an approximate saddle with respect to the true saddle. Observe the qualitative structure of the manifolds near a saddle point as shown in Figure 3.5. The phase space is divided into four distinct regions, labelled arbitrarily with I through IV. Any approximation to the saddle will necessarily lie in one of those four regions, although which region is unknown without additional information. Figure 3.5 indicates that application of the Poincaré map P (forward integration) to points in regions I and II yields iterates lying near the manifold segment W^{u^+} and application of P to points in regions III and IV produces points close the segment W^{u^-}. On the other hand, application of the inverse Poincaré map P^{-1} (backward integration) to points in region II or III generates iterates near the manifold segment W^{s^+}; application of P^{-1} to points in region I or IV similarly yields iterates close to W^{s^-}. Given these characteristics, we note that four different saddle approximations are necessary to generate all of the manifolds associated with a particular saddle point. In addition, these approximations cannot be determined independently; the manifold segment produced by one saddle approximation must be identified before the other saddle approximations corresponding to the other three manifold segments can be identified. (In other words, the Hooke-Jeeves algorithm provides no information regarding the regional location of the approximations it produces.) Complicating the situation even further is the requirement that this identification be performed quickly by a computer code; manual identification would be extremely inefficient.

One solution to this difficulty involves careful inspection of the phase space near the true saddle. First, we note that the manifolds will always form an "X" as in Figure 3.5. As a result, the angles formed by the manifolds can always be bisected, yielding two perpendicular lines as shown in Figure 3.6. (Although the lines in the picture are horizontal and vertical, in general they need not be.) For convenience, we define the two lines to be the η_1-axis and η_2-axis of a Cartesian coordinate system. The directions of these axes may be determined approximately by numerically computing the eigenvectors associated with the Jacobian matrix of the Poincaré map evaluated at

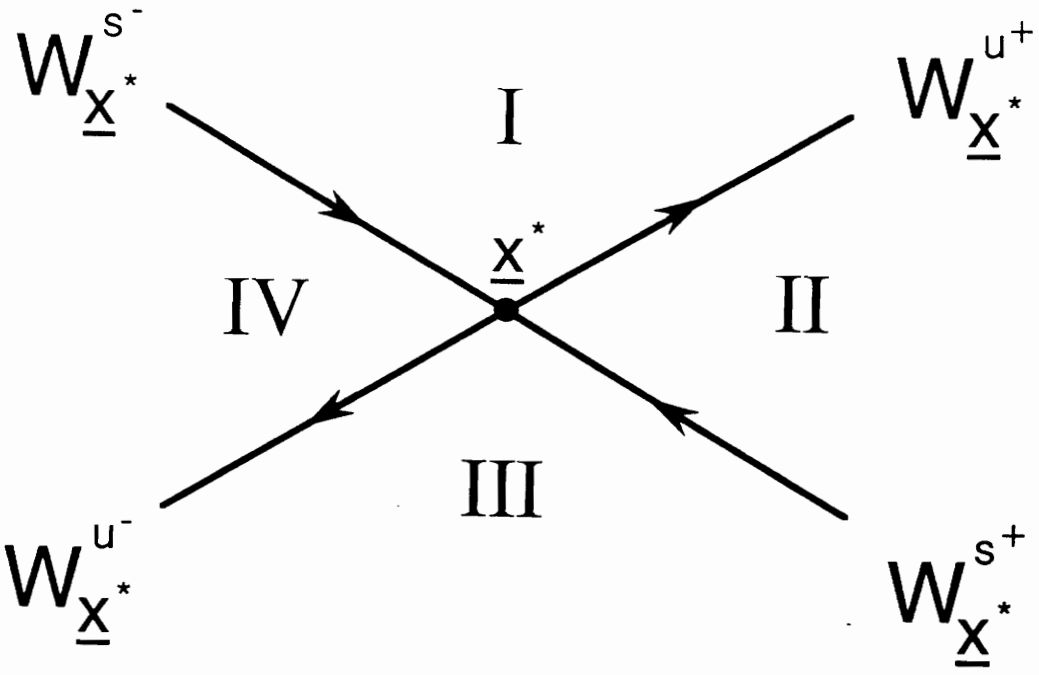

Figure 3.5. Phase Space Near a Saddle Point

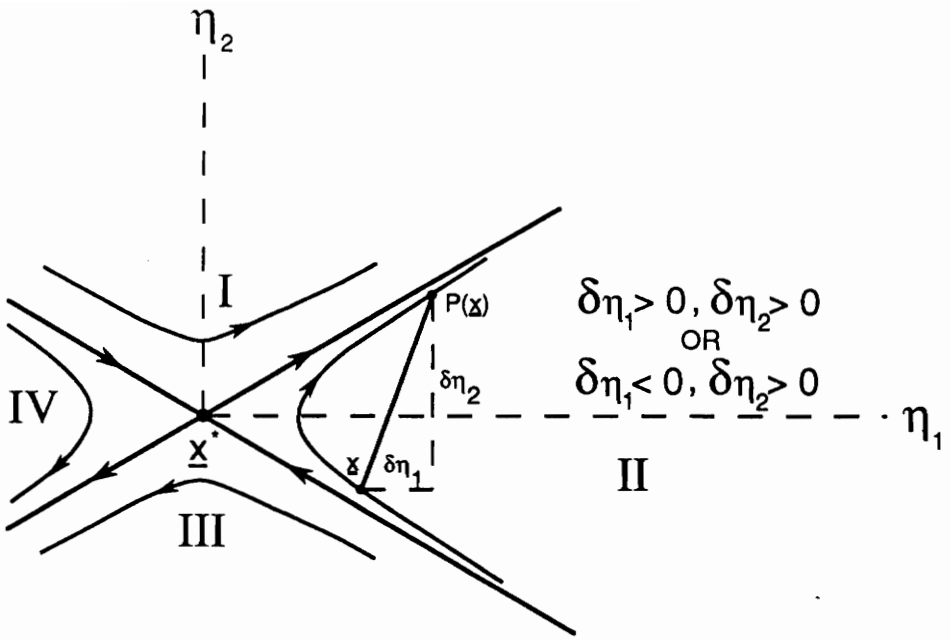

Figure 3.6. **Possible Displacements for an Iterate of the Poincaré Map:** For one region of the phase space near a saddle point, the displacement components of $P(\underline{x}) - \underline{x}$ in the η_1-η_2 coordinate system are shown. Note that $\delta\eta_2$ is always positive.

the saddle-point approximation returned by the search algorithm. Bisection of the resulting "X" (a matter of elementary geometry) produces the desired η_1- and η_2-directions.

Now consider the η_1- and η_2-components of an arbitrary displacement vector $P(\underline{x}_0) - \underline{x}_0$. If we make the assumption that the manifold has a hyperbolic appearance in the neighborhood of the saddle, then the following four consequences seem likely, if not guaranteed. First, if $\underline{x}_0$ is in region I, then the change in x-coordinate ($\delta\eta_1$) must be positive while the change in y-coordinate ($\delta\eta_2$) could be positive or negative. Second, if $\underline{x}_0$ is in region II, then $\delta\eta_2$ must be positive and $\delta\eta_1$ could be either sign. Third, an initial condition in region III will have $\delta\eta_1 < 0$ with $\delta\eta_2$ of indeterminate sign. Fourth and last, region IV produces $\delta\eta_2 < 0$ with $\delta\eta_1$ either positive or negative. The conditions for region II are illustrated in Figure 3.6 as an example. With the aid of these observations, we draw two conclusions. If $\delta\eta_1$ and $\delta\eta_2$ are both positive, then the manifold segment W^{u+} will be approximated regardless of whether the saddle-point approximation lies in region I or in region II. Likewise, if $\delta\eta_1$ and $\delta\eta_2$ are both negative, then W^{u-} will result from that saddle approximation.

We have thus achieved a simple criterion for determining what manifold segment will be produced by an arbitrary saddle approximation under the influence of the Poincaré map P. For every candidate returned by the search algorithm, the eigenvectors of the Jacobian for the Poincaré map are calculated and used to compute the corresponding η_1- and η_2-directions. Then the map P is applied to the saddle approximation, and the consequent displacement components are calculated. Candidates are generated and tested until one with $\delta\eta_1 > 0$ and $\delta\eta_2 > 0$ and another with $\delta\eta_1 < 0$ and $\delta\eta_2 < 0$ are found. At this point, we have two saddle approximations capable of producing the entire unstable manifold.

The procedure for finding the two saddle approximations necessary for generating the stable manifold is analogous. However, instead of the Poincaré map P, the inverse map P^{-1} must be used. Further, the displacement components must satisfy different criteria: $\delta\eta_1 > 0$ and $\delta\eta_2 < 0$ indicate that W^{s+} will be generated, and $\delta\eta_1 < 0$ and $\delta\eta_2 > 0$ indicate that W^{s-} will be produced. Other than these differences, the steps for finding the stable-manifold saddle approximations are identical to those outlined above.

3.3.3 Manifold Generation

To compute the manifolds, given the four saddle-point approximations, we apply an algorithm presented by Parker and Chua [1989]. The backbone of the algorithm is quite simple. First, the map $P(\underline{x})$ is applied to one of the saddle-point approximations, which is denoted with $\underline{x}_s$. The resulting point marks the start of one of the half-manifolds. Second, the map is applied to a succession of points ($\underline{x}_i$, $i = 1,2,3,...$) starting near $\underline{x}_s$ to create the half-manifold. (To avoid possible confusion, note that in this context $\underline{x}_{i+1} \neq P(\underline{x}_i)$ as was the case in Section 3.1.) This procedure is repeated to create all the half-manifolds of interest. All numerical integration is carried out using the IMSL routine DIVPRK mentioned earlier.

A major flaw makes this simple technique ineffective without some revision. For an arbitrary $P(\underline{x}_i)$, $P(\underline{x}_{i+1})$ might not be "close enough" to $P(\underline{x}_i)$, meaning the approximation of the manifold will be crude. To overcome this problem, Parker and Chua suggest that the distance between $P(\underline{x}_i)$ and $P(\underline{x}_{i+1})$ be computed. If the distance is greater than some tolerance, then the corresponding points $\underline{x}_i$ and $\underline{x}_{i+1}$ are interpolated to obtain a new value $\underline{x}_j$, to which P is applied and the resulting point tested for proximity to $P(\underline{x}_i)$. If this distance is again too large, further interpolations are executed as necessary to satisfy the tolerance. A noteworthy feature of this algorithm is that an arbitrary iterate $P(\underline{x}_i)$ is only accepted as part of the manifold when a $P(\underline{x}_j)$ close enough to $P(\underline{x}_i)$ is determined. The iteration procedure and the refinement just described are illustrated in Figure 3.7, using the notation developed.

At this point, consider again the need to approximate the saddle point accurately. Earlier, it was noted that the linearized approximation was inadequate. To appreciate why, recall that $P(\underline{x}_s)$, not $\underline{x}_s$, is the first point of the manifold generated. As a result, both the approximation *and* its first iterate must be "close to" the actual saddle point $\underline{x}^*$. Otherwise, a substantial portion of the manifold is omitted, possibly including the segment containing the transverse intersections sought. Yet due to the sensitive nature of this Poincaré map, noted in Section 3.3.2, the first iterate of points

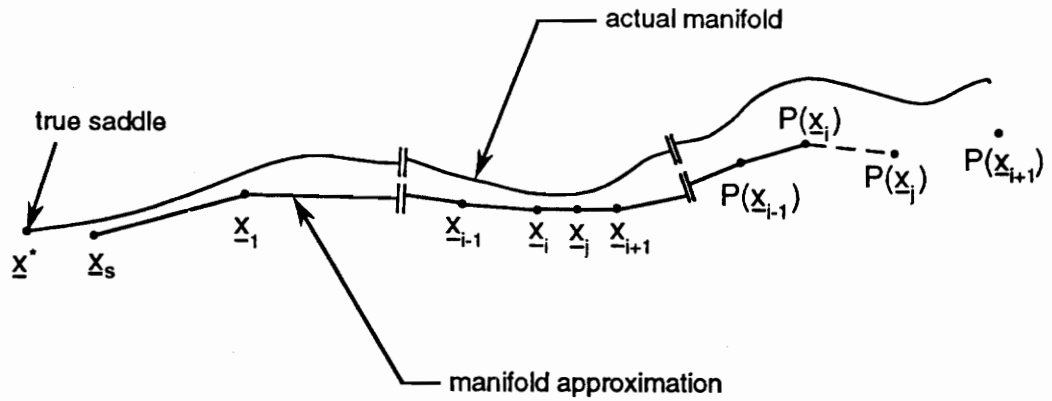

Figure 3.7. Parker and Chua's Algorithm: A manifold is computed by applying the Poincaré map P to successive points on the manifold, beginning with the saddle-point estimate $\underline{x}_s$. If two computed points are too far apart, an intermediate is calculated by interpolating the two points whose iterates were those computed points, and then applying P. In the above picture, for example, $P(\underline{x}_{i+1})$ is too far from $P(\underline{x}_i)$, so $\underline{x}_i$ and $\underline{x}_{i+1}$ are interpolated to obtain $\underline{x}_j$ and thus $P(\underline{x}_j)$. Since $P(\underline{x}_j)$ is close enough to $P(\underline{x}_i)$, $P(\underline{x}_i)$ is accepted as part of the manifold approximation. The dashed line indicates that acceptance of $P(\underline{x}_j)$ hinges on the proximity of $P(\underline{x}_{i+1})$.

reasonably close to $\underline{x}^*$, such as $\underline{x}_t$, tend to be quite distant from either point. Hence, the refined Hooke-Jeeves technique of Section 3.3.2 is necessary.

3.3.4 Computed Manifolds: Examples

The numerical techniques described in the last several sections were implemented through the use of a number of FORTRAN routines. To verify the computer codes, we apply them to a well-known system, the forced Duffing equation. Following Arrowsmith and Place [1990], we look at the equation in the form

$$\ddot{x} + \mu\dot{x} + x - x^3 = F\cos(\Omega t) \qquad [3.4]$$

Two different cases are examined: for each the damping coefficient is set equal to 0.125, while the forcing amplitude takes on the values 0.11 and 0.19. The resulting manifolds compare well with those computed independently and published by Arrowsmith and Place [1990] (Figures 3.8 and 3.9). The qualitative nature of these curves are of no particular significance; only the validity of the manifold-generating software is of concern.

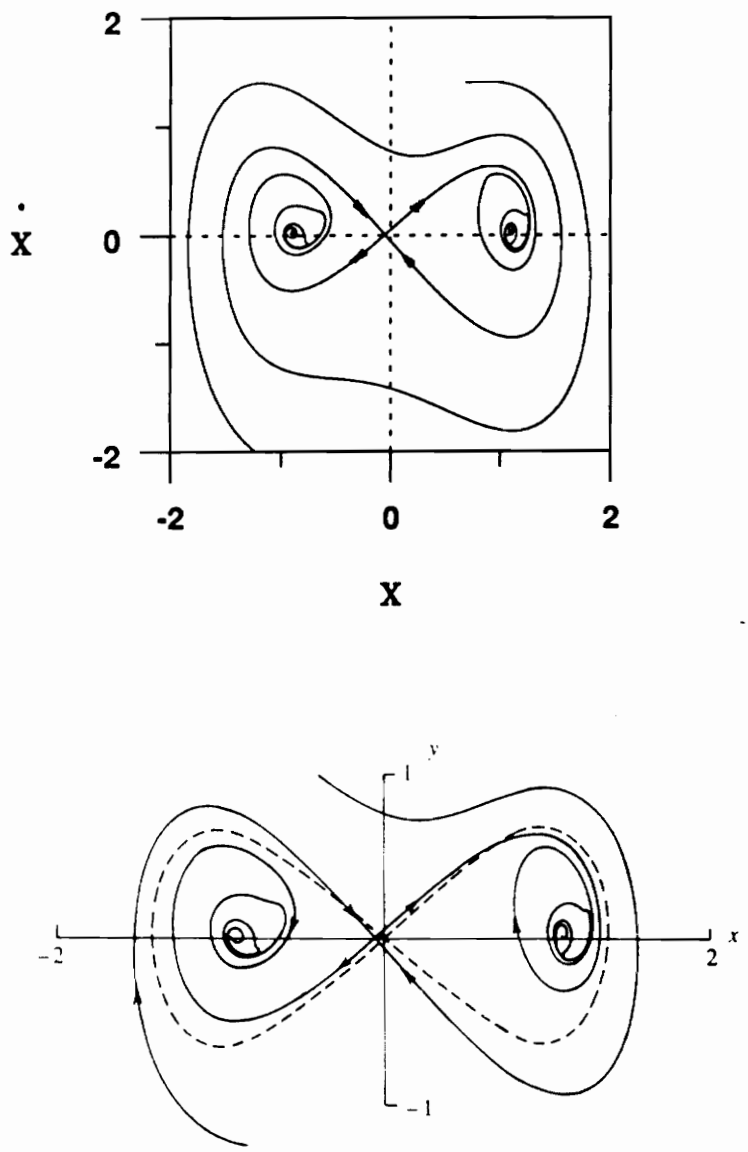

Figure 3.8. **Invariant Manifolds: Test Case (F = 0.11):** Illustrated is a graphical comparison of one set of invariant manifolds of the saddle point of a Poincaré map describing the forced Duffing equation. The top picture was generated using Parker and Chua's algorithm; the lower one is a copy of that produced by Arrowsmith and Place [1990]. Note that the two pictures are practically indistinguishable.

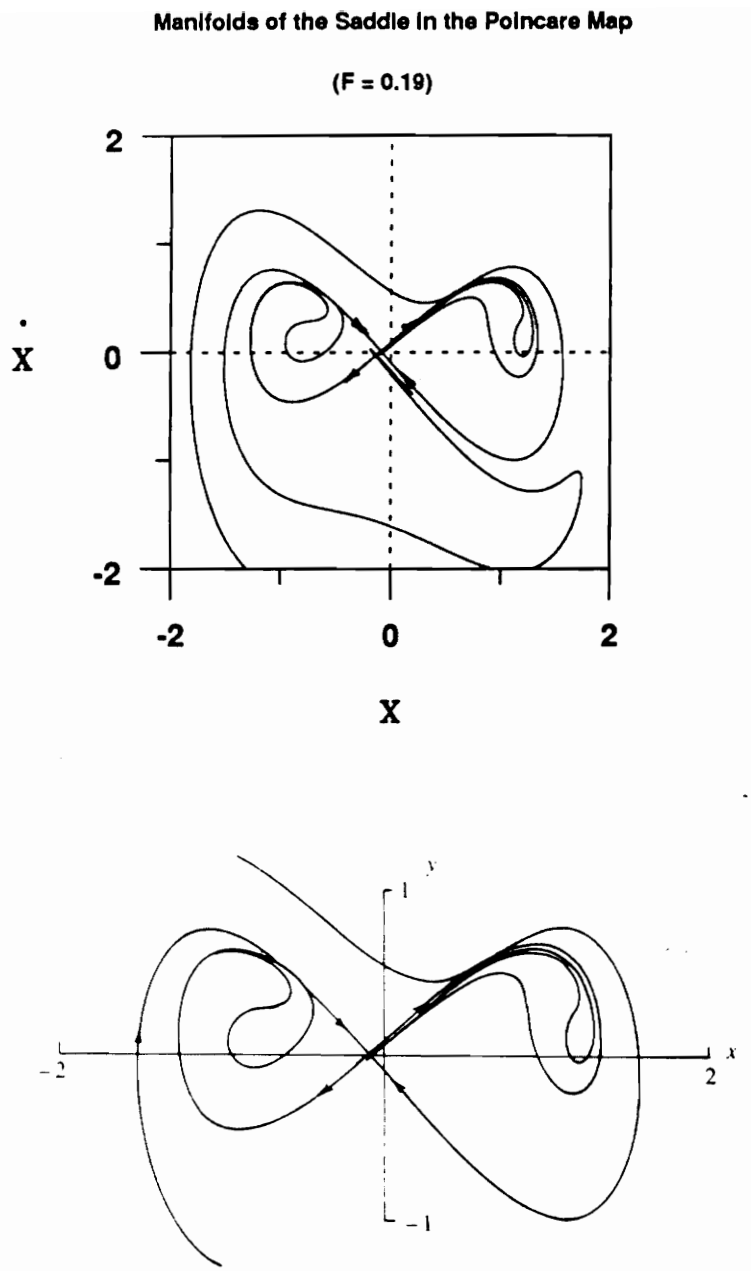

Figure 3.9. Invariant Manifolds: Test Case (F = 0.19): A second comparison of invariant manifolds for the Duffing equation includes a higher excitation level. Again, the agreement is excellent.

4. Application of Melnikov's Method

In Chapter 3, a sophisticated procedure for generating the manifolds of the saddles of a Poincaré map was developed, allowing detection of their transverse intersections, or "tangles." A great deal of analysis and particularly computational effort is necessary to compute the manifolds, however. As a result, a less time-consuming approximate method containing similar information is of substantial practical interest.

Developed in the 1960's by the researcher for whom the technique is known, Melnikov's method is such a timesaving procedure. Applicable for any system having unperturbed homoclinic or heteroclinic orbits, the method requires that the system equations be written as a perturbation of a Hamiltonian system. Afterwards, the minimum distance between the stable and unstable manifolds of a saddle point of the map (in our case a Poincaré map) describing the perturbed system is approximated. Should this distance vanish for any point in the phase space, then the onset of transverse manifold intersections is predicted to occur. In the next section, the example of a homoclinic orbit is used to derive the Melnikov function. Subsequent sections describe the application of the method to the ship-roll model for predicting both homoclinic and heteroclinic tangles. Finally, the phenomenon of mixed intersections (tangles between one homoclinic manifold and one heteroclinic manifold) is analyzed using Melnikov's technique.

4.1 *Derivation of the Melnikov Function*

A number of dynamicists have investigated the use of Melnikov's method to predict transverse homoclinic intersections, including Wiggins [1990] and Falzarano [1990]. Consequently, homoclinic geometry is used to develop a distance function and eventually a form of the Melnikov function. Due to the difficult nature of the mathematics underlying this method, many of the details of the derivation are presented to provide some intuition. Readers already familiar with Melnikov's method will not lose continuity by skimming the following development for notation and then skipping to Section 4.2.

Although various authors treat this topic in different ways, an especially clear explanation, found in the work of Arrowsmith and Place [1990], is examined here. Consider a dynamic system that may be modelled with equations of the form

$$\dot{\underline{x}} = \underline{f}(\underline{x}) + \varepsilon \underline{g}(\underline{x},t) \qquad [4.1]$$

where

$\underline{f}(\underline{x})$ = Hamiltonian part of $\dot{\underline{x}}$

$\underline{g}(\underline{x},t)$ = periodic perturbation of the Hamiltonian system

Recall that this form is identical to Equation [2.20], in which the quantities $\underline{f}$ and $\underline{g}$ were defined in terms of the parameters of the ship-roll model. The parameter ε is an explicit measure of the smallness of the perturbation $\underline{g}$ and may be equated to unity if $\underline{g}$ is sufficiently small. For the purposes of this derivation, the only restriction placed on $\underline{f}$ and $\underline{g}$, other than the characteristics described in Equation [4.1], is that the unperturbed system $\dot{\underline{x}} = \underline{f}(\underline{x})$ produces at least one homoclinic orbit in two-dimensional phase space.

At this point, two additional parameters are defined in order to fully describe the three-dimensional manifold structures associated with both the unperturbed and perturbed

continuous-time systems. First, the symbol θ denotes the particular Poincaré section chosen; it replaces the symbol t_0 used in Chapter 3 and may vary in the interval spanning the period of $\underline{g}$, namely $(0, 2\pi/\Omega]$. Second, $t \in (-\infty, +\infty)$ is defined as the time required for a chosen point on the discrete-time manifold in section θ to be reached by the trajectory beginning at a given initial condition. Although θ and t are both values of time, θ refers only to the Poincaré section chosen while t is the elapsed time describing a particular trajectory. As an example, consider the unperturbed continuous-time manifolds illustrated in Figure 4.1; any point on the surface can be located by specifying θ and t.

Unlike the unperturbed system, for which all Poincaré sections are identical, the perturbed system is described by Poincaré sections that are distinct for each value of θ in the interval spanning the period of the forcing function $\underline{g}$. Any value of θ outside this interval may be identified with a θ value which is inside the interval and which is also an integral multiple of $2\pi/\Omega$ distant from the original value. This identification is possible because any point located on one of the two sections will eventually appear on the other. Thus, for any perturbed system, only the Poincaré sections defined for an interval of the forcing period are unique.

In Chapter 5, the focus will be not on the three-dimensional continuous-time manifolds, however, but instead on the discrete-time manifolds found in particular two-dimensional Poincaré sections. Such a section is illustrated in Figure 4.2, which contains schematics of both the homoclinic orbit of the unperturbed system and the broken manifolds that result when damping or forcing is added.

A distance function that characterizes the proximity of the perturbed manifolds is now constructed. During the upcoming development, it may be helpful to refer to the illustration in Figure 4.3. First, consider the unperturbed homoclinic orbit in the Poincaré section defined by an arbitrary value $\theta = \theta_0$. Then draw a perpendicular ("L") to the orbit at an arbitrary but fixed location $\underline{x}_c$, defined to be the value of the time-varying function $\underline{x}_c(t - \theta_0)$ when $t = \theta_0$. The quantity $\underline{x}_c(t - \theta_0)$ is a vector that traces out the unperturbed homoclinic orbit as t varies. Next, the curves $\underline{x}^s(t; \theta_0)$ and $\underline{x}^u(t; \theta_0)$ are defined as the perturbed stable and unstable manifolds in the section $\theta = \theta_0$ that correspond to the homoclinic orbit. These manifolds intersect the line L at the

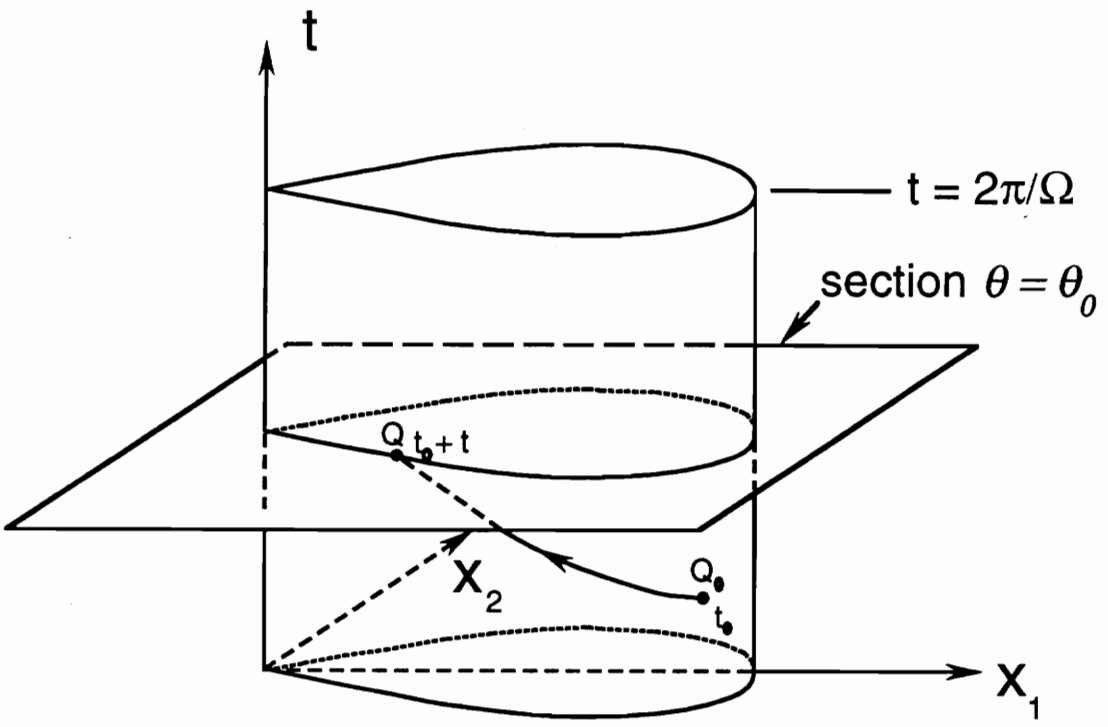

Figure 4.1. Unperturbed Invariant Manifold: A generic homoclinic invariant-manifold structure in three-dimensional phase space is illustrated. The arbitrary point Q on the surface is specified by selecting a particular Poincaré section ($\theta = \theta_0$) and the time (t) required to travel from the reference point Q_0 to the point Q.

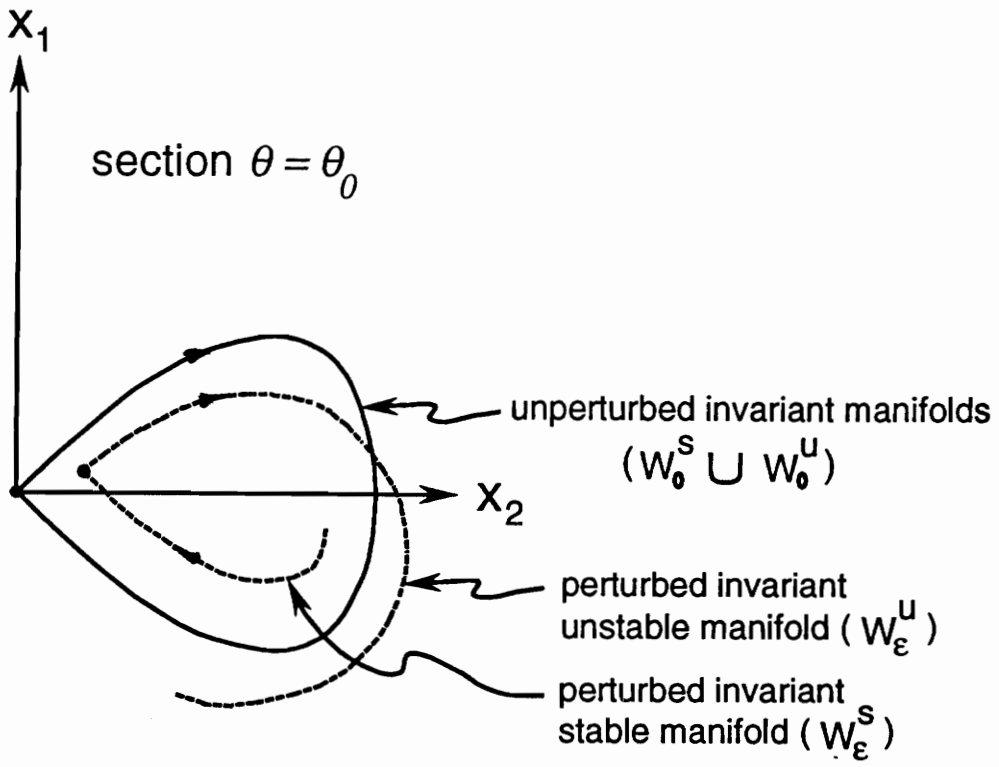

Figure 4.2. Manifolds in the Poincaré Section: The invariant manifolds for both the unperturbed system (solid curve) and the damped, forced system (broken curves) are pictured. Note that the stable and unstable manifolds coincide for the unperturbed case, creating a homoclinic orbit.

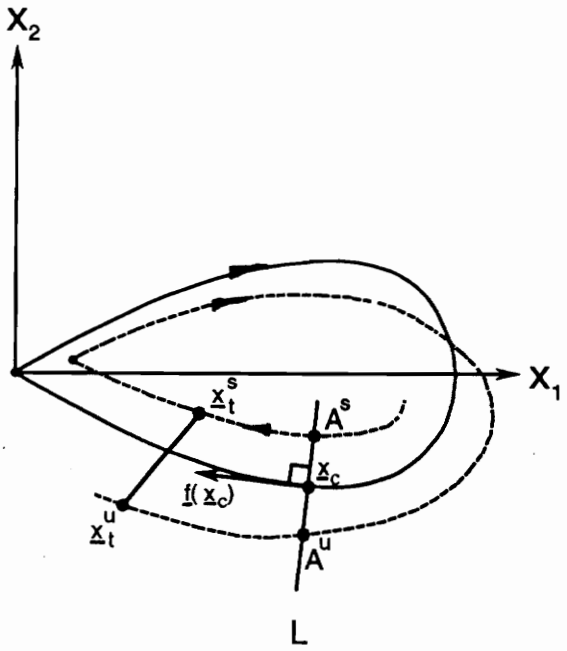

(a)

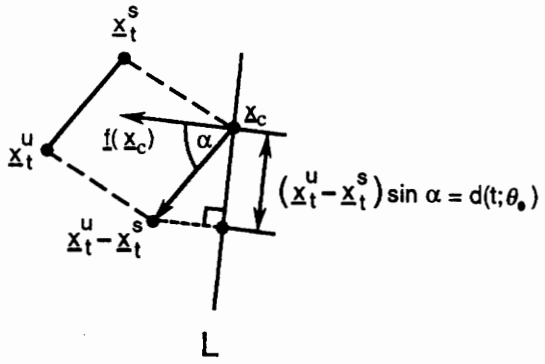

(b)

Figure 4.3. Time-Dependent Distance Function: Construction of the time-dependent distance function $d(t;\theta_0)$ is shown. (a) The points A^s and A^u represent the points on each of the stable and unstable manifolds closest to the point $\underline{x}_c$. They are defined to occur at the elapsed time $t = \theta_0$. Two other arbitrary trajectories ($\underline{x}_t^s$ and $\underline{x}_t^u$) with $t > \theta_0$ are shown as well. Note that the vector $\underline{f}(\underline{x}_c)$ is the time derivative of $\underline{x}$ evaluated at $\underline{x}_c$ and is thus tangent to the curve at that point. (b) The projection of the separation between the two arbitrary trajectories along L is clearly the labelled quantity $(\underline{x}_t^u - \underline{x}_t^s)\sin\alpha$; hence the definition of $d(t;\theta_0)$.

respective locations A^s and A^u when $t = \theta_0$. While the curves may intersect L more than once, the points A^s and A^u are those closest to the point $\underline{x}_c$. If the time t is fixed at θ_0, the distance between the manifolds projected along L is simply the separation vector $\underline{x}^u(\theta_0; \theta_0) - \underline{x}^s(\theta_0; \theta_0)$. If the time t is no longer constrained to be θ_0, the distance between the manifolds projected along the line L may be expressed as a function of time. Note that this distance is *by definition* minimized for the particular section and value of $\underline{x}_c$ we chose if t is set equal to θ_0. However, we wish to consider *all* locations on every possible Poincaré section to conclusively determine whether transverse intersections occur in the perturbed system. To do this, we need to examine the function d, which depends both on the time t and the section θ_0 and is defined as

$$d(t; \theta_0) \equiv \frac{\underline{f}(\underline{x}_c(t - \theta_0)) \wedge (\underline{x}^u(t; \theta_0) - \underline{x}^s(t; \theta_0))}{|\underline{f}(\underline{x}_c(t - \theta_0))|} \qquad [4.2]$$

The symbol "$\wedge$" denotes a vector cross product of which only the magnitude is significant. Its computation is identical to the standard cross product identified by the "$\times$" symbol, except that the result is a scalar rather than another vector. With this definition in mind, the truth of Equation [4.2] may be readily established through examination of the geometry presented in Figure 4.3. Although our interest in the function $d(t; \theta_0)$ concerns only the value at the time $t = \theta_0$, since that is by definition when the manifolds approach most closely for the section $\theta = \theta_0$, the definition of d as a time-dependent function is necessary to transform the crucial value, $d(\theta_0; \theta_0)$, from a function of the perturbed manifolds (through the trajectories $\underline{x}^u$ and $\underline{x}^s$), to a function of only the unperturbed manifolds.

The existence of real zeros of the function $d(\theta_0; \theta_0)$ in the interval $(0, 2\pi/\Omega]$ indicates conclusively that transverse intersections are predicted to occur. This fact is most easily appreciated by considering the three-dimensional continuous-time perturbed manifolds introduced in Section 3.1. If two manifolds are to intersect, they must do so in a one-dimensional homoclinic trajectory, a curve that converges to the path traced by the saddle point of the Poincaré map as the section varies. Because every point on the stable (unstable) manifold will eventually approach the

trajectory of the perturbed saddle point $\underline{x}^*$ as the system moves forward (backward) in time, any point on an intersection of the manifolds will approach the perturbed saddle trajectory as time moves either forward or backward in time. The implication is that an intersection point will travel roughly "around" the homoclinic orbit of the unperturbed system. Because only the Poincaré sections defined by one repetition of the interval $(0, 2\pi/\Omega]$ are unique, all of the information about the journey of the intersection point in question around the homoclinic orbit must be contained in these sections. The conclusion is that the arbitrary choice $\underline{x}_c$ where we decided to draw the perpendicular L is unimportant; if all nonredundant values of θ_0 are considered, then any existing transverse intersections will pass through that section and be detected by our calculation of $d(\theta_0; \theta_0)$.

The next step in developing the Melnikov function consists of expressing the trajectories $\underline{x}^u$ and $\underline{x}^s$ in terms of only unperturbed quantities. To this end, we consider the function Δ_ε, which is related to the function $d(t; \theta_0)$ and is defined as

$$\Delta_\varepsilon(t; \theta_0) \equiv \underline{f}(\underline{x}_c(t - \theta_0)) \wedge (\underline{x}^u(t; \theta_0) - \underline{x}^s(t; \theta_0)) \qquad [4.3]$$

We expand the perturbed quantities $\underline{x}^u$ and $\underline{x}^s$, writing

$$\underline{x}^{u,s}(t; \theta_0) = \underline{x}_c(t - \theta_0) + \varepsilon \underline{x}_1{}^{u,s}(t; \theta_0) + O(\varepsilon^2) \qquad [4.4]$$

Next we substitute the expansion into the governing differential equation, [4.1], separate powers of ε, and obtain

$$\varepsilon^0: \quad \dot{\underline{x}}_c(t - \theta_0) = \underline{f}(\underline{x}_c(t - \theta_0))$$

$$\varepsilon^1: \quad \dot{\underline{x}}^{u,s}(t; \theta_0) = D\underline{f}(\underline{x}_c(t - \theta_0))\underline{x}_1{}^{u,s}(t; \theta_0) + \underline{g}(\underline{x}_c(t - \theta_0), t) \qquad [4.5]$$

At the same time, we also substitute the expansions of Equation [4.4] into the expression for Δ_ε (Equation [4.3]) which results in

$$\Delta_\varepsilon(t;\theta_0) = \underline{f}(\underline{x}_c(t-\theta_0)) \wedge \varepsilon \underline{x}_1{}^u(t;\theta_0) - \underline{f}(\underline{x}_c(t-\theta_0)) \wedge \varepsilon \underline{x}_1{}^s(t;\theta_0) + O(\varepsilon^2) \qquad [4.6]$$

For convenience, the two terms on the right-hand side above are defined, respectively, as $\Delta_\varepsilon^u(t;\theta_0)$ and $\Delta_\varepsilon^s(t;\theta_0)$. Differentiating each quantity with respect to the time t yields, after some manipulation,

$$\dot{\Delta}_\varepsilon^{u,s}(t;\theta_0) = \varepsilon Tr[D\underline{f}(\underline{x}_c(t-\theta_0))]\underline{f}(\underline{x}_c(t-\theta_0)) \wedge \underline{x}_1{}^{u,s}(t;\theta_0) + \varepsilon \underline{f}(\underline{x}_c(t-\theta_0)) \wedge \underline{g}(\underline{x}_c(t-\theta_0),t) \qquad [4.7]$$

Because $\dot{\underline{x}} = \underline{f}(\underline{x})$ is Hamiltonian, the quantity $Tr[D\underline{f}(\underline{x})]$ is identically zero (Wiggins [1990]). As a consequence, Equation [4.7] may be simplified to

$$\dot{\Delta}_\varepsilon^{u,s} = \varepsilon \underline{f}(\underline{x}_c(t-\theta_0)) \wedge \underline{g}(\underline{x}_c(t-\theta_0),t) \qquad [4.8]$$

Integration produces

$$\Delta_\varepsilon^u(\theta_0;\theta_0) - \Delta_\varepsilon^u(-\infty;\theta_0) = \int_{-\infty}^{\theta_0} \varepsilon \underline{f}(\underline{x}_c(t-\theta_0)) \wedge \underline{g}(\underline{x}_c(t-\theta_0),t)\, dt \qquad [4.9]$$

$$\Delta_\varepsilon^s(+\infty;\theta_0) - \Delta_\varepsilon^s(\theta_0;\theta_0) = \int_{\theta_0}^{+\infty} \varepsilon \underline{f}(\underline{x}_c(t-\theta_0)) \wedge \underline{g}(\underline{x}_c(t-\theta_0),t)\, dt \qquad [4.10]$$

The quantities $\Delta_\varepsilon^u(-\infty;\theta_0)$ and $\Delta_\varepsilon^s(+\infty;\theta_0)$ both reduce to $\underline{f}(\underline{x}_c^*) \wedge \varepsilon \underline{x}^*$, meaning that we can add the last two equations, substitute the result into Equation [4.6], and write

$$\Delta_\varepsilon(\theta_0;\theta_0) = \int_{-\infty}^{+\infty} \varepsilon \underline{f}(\underline{x}_c(t-\theta_0)) \wedge \underline{g}(\underline{x}_c(t-\theta_0),t)\, dt + O(\varepsilon^2) \qquad [4.11]$$

This simplified result leads us to define the Melnikov function as

$$M(\theta_0) = \int_{-\infty}^{+\infty} \underline{f}(\underline{x}_c(t-\theta_0)) \wedge \underline{g}(\underline{x}_c(t-\theta_0), t)\, dt \qquad [4.12]$$

The functional dependence in this equation is solely on the section level θ_0 ($0 < \theta_0 \leq 2\pi/\Omega$). We note that $M(\theta_0)$ is approximately proportional to $d(\theta_0;\theta_0)$ and can thus be used to predict transverse manifold intersections.

4.2 Calculation of the Melnikov Function

As noted in the last section, the distance between the manifolds is converted from a function of the perturbed manifolds to a function only of the conservative trajectories (i.e., the homoclinic or heteroclinic orbit of interest). In the following sections, we detail the procedure used to compute these trajectories and subsequently $M(\theta_0)$ for the ship-roll model.

4.2.1 Homoclinic Tangles

In this instance, the relevant conservative orbit is, of course, homoclinic in nature; recall that Figure 2.5 contains an illustration of two such orbits. Evaluating the Melnikov integral first

requires the evaluation of $\underline{f}$ and $\underline{g}$ in terms of the homoclinic trajectory. For the roll model of Equation [2.19], substitution into Equation [4.12] yields

$$M(\theta_0) = -\int_{-\infty}^{+\infty} [\mu_1 x_{c_2}{}^2 + \mu_3 x_{c_2}{}^4 + h x_{c_1} x_{c_2} \cos(\Omega(t - \theta_0))]\, dt \qquad [4.13]$$

For the double-subscripted quantities above, the first subscript ("c") denotes the use of the (conservative) homoclinic orbit while the second subscript refers to the vector component. Actual computation of the integral in Equation [4.13] requires a numerical representation for the homoclinic trajectory $\underline{x}_c(t - \theta_0)$. This curve may be approximately computed by numerically integrating the conservative equation, [2.21], from an initial guess point $\underline{x}_g$ inside the homoclinic curve and near the unperturbed saddle point $\underline{x}_c^*$ to some final point also near $\underline{x}_c^*$. This procedure is pictured schematically in Figure 4.4.

Practically, the integral over $(-\infty, +\infty)$ may be carried out by applying the trapezoidal rule (or other numerical integration technique) with an appropriate step size Δt between the two points established as the "beginning" and "end" of the orbit. Note that Δt is fixed implicitly by the calculation of the homoclinic curve; the time step cannot be freely chosen in the computation of Equation [4.13], but must be selected during the calculation of the conservative orbit. In addition, although the two endpoints of the interval are theoretically both identical to the unperturbed saddle $\underline{x}_c^*$, we must use approximations at either end of the trajectory to compute M; use of the exact saddle point will result in the degenerate trajectory consisting only of the saddle itself.

4.2.2 Heteroclinic Tangles

If the potential intersection is heteroclinic in nature, the procedure is similar. The only difference is that the conservative curve is not a homoclinic orbit, but a heteroclinic half-orbit. Such a curve proceeds from one unperturbed saddle point to another. For a single heteroclinic circuit,

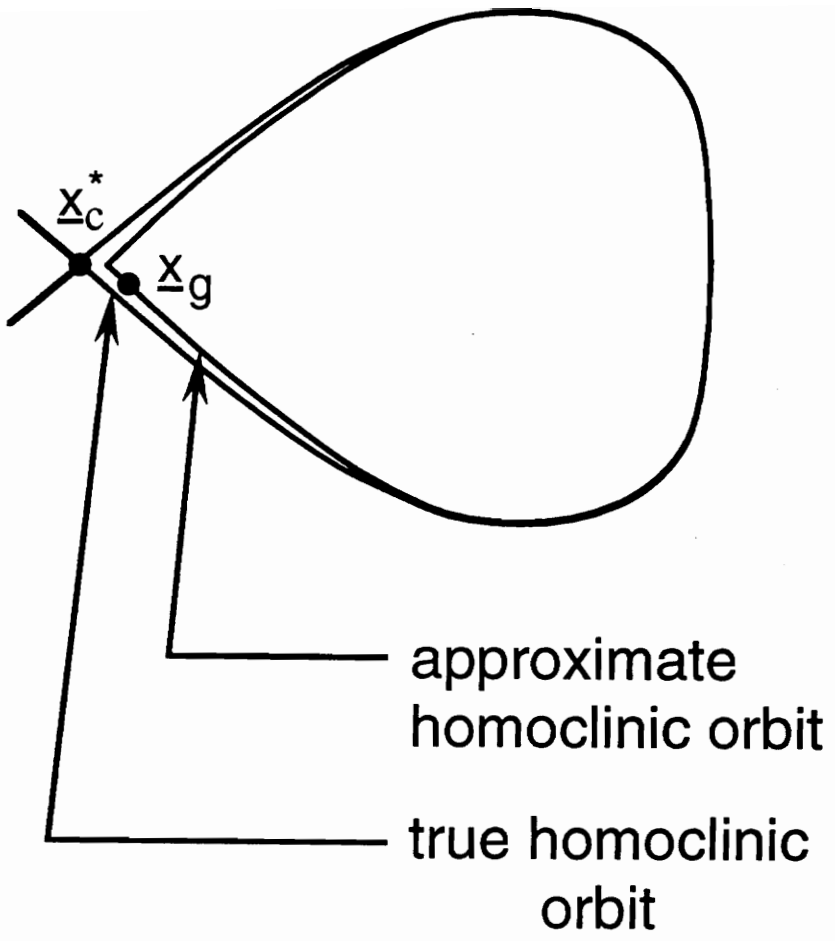

Figure 4.4. Approximate Homoclinic Trajectory: The homoclinic orbit is approximated by selecting an initial guess point $\underline{x}_g$ near the unperturbed saddle $\underline{x}_c^*$ and inside the homoclinic orbit and then integrating numerically until the curve closes on itself.

two such trajectories exist, as shown in Figure 4.5. As might be intuitively expected, the use of the upper curve in Figure 4.5 in the Melnikov integral will lead to the detection of the intersection between the unstable manifold of the left saddle point and the stable manifold of the right saddle point. Analogously, the lower curve corresponds to intersections of the left stable and right unstable manifolds.

4.2.3 Mixed Tangles

If it is possible to detect both homoclinic and heteroclinic intersections using the Melnikov function, what about finding mixed intersections? The occurrence of intersections of one heteroclinic manifold and one homoclinic manifold has been documented in the work of Falzarano [1990]. However, a review of the pertinent literature seems to suggest that no one has used the Melnikov function to predict these intersections. In fact, Falzarano [1990] indicates that he does "...not yet see a way to determine the...Melnikov function [for predicting homoclinic-heteroclinic intersections]."

We now discuss a fruitful approach to solving this problem. The key to computing the Melnikov function for predicting mixed intersections lies with the choice of unperturbed trajectory over which the computation occurs. In the homoclinic case, the manifolds that intersect correspond to an unperturbed homoclinic orbit, the curve along which Melnikov's function is calculated. Similarly, in the heteroclinic case, the intersecting manifolds originate from a heteroclinic half-orbit, which is used to compute $M(\theta_0)$. For detecting mixed tangles, then, it seems reasonable to use in the Melnikov integral the unperturbed manifolds that later result in a mixed intersection when the perturbation is added. A trajectory that closely approximates a homoclinic orbit *and* a heteroclinic half-orbit fits this description; an example of such a trajectory is illustrated in Figure 4.6. Other than the selection of the unperturbed trajectory, the computational procedure is identical to that used in the homoclinic and heteroclinic cases described in Sections 4.2.1 and 4.2.2.

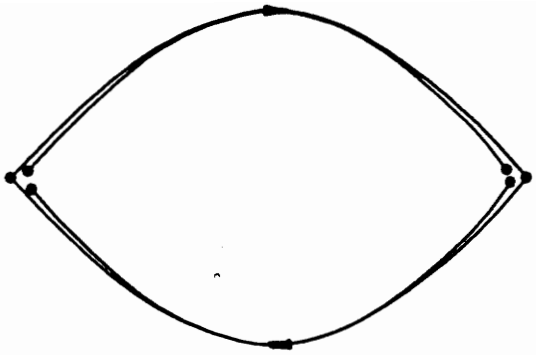

Approximate Heteroclinic Trajectories

(a)

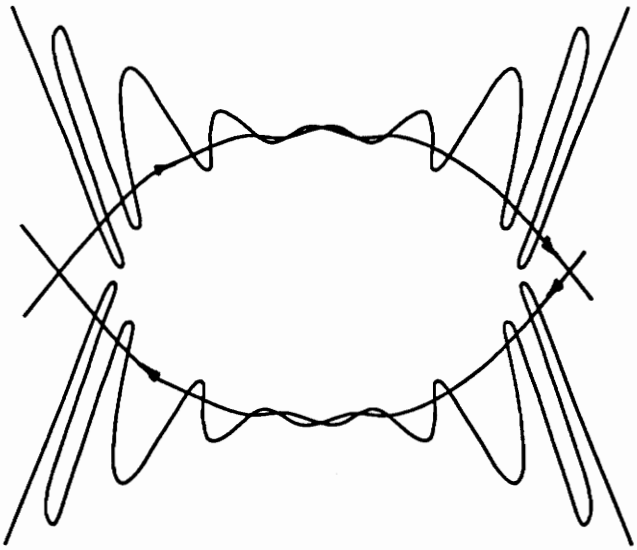

Associated Perturbed Manifolds

(b)

Figure 4.5. **Approximate Heteroclinic Trajectories:** A heteroclinic orbit has two possible approximations for use in computing the Melnikov function. The use of the upper inside curve in (a) predicts the intersections of the two upper curves in (b), while the lower inside curve in (a) forecasts the intersections of the lower two curves in (b). Note that as for the homoclinic case, the beginning and end points of the approximate trajectories must lie near the corresponding saddle points.

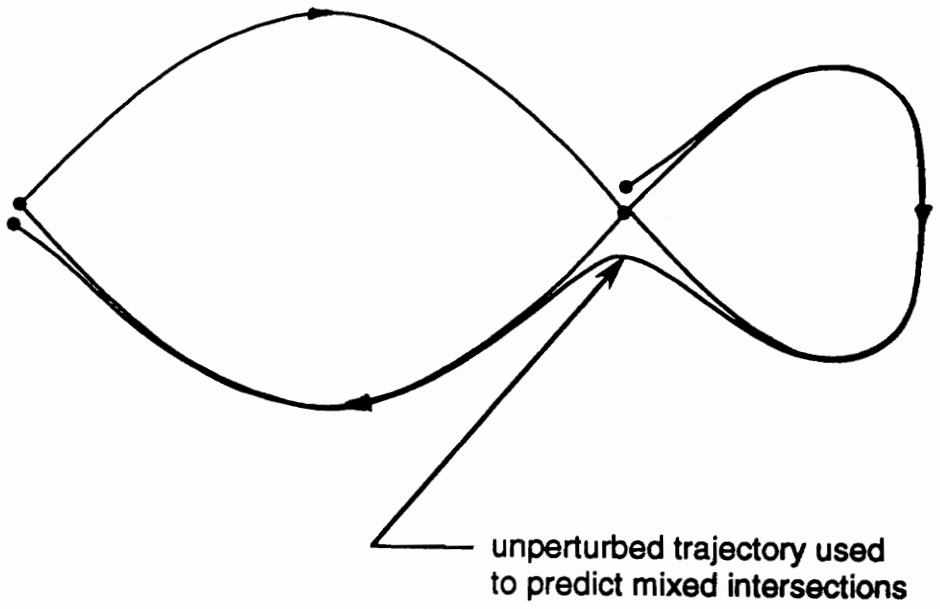

Figure 4.6. Unperturbed Trajectory Used for Predicting Mixed Tangles: Pictured is the unperturbed trajectory used in the Melnikov integral when predicting intersections of one homoclinic manifold and one heteroclinic manifold in the perturbed map.

4.3 *Examples of Melnikov Computations*

To confirm the numerical schemes used in implementing the computational procedures discussed in this chapter, we apply Melnikov's method (as detailed in Section 4.2.1) to the Duffing equation in the form specified in the last chapter:

$$\ddot{x} + \mu\dot{x} + x - x^3 = F\cos(\Omega t) \qquad [4.14]$$

Recall now the invariant manifolds computed for this equation in the last chapter. In Figure 3.9 ($\mu = 0.125$, $F = 0.19$), the manifolds intersect tangentially or are very close to doing so. As a consequence, we expect the Melnikov function to be close to acquiring a root. In other words, the absolute values of the function M should have as their minimum a value very close to zero. The graph in Figure 4.7 confirms our expectations: for the same values of μ and F used in Chapter 3, the Melnikov function has a minimum very close to zero. As further validation of the technique, the Melnikov function is also plotted for the first case treated in Chapter 3, which corresponds to Figure 3.8 ($\mu = 0.125$, $F = 0.11$). Because the manifolds in Figure 3.8 do not intersect transversely, we expect that the Melnikov function will have no impending roots; Figure 4.8 verifies this assumption. Due to these two examples, we proceed to Chapter 5 and an analysis of the ship-roll equation with confidence in the numerics used to calculate both invariant manifolds and the Melnikov function.

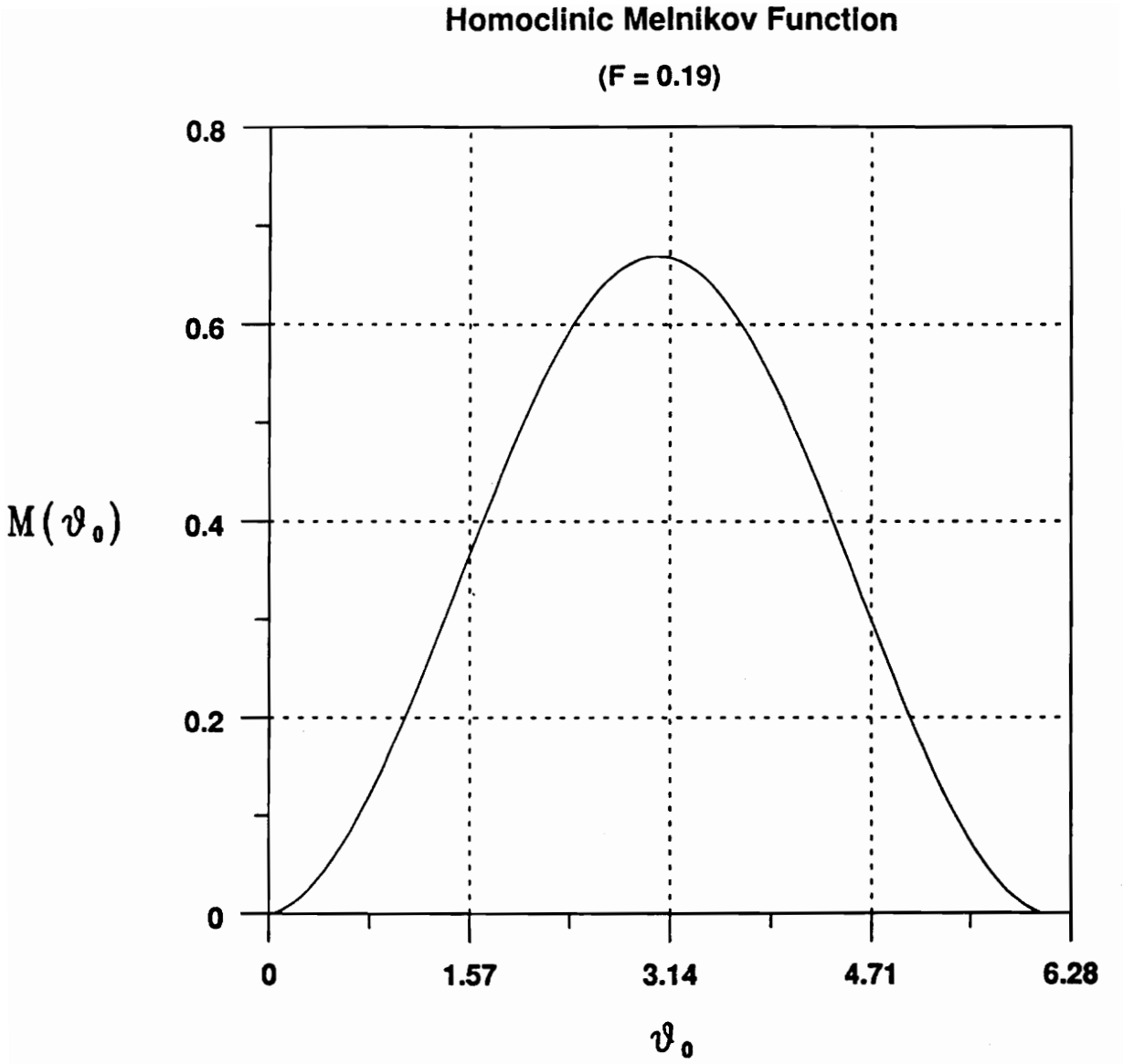

Figure 4.7. Melnikov Function for the Duffing Equation (F = 0.19): The Melnikov function has a minimum very close to zero when manifold intersections first occur.

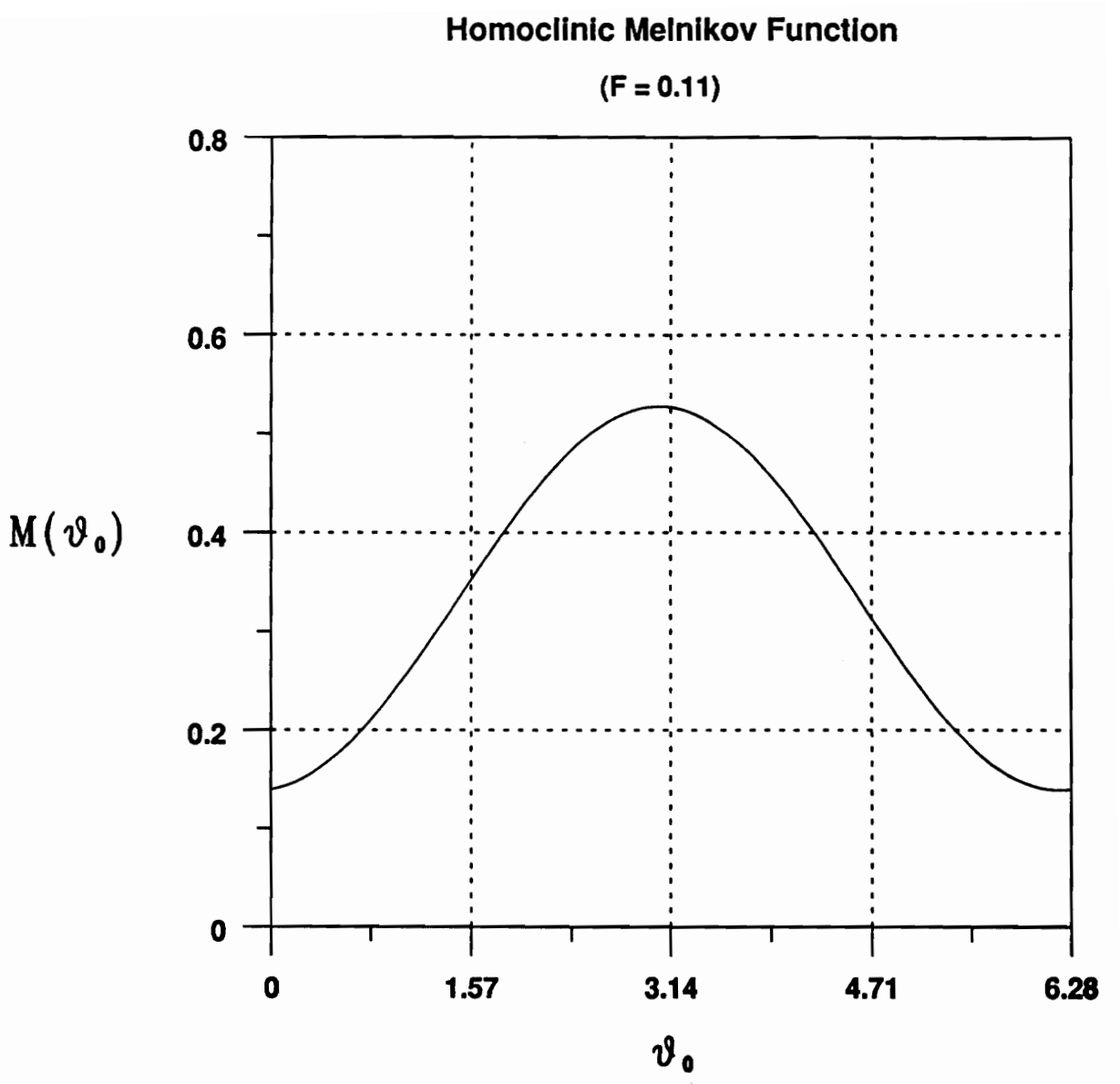

Figure 4.8. Melnikov Function for the Duffing Equation (F = 0.11): The minimum of the function is far from zero when intersections are not approaching.

5. Results for the Ship-Roll Model

In the following sections, we apply the techniques developed in the last two chapters to the ship-roll model as described by Equation [2.19]. Invariant manifolds and Melnikov predictions are computed for a "base case," defined by specifying selected values for the damping and restoring-moment coefficients. The onset of fractally mixed two-dimensional phase space, which is forecast by both transverse manifold intersections and the corresponding Melnikov prediction, is explored for this case by computing a number of transient basins. Then, the effect of changing each of the damping and restoring-moment parameters is studied through an extensive Melnikov analysis. We partially validate this parameter study by examining several other transient basins.

Before proceeding, we transform the single-degree-of-freedom equation to nondimensional form. This is accomplished by changing the dependent variable in Equation [2.19] to $\tau = \omega_0 t$, resulting in

$$\phi'' + \phi + \left(\frac{\alpha_3}{{\omega_0}^2}\right)\phi^3 + \left(\frac{\alpha_5}{{\omega_0}^2}\right)\phi^5 + \left(\frac{\mu_1}{\omega_0}\right)\phi' + \mu_3\omega_0\phi'^3 + \left(\frac{h\phi}{{\omega_0}^2}\right)\cos\left(\frac{\Omega}{\omega_0}\tau\right) = 0 \quad [5.1]$$

where

τ = nondimensional time

$(\,)'$ = derivative with respect to τ

Because the time has been scaled with the linear natural frequency, problems having different values of ω_0 are all described by Equation [5.1]. Any result generated in the following sections may be interpreted as applying to systems with other values of ω_0 by scaling the damping and restoring-moment coefficients according to Equation [5.1]. In the following sections, however, we consider only the condition of primary resonance. For simplicity, both frequencies are equated to unity. In the presence of this restriction, Equations [2.19] and [5.1] are identical descriptions.

5.1 Base Case

5.1.1 Determination of Parameter Values

In order to calculate invariant manifolds and the Melnikov function, we must specify concrete values for the parameters of the system: both damping coefficients (μ, μ_3), the cubic and quintic restoring-moment coefficients (α_3, α_5), and the excitation amplitude (h).

Because experimental studies of the single-degree-of-freedom equation as a model for ship roll are not extensive, choosing reasonable values for use in Equation [2.19] is itself not a trivial matter. We consider first the graph reprinted in Wright and Marshfield [1980], which depicts linear and cubic damping coefficients as a function of ship speed for "'normal' damping for [a] 50 metre ship." These graphs were obtained from model experiments carried out by the Admiralty Marine Technology Establishment, and thus represent "reasonable" values. However, the computed coefficients do not refer to the linear-plus-cubic damping model that we are employing here, but (presumably) to independent linear and cubic damping models. Although use of values from this graph might be questionable for comparing with any experimental data directly, it is probably acceptable for our purpose: establishing the viability of invariant-manifold and Melnikov analyses. Consequently, we arbitrarily select the following values:

$$\mu_1 = 0.2 \quad \text{(corresponds to } g_1 \text{ in graph)} \qquad [5.2]$$

$$\mu_3 = 0.2 \quad \text{(corresponds to } g_3 \text{ in graph)} \qquad [5.3]$$

Although graphical representations of restoring-moment curves (also called GZ curves) were found in the literature, few researchers listed appropriate values for the coefficients in the polynomial approximation we use in this work. However, it seems that the primary effect of the two parameters may be appreciated solely by examining the conservative separatrices, an example of which we saw in Figure 2.5. Changing α_3 and α_5 affects the existence and location of the saddle points, and the resulting shape of the associated phase trajectories. Thus, we need only select values that generate the qualitative behavior desired. We seek to examine models with saddle points because they indicate a ship configuration that can lose stability (near the saddles). Through a trial and error procedure, the following values were found to generate the qualitative picture seen in Figure 2.5:

$$\alpha_3 = -1.9 \qquad [5.4]$$

$$\alpha_5 = 0.722 \qquad [5.5]$$

The only parameter remaining, the excitation amplitude h, represents the strength of the parametric forcing. For the derivation of Equation [2.19], it depends on the waterplane area, the distance of the center of mass of the ship from the waterline, and the transverse curvature radius of the center-of-flotation curve for constant displacement volume, all of which are geometric properties of the ship (Blocki [1980]). It also depends on the amplitude of heave, and thereby on wave amplitude. When we mention a particular value of h, these dependencies should be kept in mind. In the upcoming analysis, we allow h to vary until manifold intersections and the accompanying dynamic phenomena are observed. Because the geometry of the ship remains constant, only the wave amplitude changes as h is varied.

5.1.2 Invariant Manifold Computation (Base Case)

In this section, we examine the effects of increasing excitation amplitude on the invariant manifolds of the saddles of the Poincaré map for the model represented by Equation [2.19] with the parameter values specified in the last section. We begin with a low excitation level ($h = 0.05$); the corresponding manifold structure does not exhibit any intersections or other unusual characteristics. As shown in Figure 5.1, the manifolds resemble the trajectories of a damped, unforced phase portrait, although they represent something qualitatively different, as was mentioned in Section 3.1. Fixed-point solutions occur near $\phi = 0, \pm 1.35$. These solutions are fixed points of the Poincaré map and therefore correspond to periodic solutions of the original continuous-time equation.

When the forcing amplitude is increased to $h = 0.08$, the qualitative nature of the homoclinic manifolds changes, as is illustrated in Figure 5.2. Rather than spiraling smoothly to fixed points as they did in the previous case, the unstable homoclinic manifolds bend and twist as they spiral inward.

The bending and twisting of the homoclinic manifolds act as a precursor to transverse intersections, which are first observed for an excitation level very near $h = 0.085$. Illustrated in Figure 5.3, the intersections are pending at two different locations for each homoclinic structure: near the points $(\pm 0.2, \mp 1.1)$ and also near each of the saddles. We recall from Chapter 3 that the significance of the onset of these intersections is the concurrent incidence of fractal regions in the transient basin; this phenomenon is discussed in Section 5.1.4. The heteroclinic manifolds in this case remain qualitatively like the earlier cases, spiraling smoothly to a fixed point at the origin.

An excitation level of $h = 0.10$ is used to show more well-developed homoclinic manifold intersections. Several such crossings are clearly evident in Figure 5.4. By this time, it should be obvious that the Poincaré section for this system is symmetric about the origin, meaning that successive reflections of any point on the manifold structure across both coordinate axes generate a point also on the structure. (This behavior is due to the fact that Equation [2.19] is an odd function of both roll and roll velocity.) Consequently, any feature associated with one homoclinic

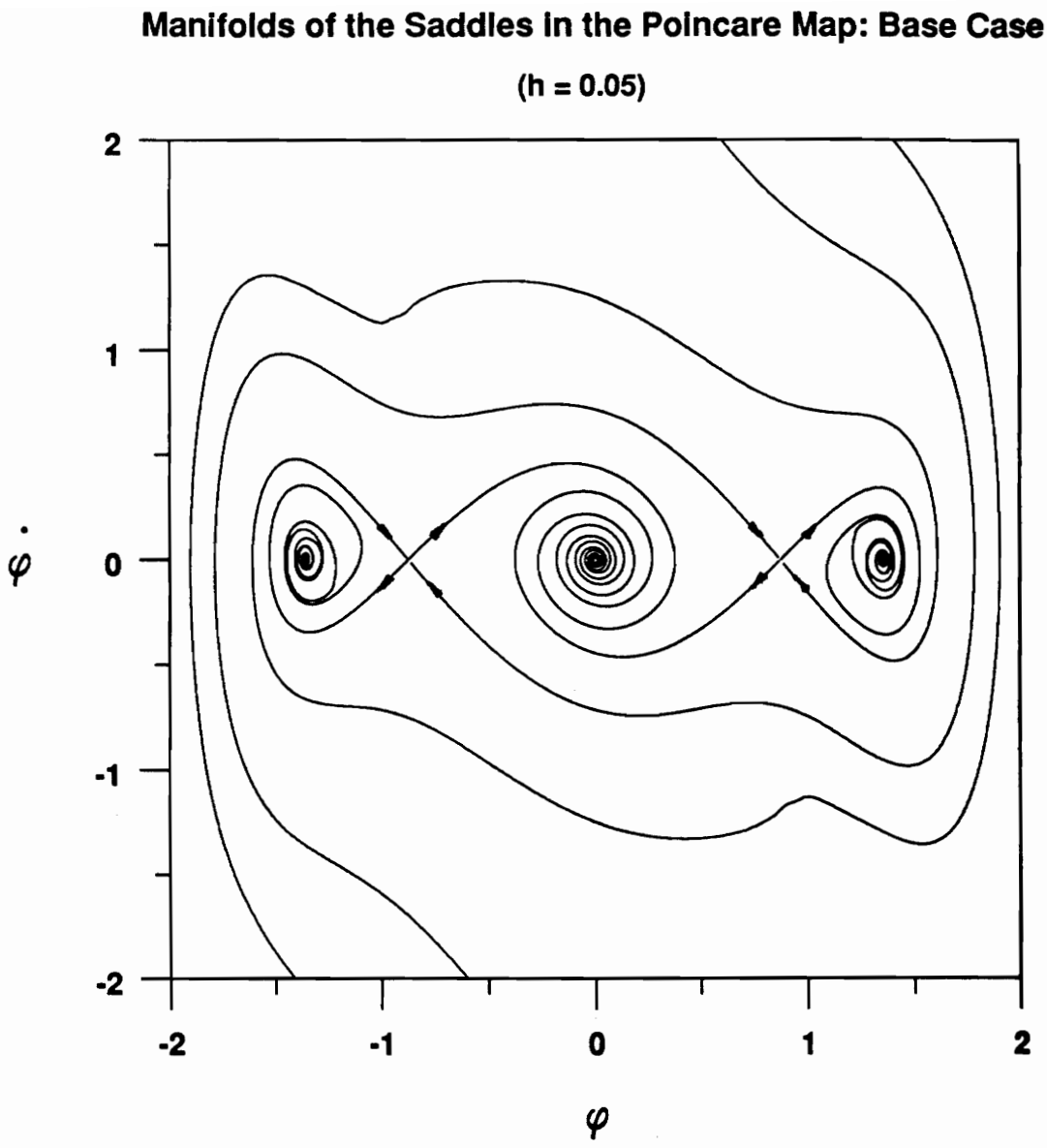

Figure 5.1. **Manifolds without Transverse Intersections:** For a low enough value of forcing amplitude, transverse intersections of the invariant manifolds in the Poincaré section do not occur.

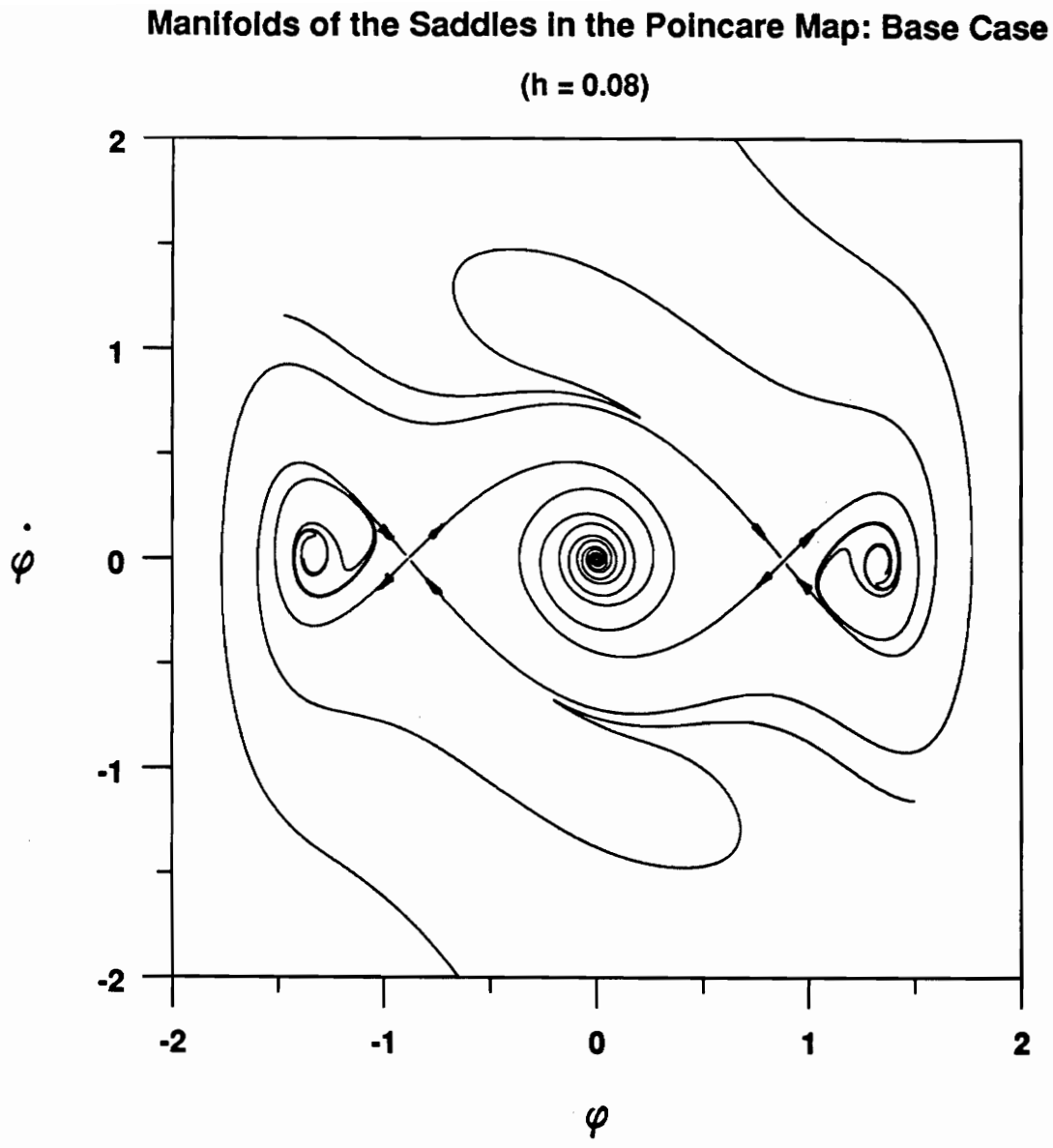

Figure 5.2. **Manifolds with Pending Homoclinic Intersections:** For this value of excitation amplitude, a change in the character of the manifolds is noticeable as homoclinic intersections approach.

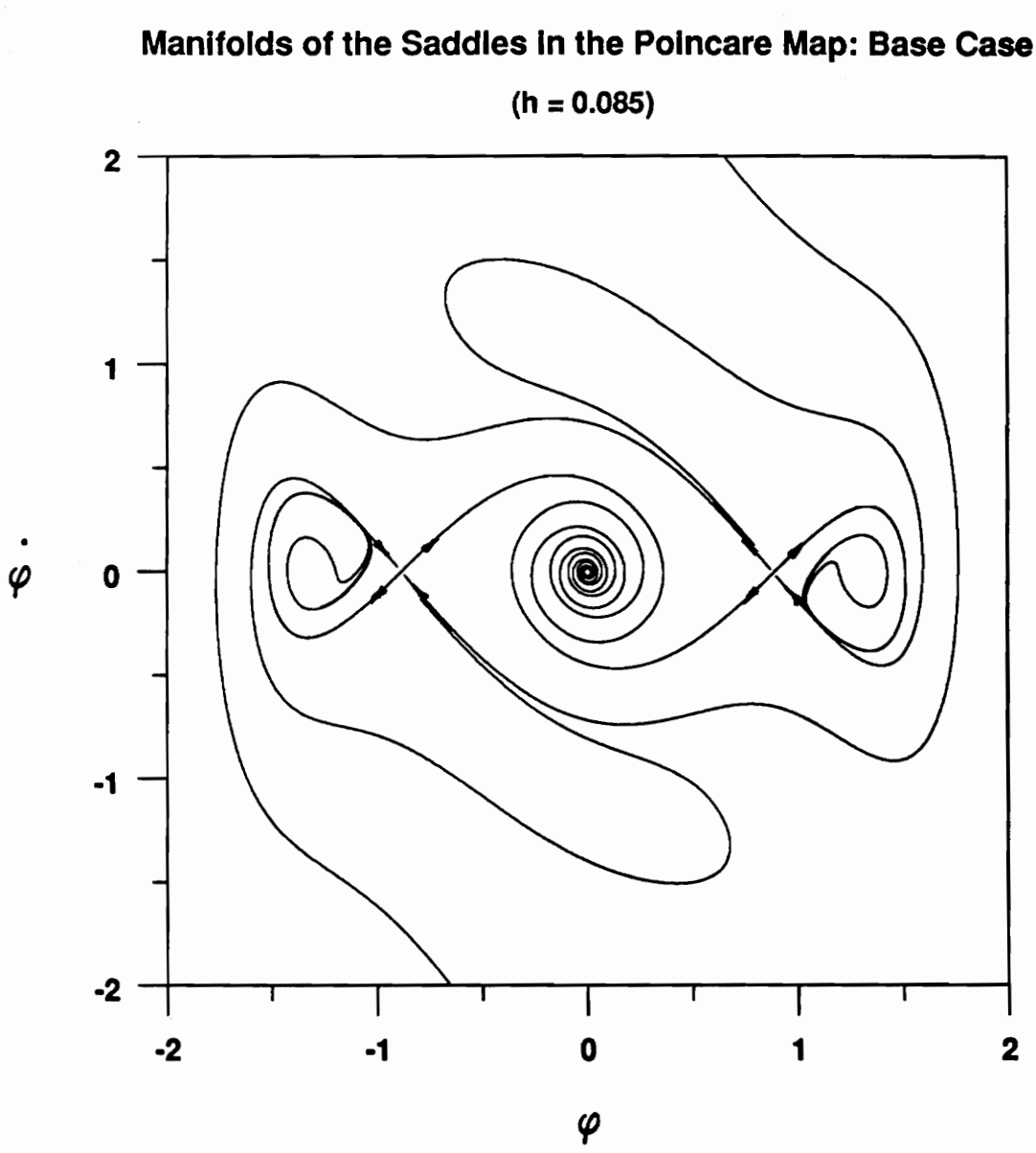

Figure 5.3. **Onset of Homoclinic Intersections in the Manifolds:** At a slightly larger forcing level than in Figure 5.2, homoclinic tangles begin to occur.

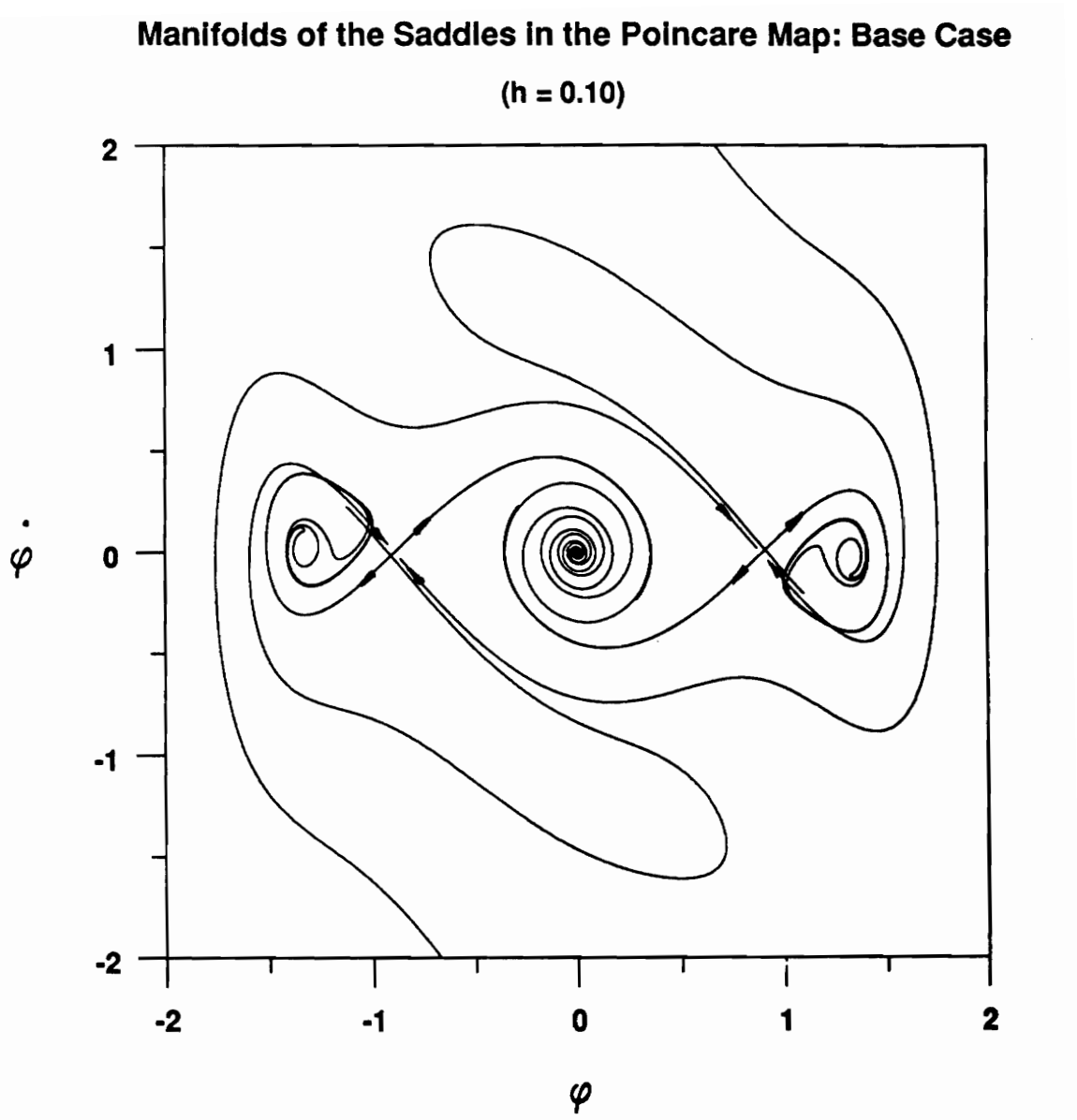

Figure 5.4. **Well-Developed Homoclinic Manifold Intersections:** With greater forcing, the manifolds intersect even more clearly.

manifold will also appear on the other. This symmetry will be taken for granted in the following development, in which only the left-most feature will be referenced.

Although we have now observed transverse intersections of the homoclinic manifolds, such a finding is usually not crucial to naval architects, since the homoclinic structures frequently occupy a part of the phase space that represents unacceptable operating conditions. For example, for the parameter values we chose in Section 5.1.1, the saddle points lie near ± 0.9 radians, or about $\pm 50°$. Of greater interest are heteroclinic intersections or perhaps (if they exist) "mixed" intersections between a homoclinic manifold and a heteroclinic manifold. Thus, we continue to increase the forcing amplitude h in search of these phenomena.

Observation of the manifold structure at $h = 0.215$ in Figure 5.5 reveals that mixed intersections *do* occur. The stable heteroclinic manifold intersects the unstable homoclinic manifold. This occurrence appears to indicate that the manifold structure of a roll model with parametric forcing and that of a model with only external excitation are fundamentally different. As evidence, consider the conjecture put forth by Falzarano [1990], who states:

> ...it seems reasonable that for unstable homoclinic and stable heteroclinic manifold intersections, the required wave amplitude (external forcing) must be greater than that for unstable heteroclinic and stable heteroclinic manifold intersections.

This situation obviously does not occur in the parametric case we are studying. At this point ($h \leq 0.215$), we have yet to observe heteroclinic intersections, although the stable heteroclinic-unstable homoclinic intersection was just pointed out in Figure 5.5. These manifold crossings could be particularly important, as they might give rise to what Falzarano [1990] calls "totally unexpected capsize." This concept will be further explored in Section 5.1.4.

Now we increase the excitation level to the point at which heteroclinic intersections finally begin: $h = 0.34$. These intersections are illustrated in Figure 5.6 and indicate that the safe area surrounding the origin could be starting to diminish rapidly (see Thompson [1991]). To summarize our progress, recall that homoclinic intersections were observed first at an excitation level of approximately 0.085, followed by mixed intersections at $h = 0.215$ and heteroclinic intersections at $h = 0.34$. This concludes our study of invariant manifolds for the base case; we proceed to test how well these different intersections are predicted by Melnikov's method.

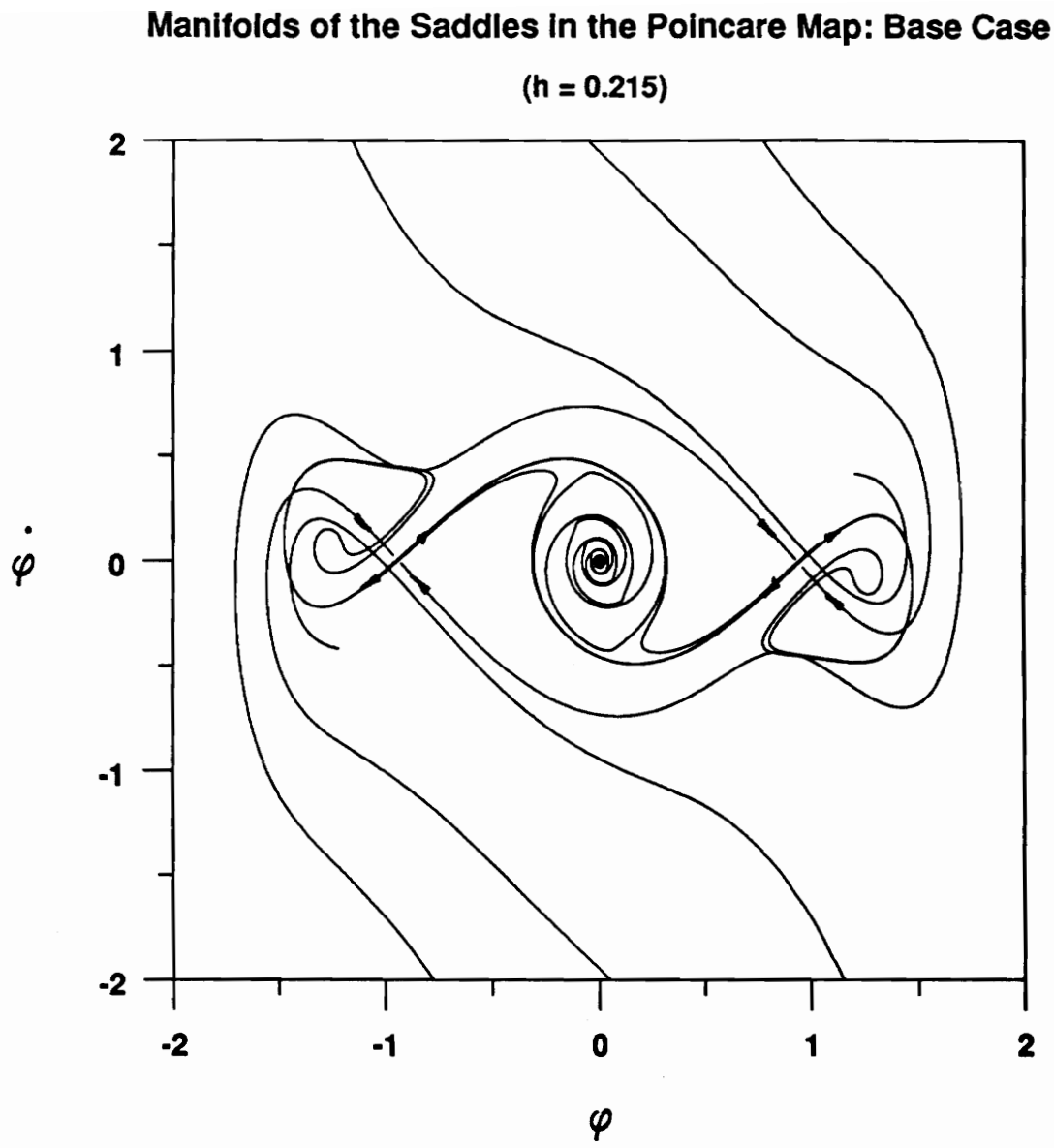

Figure 5.5. **Onset of Mixed Manifold Intersections:** Intersections of the stable heteroclinic and unstable homoclinic manifolds are initiated at a higher excitation amplitude than the homoclinic tangles illustrated previously.

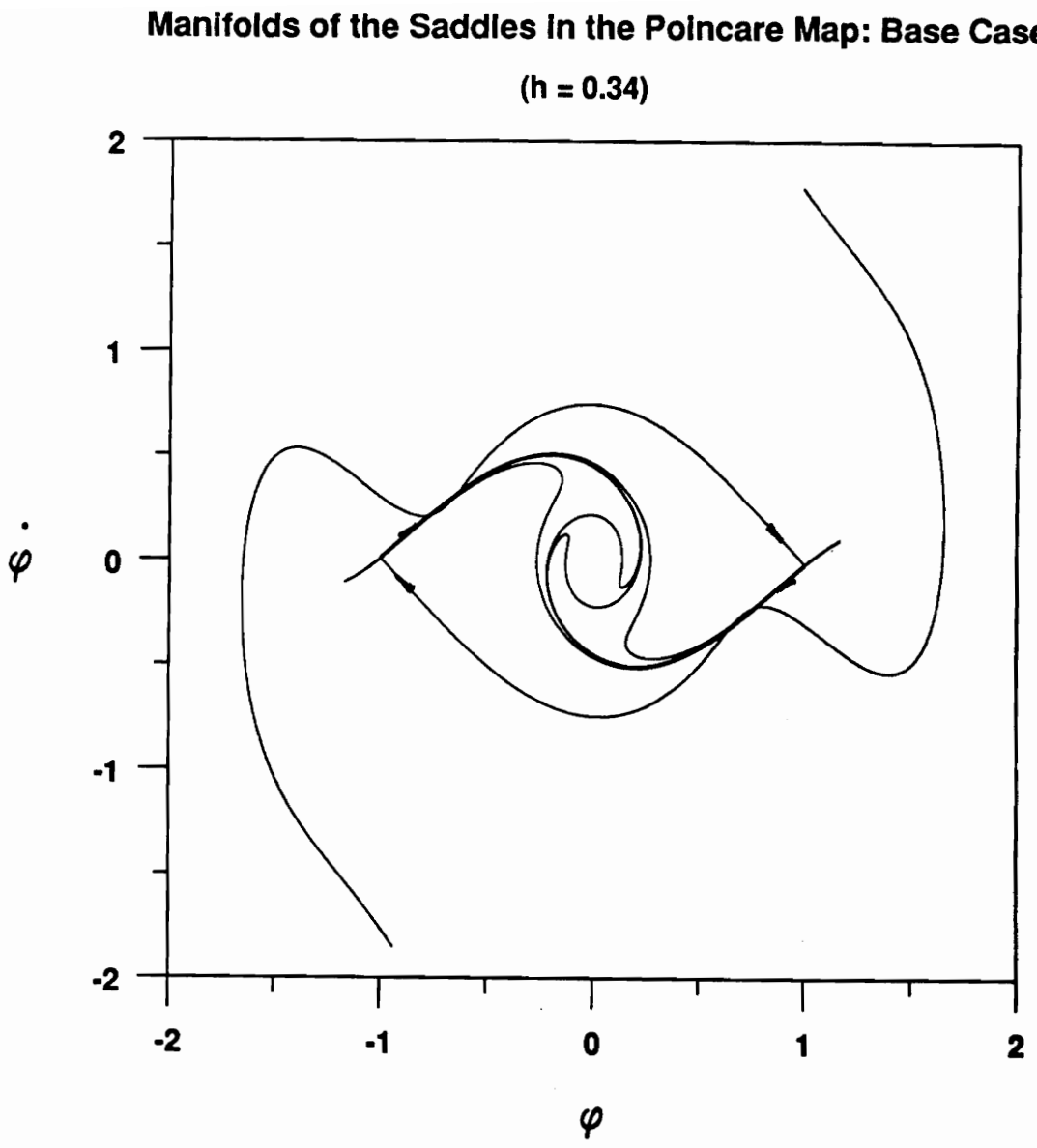

Figure 5.6. **Onset of Heteroclinic Manifold Intersections:** For this particular combination of parameter values (the base case), heteroclinic tangles begin to occur at a forcing level above those that first caused homoclinic and mixed intersections. Note that for clarity, the homoclinic manifolds have not been included in this picture.

5.1.3 Melnikov Analysis (Base Case)

We recall from Chapter 4 that the Melnikov function predicts transverse manifold intersections through the occurrence of simple roots in its domain (the period of the forcing function). If transverse intersections are imminent, then the Melnikov function is expected to take on minimum absolute values near zero.

We begin with the low-amplitude forcing for which invariant manifolds were computed ($h = 0.05$). In Figure 5.7, the Melnikov function for the homoclinic orbits is displayed; the calculation involved is an application of the technique described in Section 4.2.1. The variation of $M(\theta_0)$ is in qualitative agreement with the corresponding manifolds also shown in the figure: no intersections are pending and M does not approach zero.

Clear *quantitative* agreement between homoclinic Melnikov predictions and transverse homoclinic intersections is observed when the forcing is increased slightly. The Melnikov function is plotted for the values $h = 0.08$ and $h = 0.085$ in Figures 5.8 and 5.9. Note that the minimum absolute value of M begins to approach zero in these two figures; the companion manifolds shown below the plots of M exhibit impending intersections. These four pictures indicate that Melnikov's method is in some sense quantitatively correct in predicting the homoclinic tangles. Recall that our assignment of $\varepsilon = 1$ in Equation 4.1 was arbitrary; Melnikov's theory is effective if this parameter is small enough. The success of the method for the base case tends to indicate that $\varepsilon = 1$ is indeed small enough for our roll equation with base-case parameter values.

Further confirmation of Melnikov's method for the base case is sought by examining the heteroclinic intersections, which occur near $h = 0.34$. Once again, the variation of M (this time computed according to Section 4.2.2) closely parallels the approach of the stable and unstable manifolds. Heteroclinic tangles are approaching but yet to occur when $h = 0.32$. This behavior is predicted by the Melnikov function, pictured in Figure 5.10 along with the manifolds. In Figure 5.11, the incidence of heteroclinic intersections is definitely established, and the plot of M has two closely spaced roots, indicating a minimum near zero and thus good agreement.

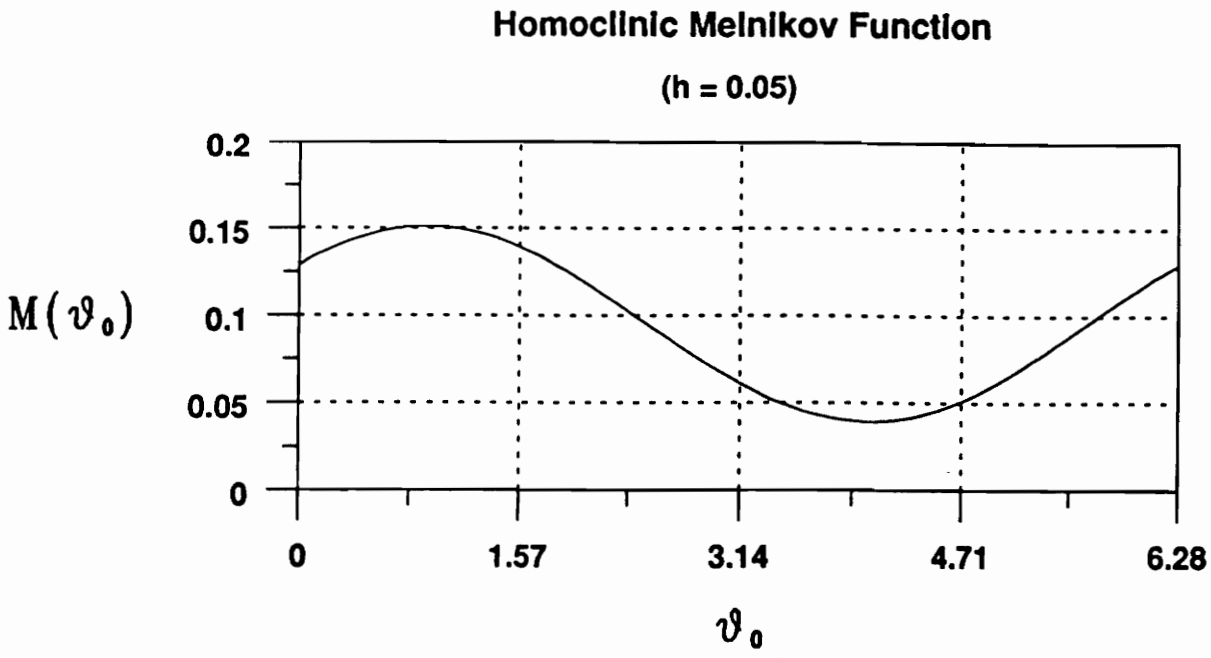

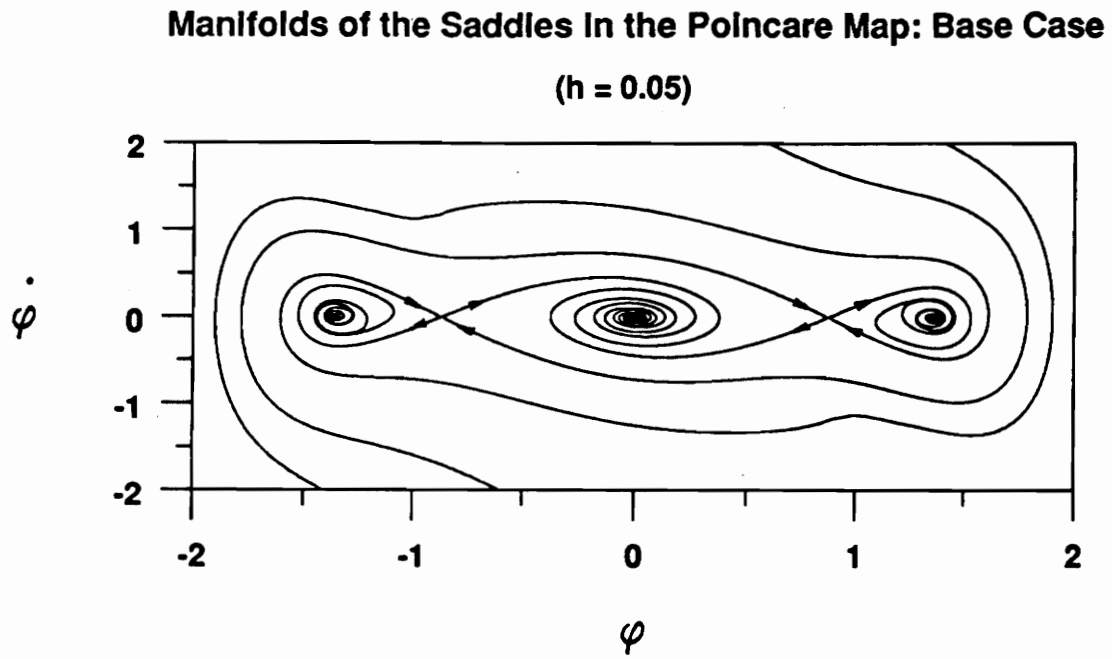

Figure 5.7. Homoclinic Melnikov Function (h = 0.05): The homoclinic Melnikov function for low forcing as expected does not approach zero.

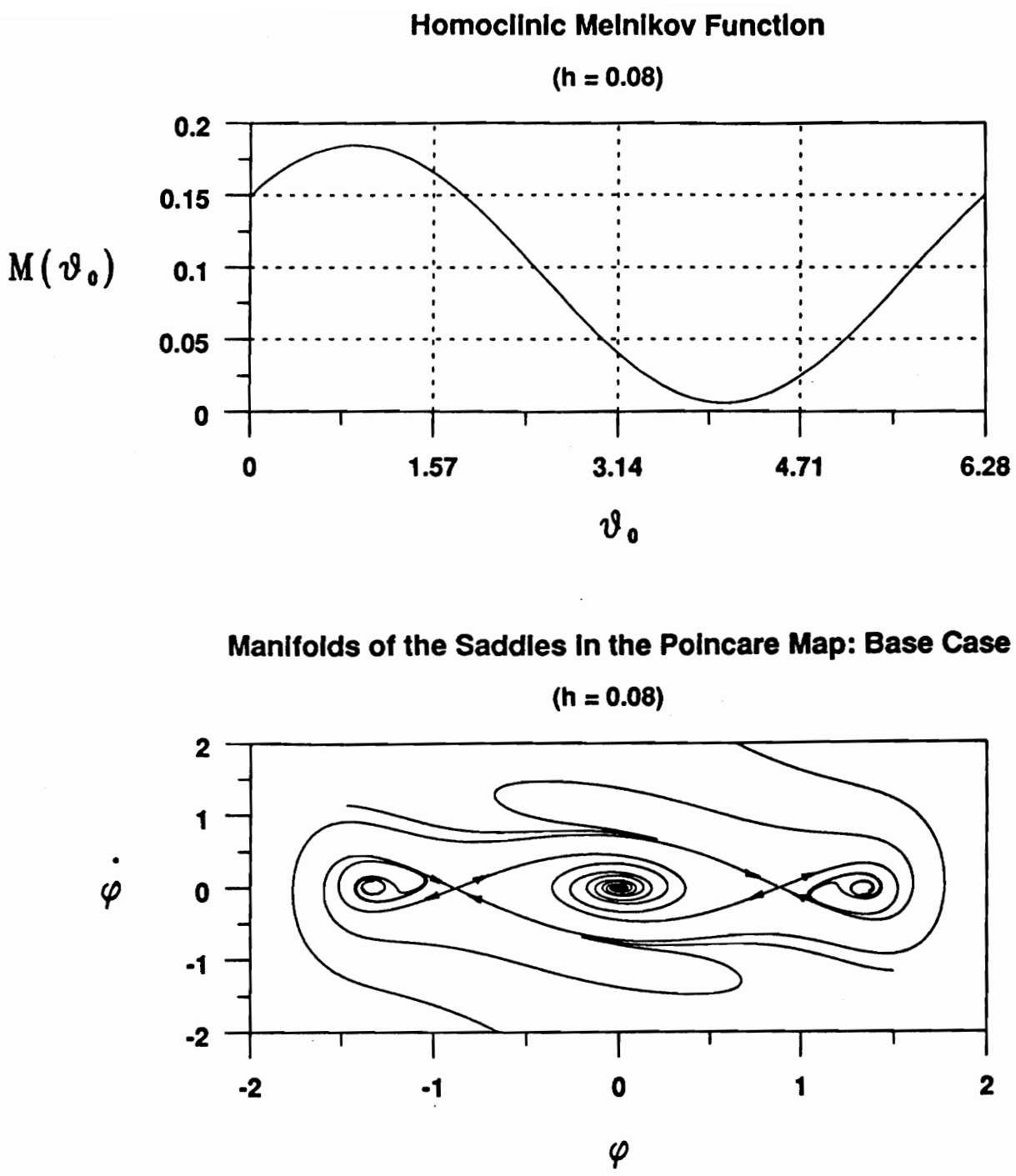

Figure 5.8. Homoclinic Melnikov Function (h = 0.08): The function has a minimum close to zero as homoclinic intersections approach.

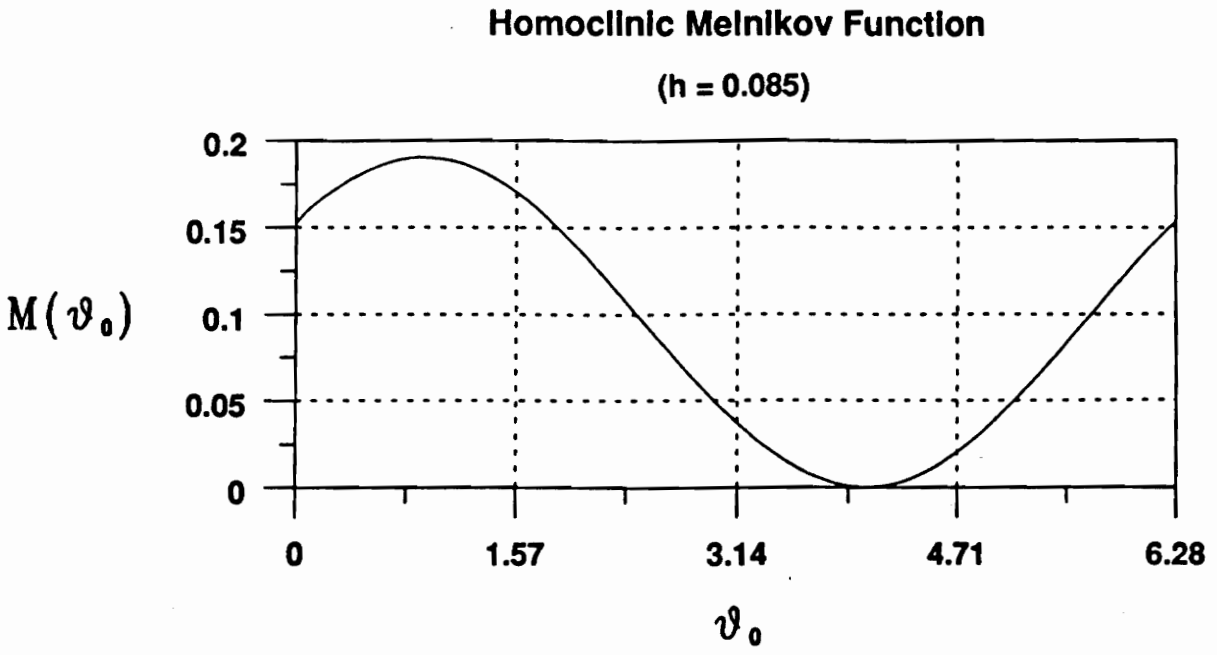

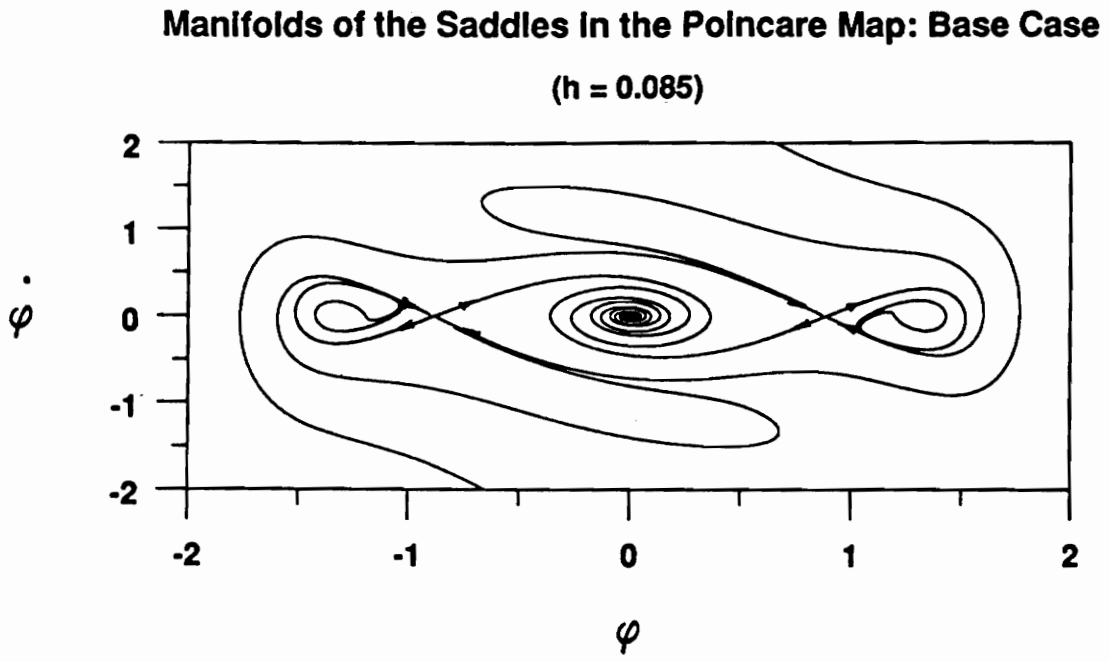

Figure 5.9. Homoclinic Melnikov Function (h = 0.085): As homoclinic intersections begin to occur, Melnikov's function acquires closely spaced roots.

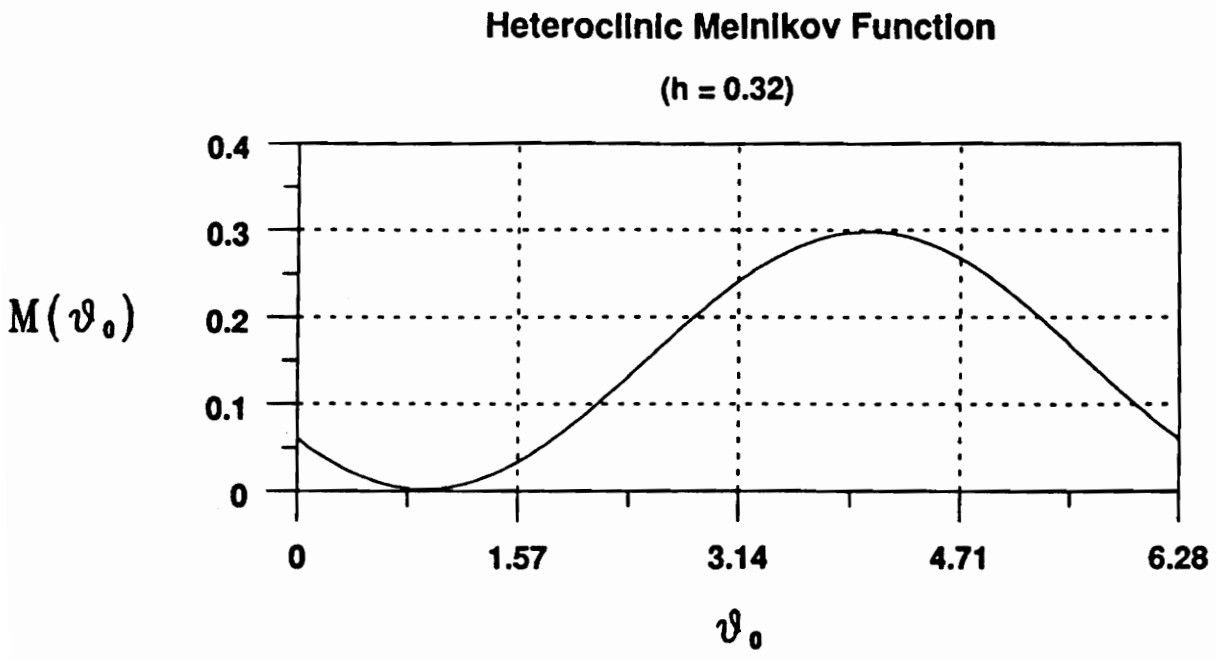

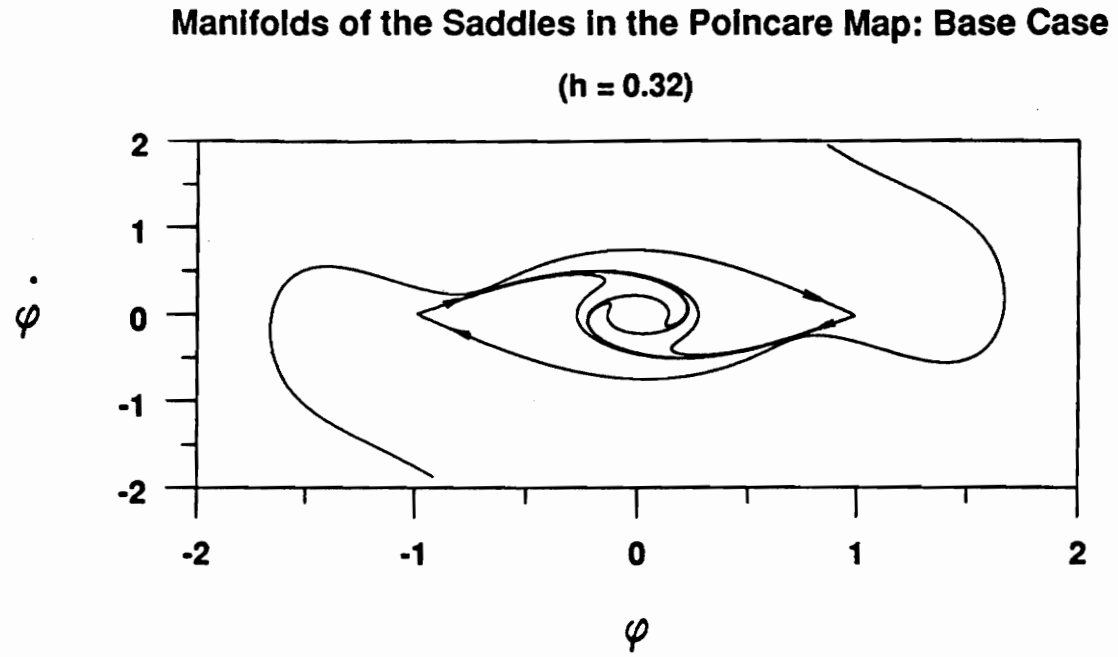

Figure 5.10. Heteroclinic Melnikov Function (h = 0.32): The curve approaches but does not reach zero for impending heteroclinic intersections.

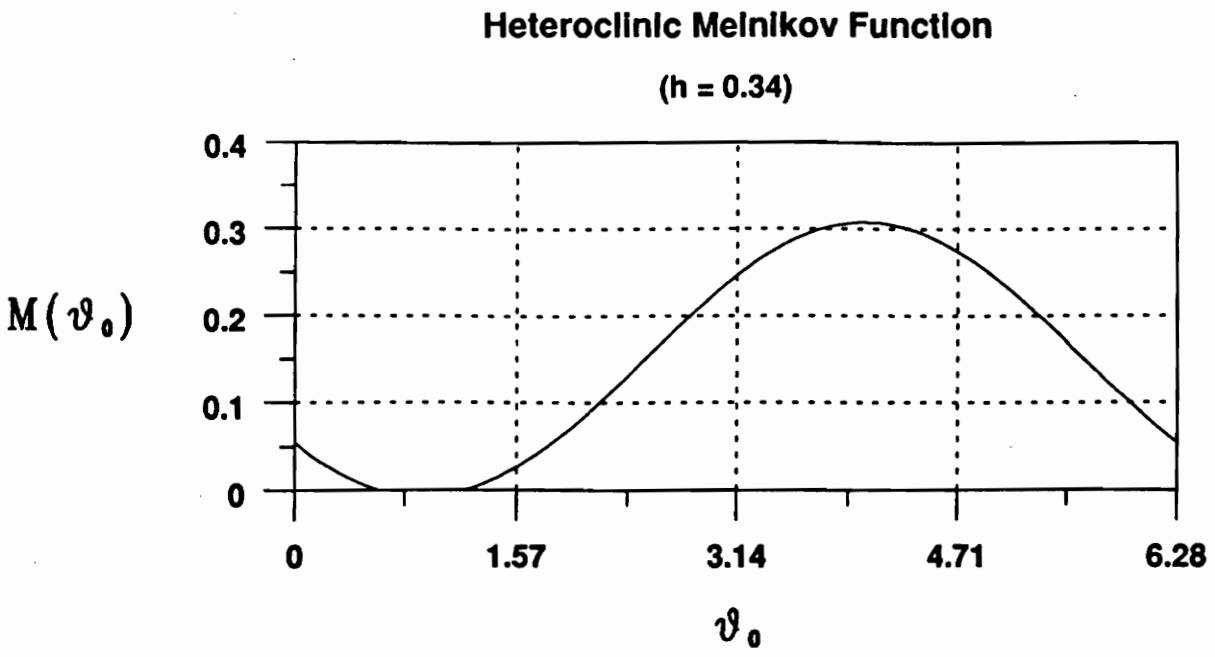

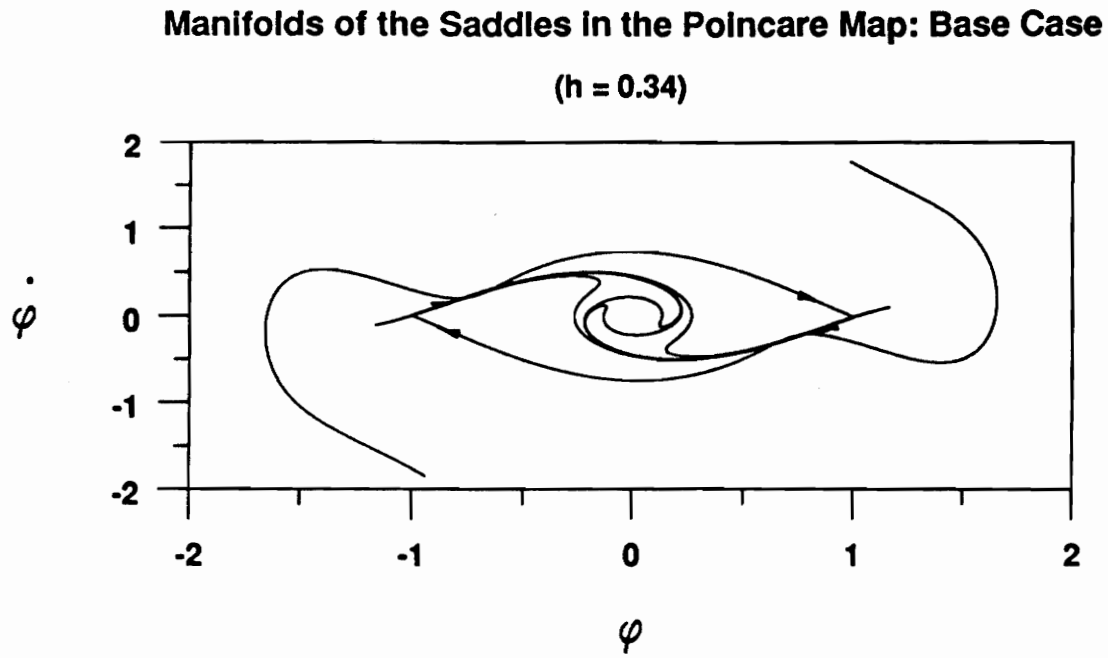

Figure 5.11. Heteroclinic Melnikov Function (h = 0.34): When heteroclinic tangles are first established, the Melnikov function exhibits a minimum near zero.

Finally, we consider the mixed intersections described in the last section. We use an apparently new technique for applying Melnikov's method in attempting to predict homoclinic-heteroclinic intersections. The results are summarized in Figures 5.12 and 5.13, which contain the Melnikov graphs and manifolds for $h = 0.21$ and $h = 0.215$. The technique seems to work quite well. As the homoclinic unstable manifold and heteroclinic stable manifold approach one another ($h = 0.21$) and then intersect ($h = 0.215$), the Melnikov function exhibits closely spaced roots in each case. Thus, Melnikov's method is slightly conservative, predicting intersections at a marginally lower forcing amplitude (just smaller than $h = 0.21$) than that at which tangles first occur (just larger than $h = 0.21$).

Summarizing, we have verified Melnikov's method for accurately predicting all types of manifold intersections observed in the base case for the ship-roll model: homoclinic, heteroclinic, and mixed homoclinic-heteroclinic. To determine the implications of manifold intersections on stability, we next examine the phase space in the neighborhood of the intersections.

5.1.4 Transient-Basin Analysis (Base Case)

5.1.4.1 Appearance of Fractal Geometry

The significance of the invariant-manifold intersections calculated and predicted in the last two sections rests on the characteristics of the evolving trajectories associated with different initial conditions in the phase space. Recall from Section 3.2 that the transient basins in phase space become fractal in nature near manifold intersections. The stability of an arbitrary initial condition in such a fractal region is virtually impossible to forecast. Due to the inherent danger of operating a ship in these areas of the phase space, we seek to identify the extent of any fractal regions for the base case and the consequent effects on stability.

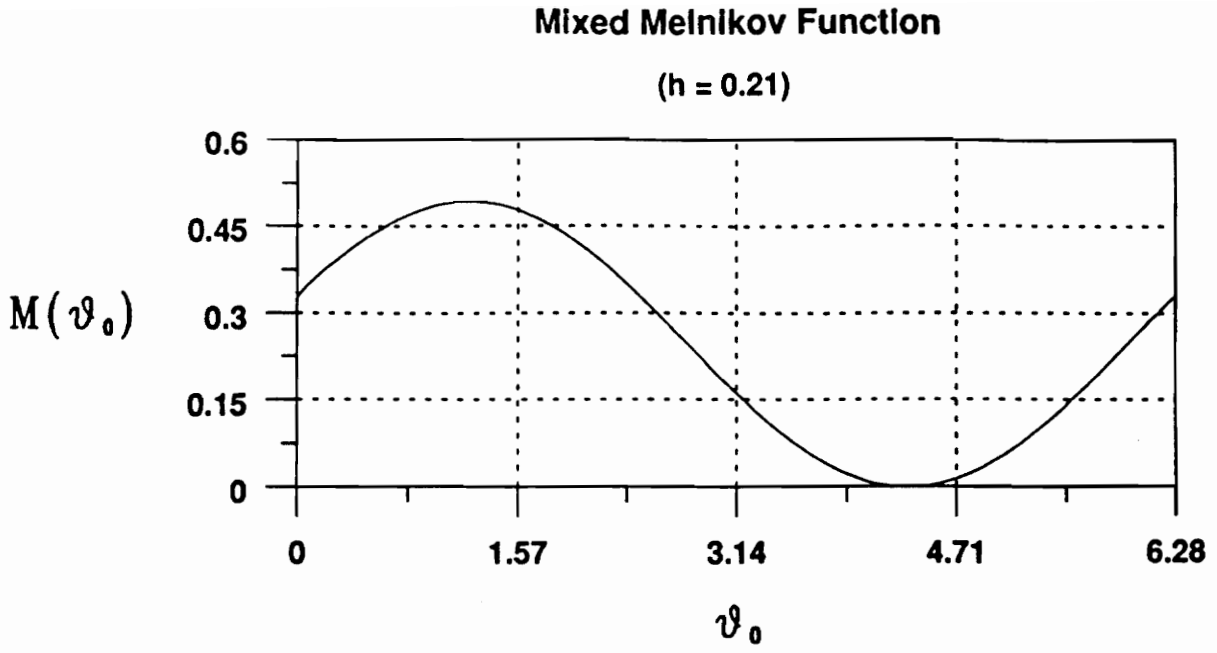

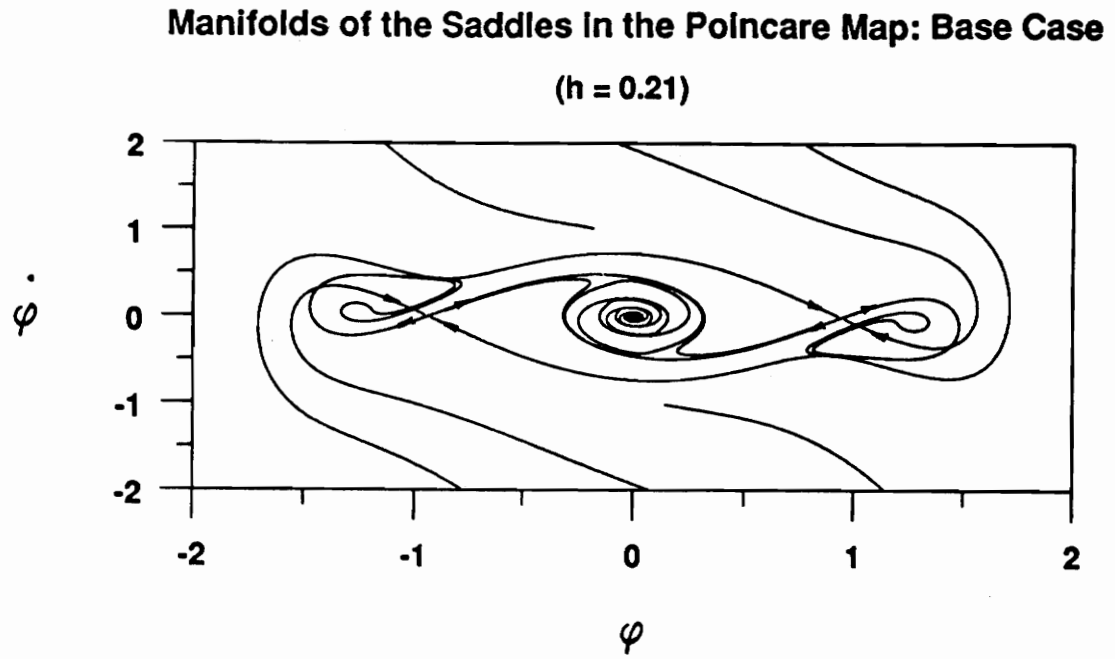

Figure 5.12. Mixed Melnikov Function (h = 0.21): For approaching intersections of a stable heteroclinic manifold and an unstable homoclinic manifold, the Melnikov function has already acquired two closely spaced roots.

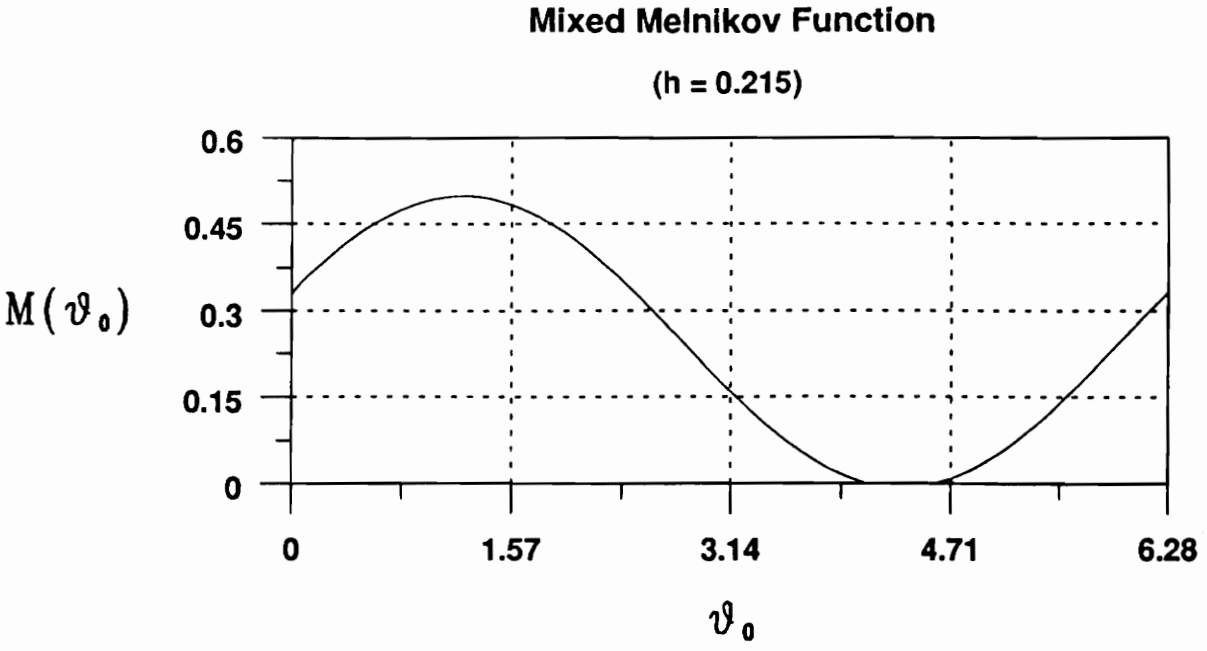

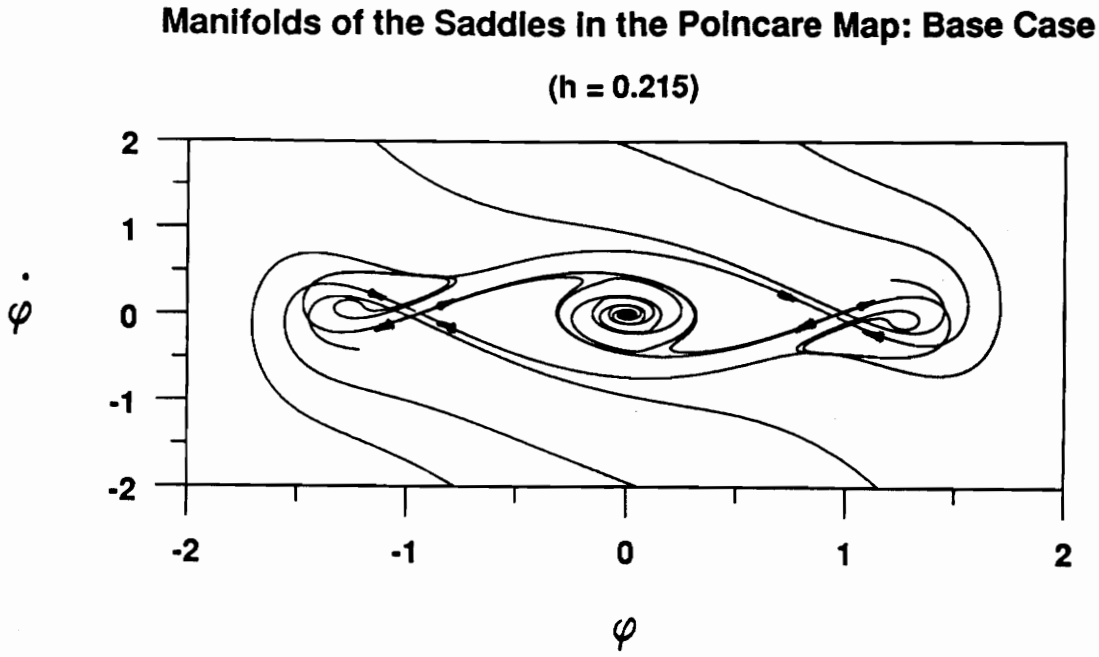

Figure 5.13. Mixed Melnikov Function (h = 0.215): As mixed tangles develop, the minimum of the Melnikov function decreases slightly. The prediction in this case is slightly conservative.

Before we examine any results, a few points concerning transient basins should be clarified. A typical graphical representation of a transient basin usually has black and white regions. One color represents initial conditions that are "stable" and the other color indicates "unstable" initial conditions. In this context, a stable initial condition must remain bounded by a specified condition after it is integrated for a specified length of time. The boundedness condition and the time of integration are parameters that may *significantly* affect the appearance of the transient basin.

With the previous remarks in mind, we first specify the time of integration for each initial condition. Although many researchers select a very large time in order to draw conclusions about the stability of their systems in the long term, such a choice makes little sense when studying the ship-roll model described by Equation [2.19]. The periodic forcing term in the equation may be associated with a regular occurrence of waves impacting the ship. The chance of a ship encountering a very long string of these identical waves is extremely small. As a result, it is more realistic to consider a small number of waves; in all of the diagrams in this section, the length of numerical integration is 25 seconds, or roughly four periods of the excitation (four waves).

The boundedness condition we apply varies with the type of manifold intersections considered, but in all cases a 400 x 400 grid of equally spaced points is integrated for the specified four periods. For each of the three types of manifold intersection (homoclinic, heteroclinic, and mixed), a rectangular region of the phase space is identified. Any grid point which leaves the region during the four periods of integration is defined as unstable and marked with a black dot. All other grid points are considered stable and remain white. For the homoclinic case, the selected region encompasses roll velocities with an absolute value of 0.75 or less and roll displacements between -2 and -0.5. This region is not unique, but represents an arbitrary area enclosing the homoclinic intersections identified earlier in this chapter. For both the heteroclinic and mixed cases, the bounds for stable behavior are defined by magnitudes of roll and roll velocity equal to 1. This choice is motivated by practical ship-stability considerations, which dictate that the roll displacement and velocity should not grow too large if capsize is to be avoided.

Homoclinic Tangles: Although the homoclinic case is irrelevant to the ship problem, we treat it as an example. Two excitation amplitudes are considered: $h = 0.07$ and h = 0.09. The lower amplitude generates no homoclinic intersections while the higher one is large enough to produce tangles. The resulting transient basins appear in Figures 5.14 and 5.15. Note that the lower amplitude results in a diagram with sharp edges between stable and unstable areas. No erosion of the safe area appears to have begun. However, the higher amplitude yields transient basins clearly marked by fractal bands, which reduce the size of the safe region. These observations confirm the implications of the homoclinic manifold intersections catalogued in the last section.

Heteroclinic Tangles: Because most ships are not likely to operate in the homoclinic region (due to the large roll displacements), we devote most of our attention to the heteroclinic case. We study a range of values for excitation amplitude h in an attempt to determine the significance of heteroclinic intersections. A value of $h = 0.25$, well below the critical value that first causes manifold intersections, resulted in the diagram apprearing in Figure 5.16; the division between stable and unstable areas is continuous. When the excitation is increased to $h = 0.32$, still below the critical value, the appearance of the transient basin is qualitatively similar (Figure 5.17) although the safe region is slightly smaller. For $h = 0.35$, which we determined produces heteroclinic intersections, the transient basin (pictured in Figure 5.18) is marked by the appearance of fractal bands surrounding the safe region. This sequence of diagrams verifies the implications of the invariant-manifold and Melnikov analyses carried out earlier in this chapter.

To examine how the fractal bands evolve, we let h increase even further. When the excitation level reaches 0.50, the transient basin has the appearance illustrated in Figure 5.19. Note that the fractal bands evident when $h = 0.35$ have seemingly disappeared (or have become negligible in size). Although the safe region is smaller and has a different shape, the division between stable and unstable areas is ostensibly continuous or very nearly so. At a much higher amplitude ($h = 2.00$), the fractal bands reappear, but again are very small; this case is shown in Figure 5.20. The excitation in this instance is so large that the safe area is essentially gone. In summary, for the base

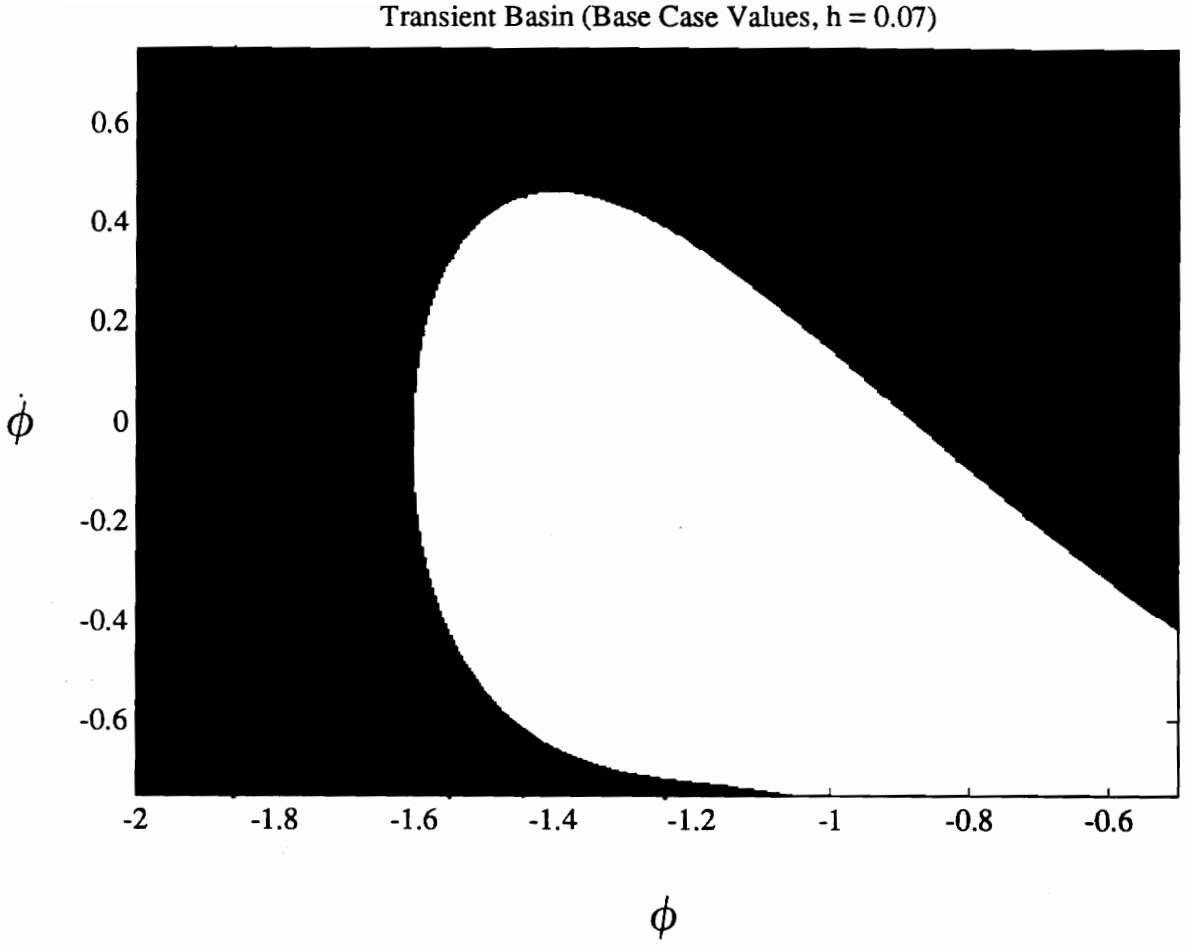

Figure 5.14. Homoclinic Transient Basin (Base Case, h = 0.07): At this low forcing amplitude, the transient basin exhibits continuous boundaries between stable and unstable regions in the phase space.

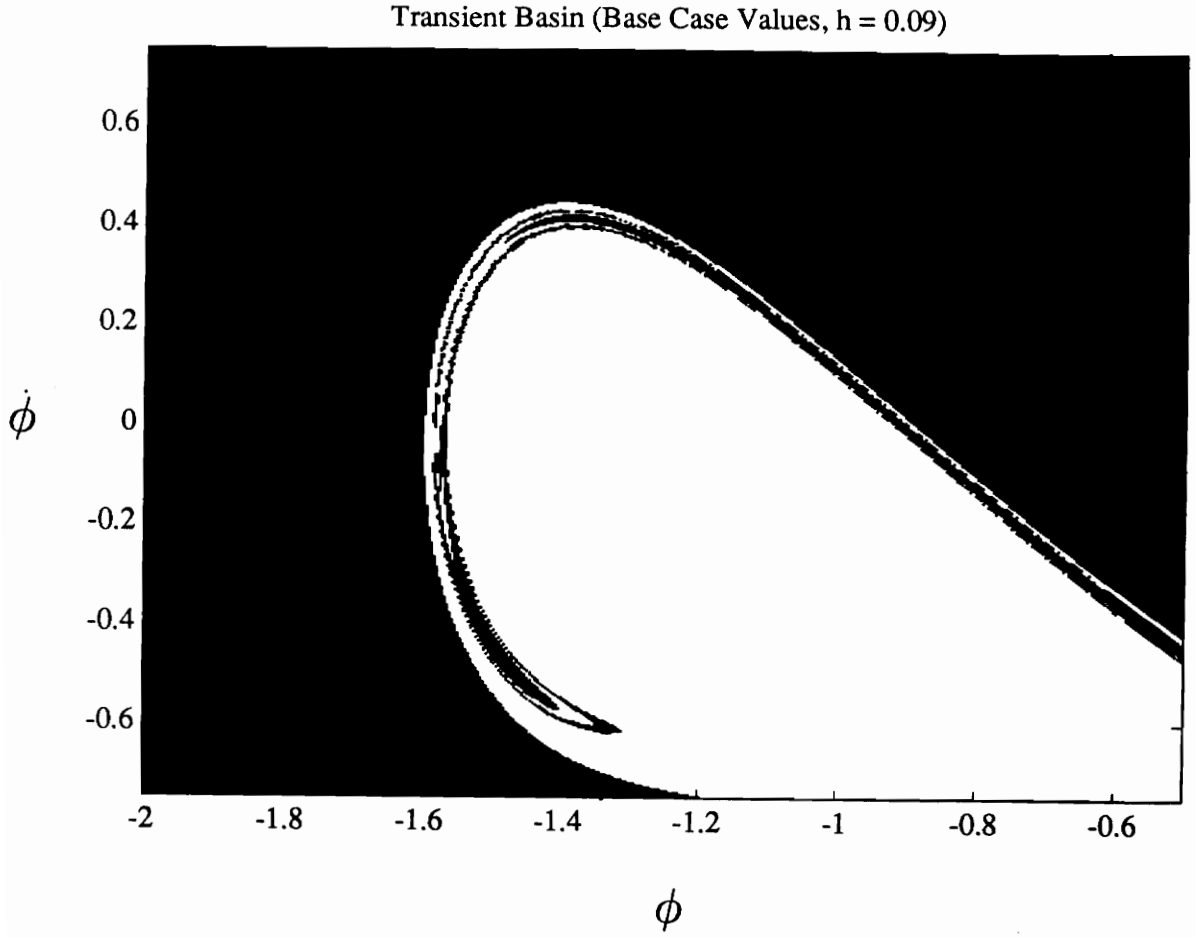

Figure 5.15. Homoclinic Transient Basin (Base Case, h = 0.09): When homoclinic intersections begin to occur, the corresponding transient basin features a fractal border between safe and unsafe areas.

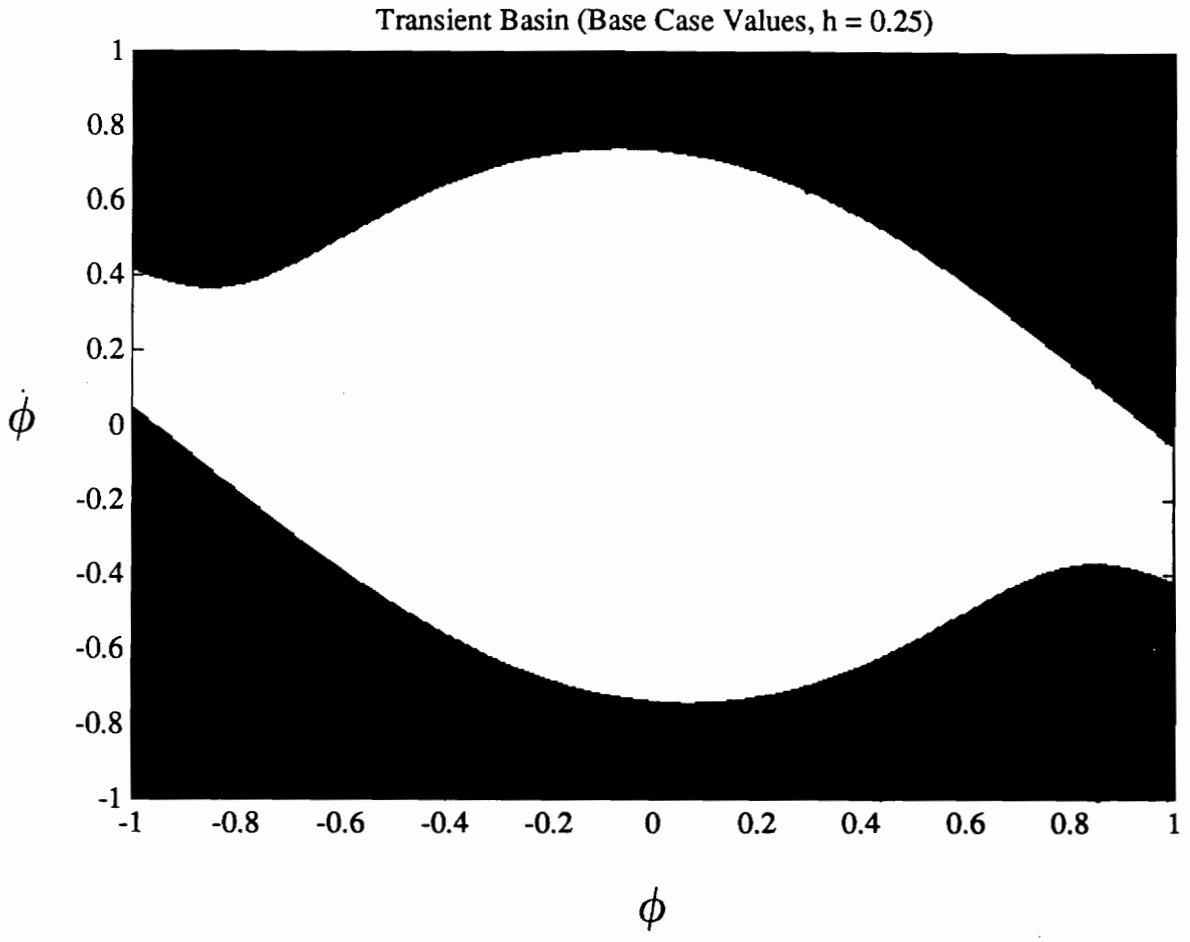

Figure 5.16. Heteroclinic Transient Basin (Base Case, h = 0.25): Before heteroclinic tangles emerge, the safe region is sharply divided from unstable initial conditions.

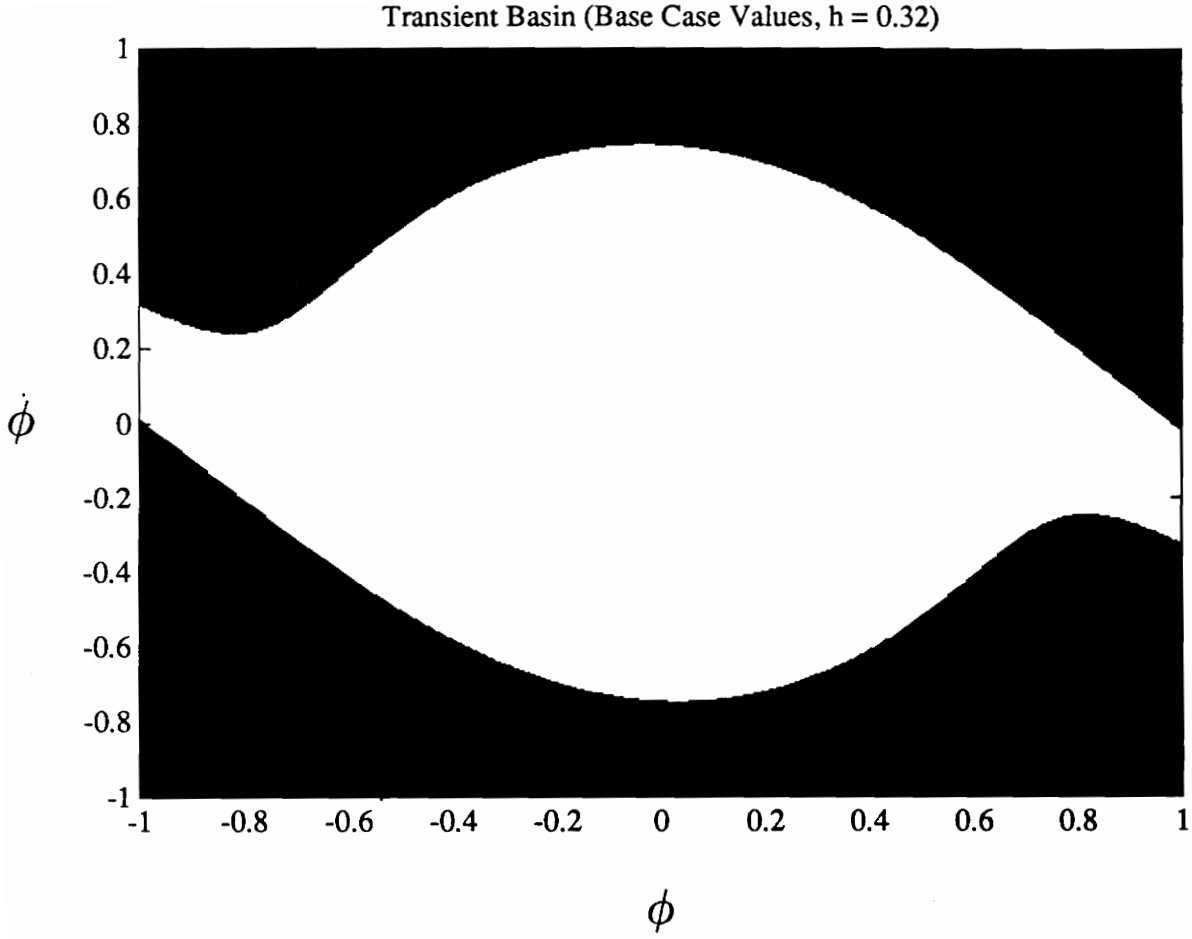

Figure 5.17. **Heteroclinic Transient Basin (Base Case, h = 0.32):** As the forcing is increased (but before manifold intersections), the safe region changes shape slightly, but remains qualitatively similar to the previous diagram.

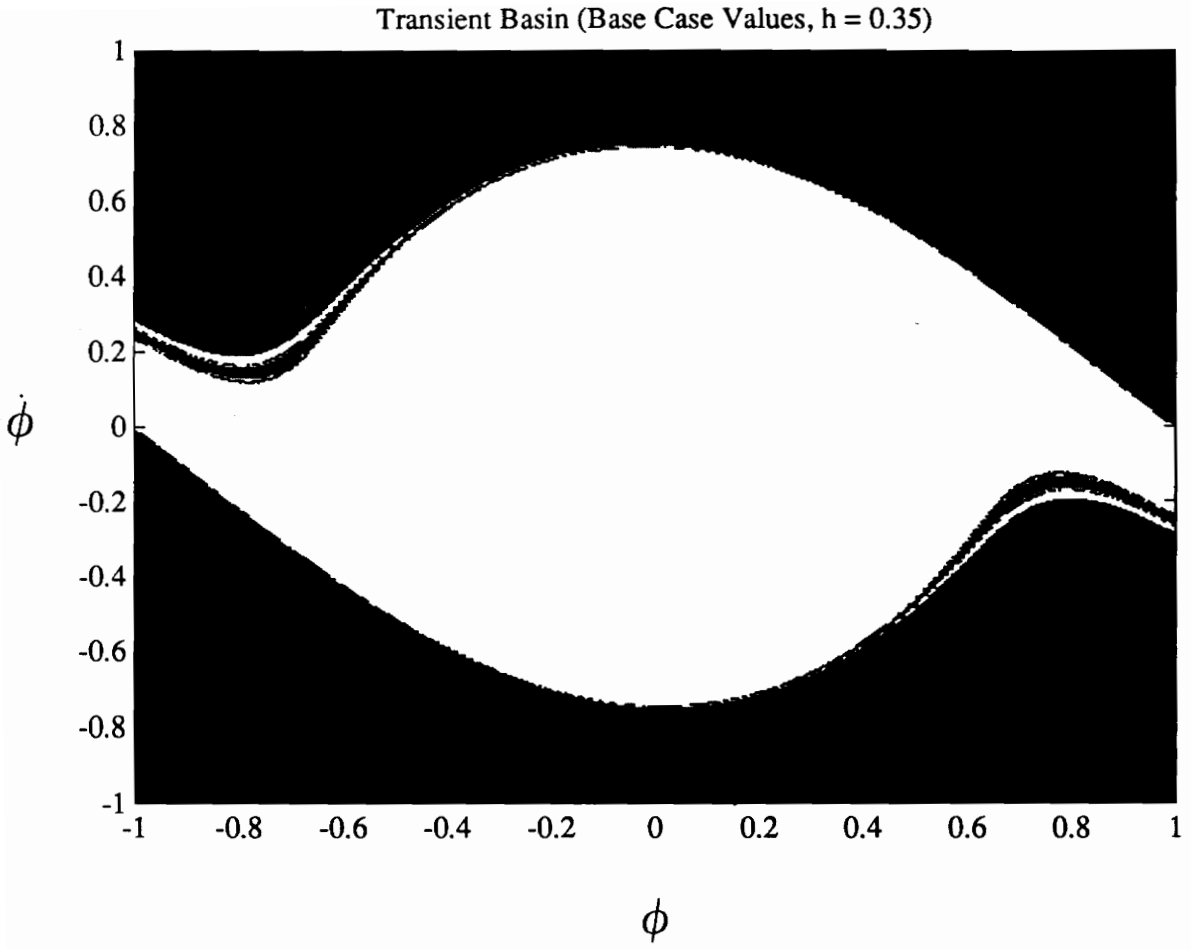

Figure 5.18. Heteroclinic Transient Basin (Base Case, h = 0.35): When manifold crossings appear, the transient basin begins to acquire fractal boundaries.

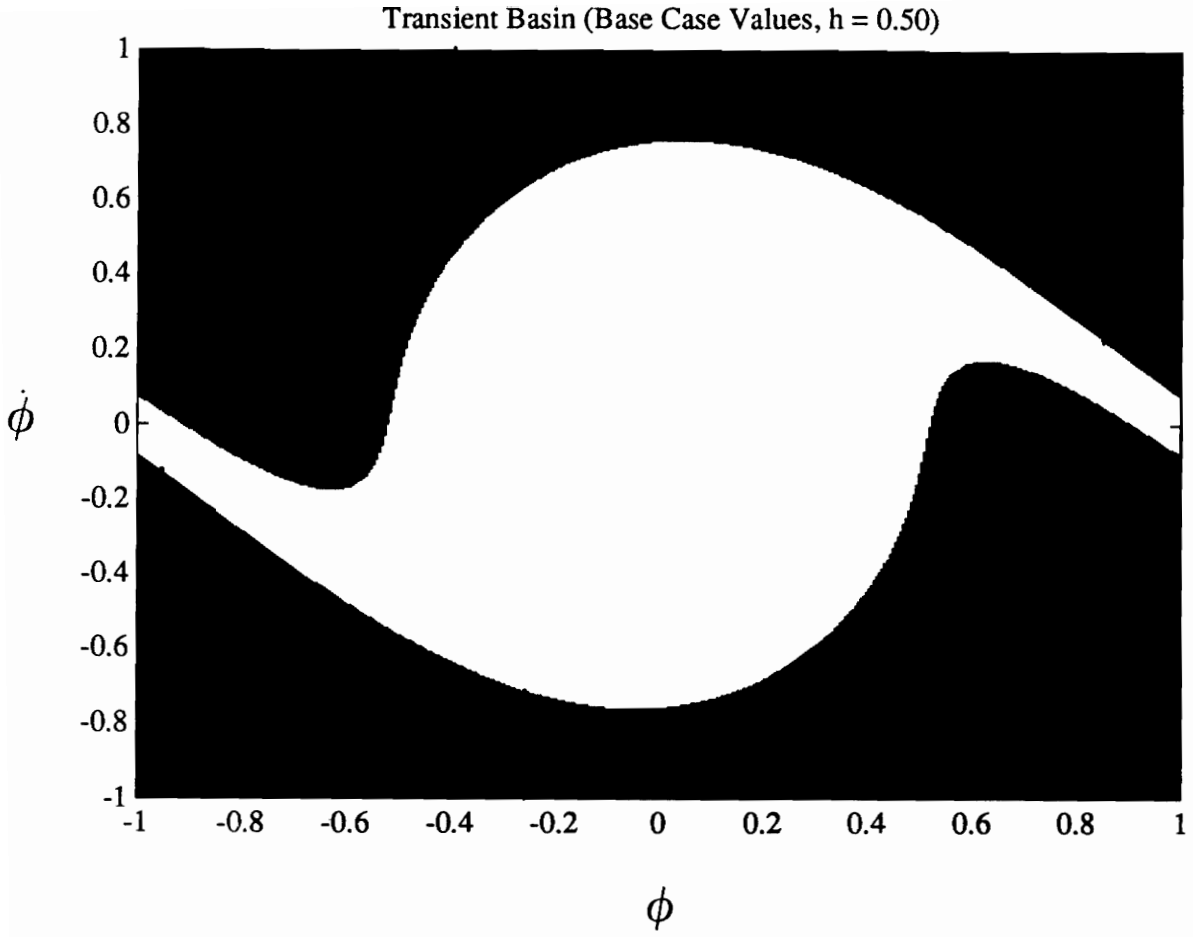

Figure 5.19. Heteroclinic Transient Basin (Base Case, h = 0.50): At a forcing amplitude well above the critical level, the fractal quality of the transient basin seems to have disappeared.

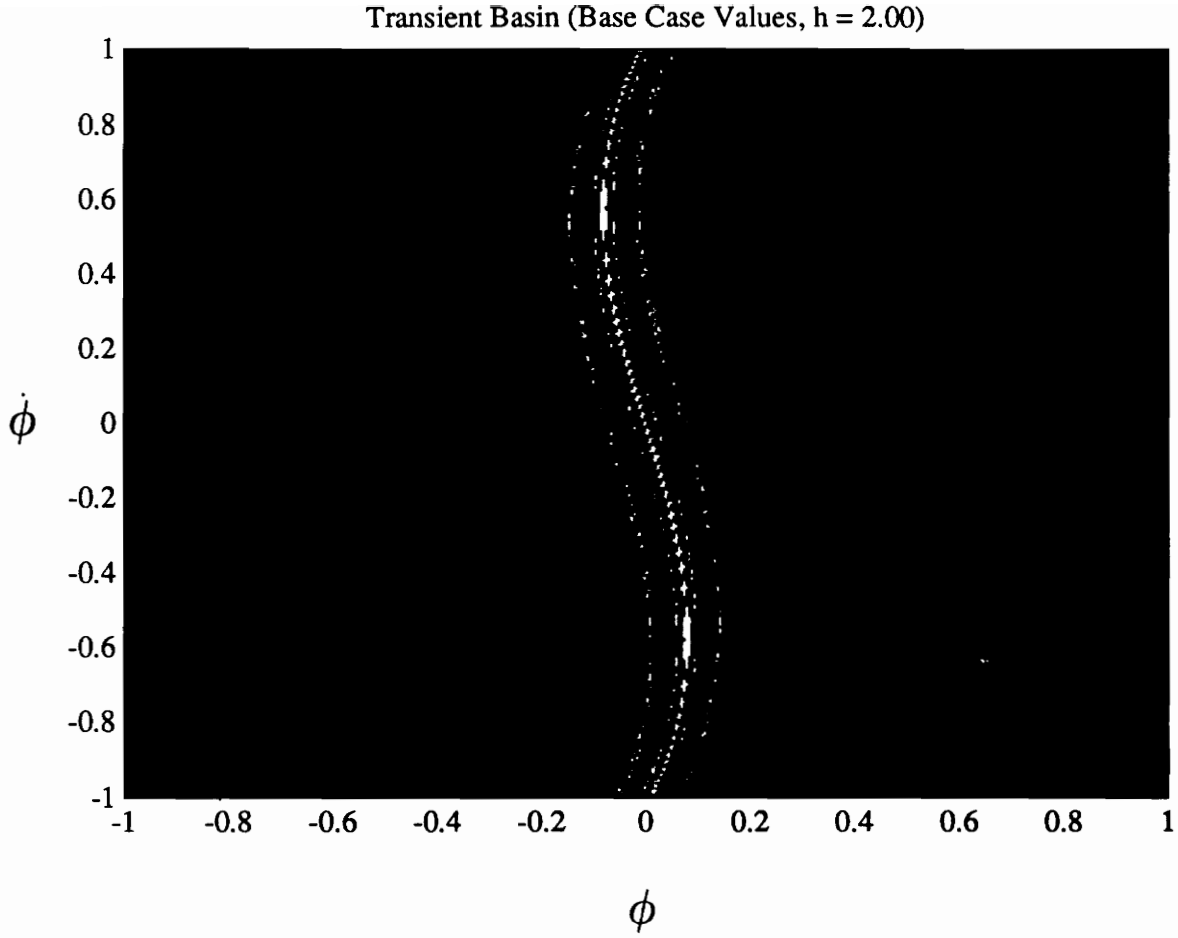

Figure 5.20. Heteroclinic Transient Basin (Base Case, h = 2.00): For very large forcing, the safe region is mostly destroyed; very small fractal areas have reappeared.

case the heteroclinic manifold intersections correctly predict the onset of fractal phase space, but these fractal areas remain small and do not significantly penetrate the safe region.

Mixed Tangles: Lastly, we consider the impact of the mixed homoclinic-heteroclinic intersections on the character of the phase space. Are there fractal regions associated with this type of intersection? For the boundedness condition defined earlier, Figure 5.16 suggests a negative answer. The excitation level for that diagram ($h = 0.25$) exceeds the amplitude of 0.215 at which mixed intersections first occurred. Yet the transient basin shows no sign of fractal geometry. This result can most easily be understood by returning again to the manifold diagram that illustrates mixed intersections (Figure 5.13). The locations of the intersections are far from the origin; we recall from Chapter 3 that manifold intersections induce fractal behavior to occur in the transient basin in the neighborhood of the intersections. Thus, the mixed tangles are not expected to cause fractal bands in the safe region near the origin, meaning that for the base case, the phenomenon termed "totally unexpected capsize" by Falzarano [1990] is unlikely to occur.

A feature common to all of the transient basins in this section is symmetry about the origin. Recall that the corresponding invariant manifolds also had this property, which we attributed to the odd symmetry of Equation [2.19]. Apparently, the odd symmetry of [2.19] also causes the symmetry observed in the transient basin. This phenomenon implies significant computational savings because only one half of any diagram needs to be computed.

5.1.4.2 Stability Implications for Ship Roll

The transient basins in the previous section reveal that stable and unstable regions of phase space become fractally mixed for two of the three types of manifold intersection studied: homoclinic and heteroclinic, but not mixed. The homoclinic case is, as mentioned earlier, not very useful for predicting ship capsize. Mixed tangles for base-case parameter values may be ignored, as they have no apparent effect on ship stability.

Heteroclinic tangles, on the other hand, did result in the onset of fractally mixed stable and unstable areas of the phase space in a neighborhood potentially crucial to ship stability. The relevant transient basins exhibited fractal bands in which predicting stability (as defined for the transient basins) becomes impossible. The size of the fractal region, however, is small or even negligible (Figures 5.16-5.20). Consequently, a ship with the characteristics denoted by the base case can operate safely (for four periods) in a sharply defined region for excitation amplitudes considerably larger than the critical value at which heteroclinic crossings begin to occur. This value is thus probably suitable as an upper bound on acceptable parametric excitation as defined in our model.

The essential integrity of the safe region for large amplitudes contrasts with other studies that focus on external forcing. Thompson [1991] examined a single-degree-of-freedom equation with a quadratic nonlinearity and external excitation; he noted an abrupt erosion of the stable area in the transient basin as the forcing amplitude is increased above the critical value. We have not observed this phenomenon for parametric excitation. However, Thompson's model and Equation [2.19] have other differences besides the form of the excitation.

In order to test if the type of forcing is the cause of the catastrophic erosion that Thompson noticed, we consider the base case with external excitation substituted in place of the parametric term. Melnikov's criterion was used to predict heteroclinic intersections. The prediction is confirmed by the manifolds themselves, which appear in Figure 5.21 and indicate that the critical value of h is slightly less than 0.23. The corresponding transient basin is shown in Figure 5.22. It contains fractal boundaries, but the safe region has not been significantly penetrated. However, when the amplitude is raised to 0.30 (Figure 5.23), one fractal region extends almost to the origin, seriously threatening safe ship operation. At $h = 0.40$ (Figure 5.24), the integrity of the safe region is completely destroyed. Apparently, the use of external excitation in Equation [2.19] is necessary to produce the rapid decline of stable area in the transient basin seen in Thompson's model. Also, further evidence for the correlation between the odd symmetry of the parametrically forced equation and symmetric transient basins is the *asymmetry* of the basins associated with the externally forced equation, which is *not* odd.

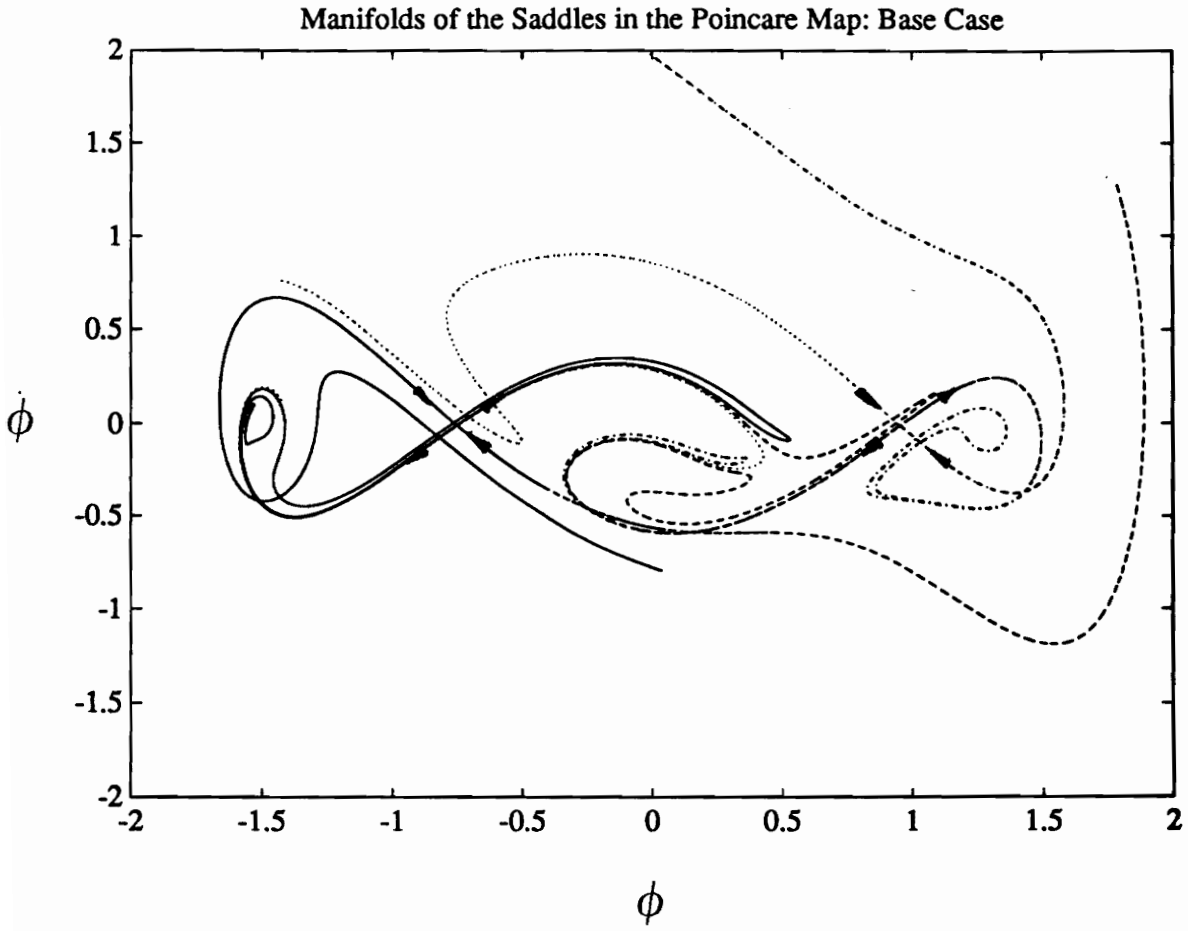

Figure 5.21. Manifolds for External Forcing (Base Case, h = 0.23): The manifolds for the externally forced roll equation are shown as heteroclinic crossings have just been established.

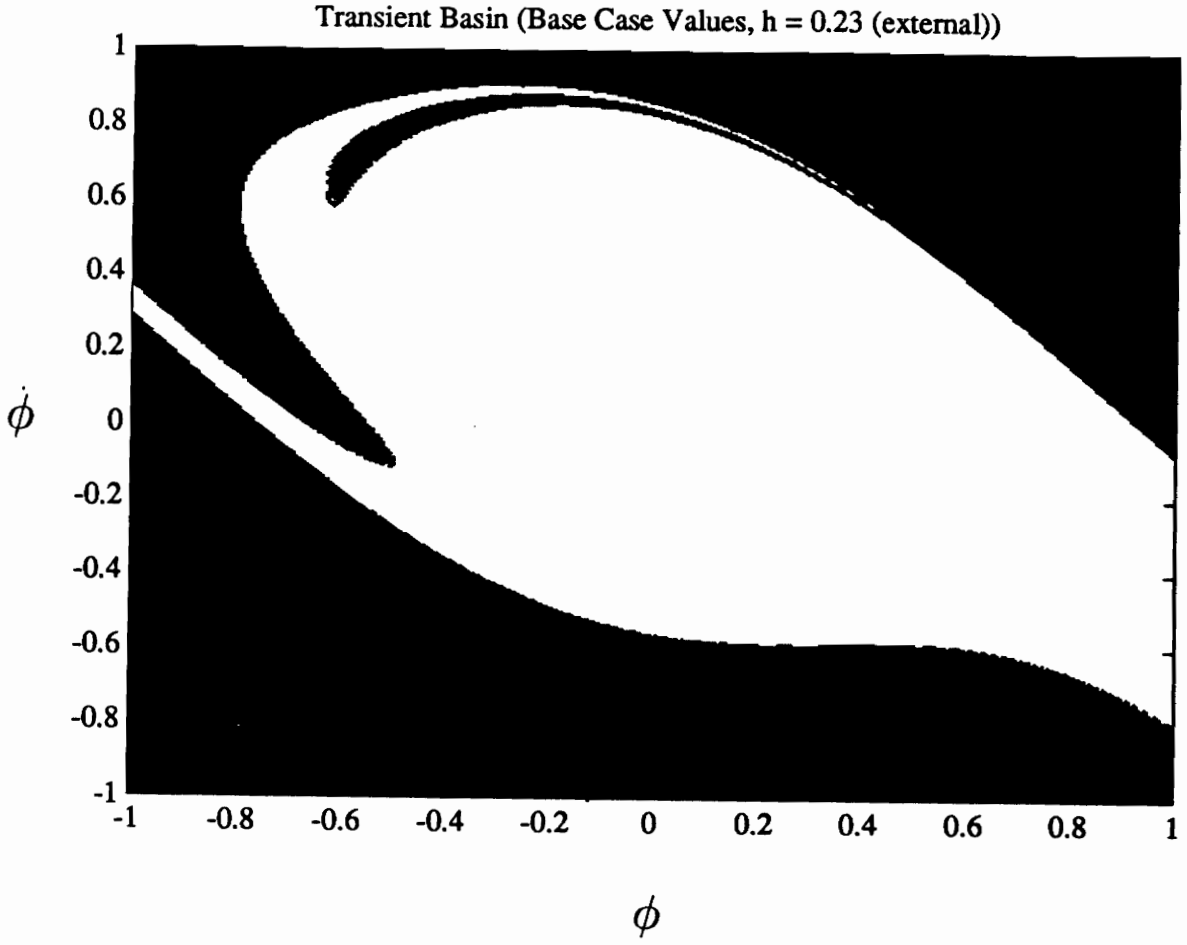

Figure 5.22. Transient Basin for External Forcing (Base Case, h = 0.23): The companion basins for the externally forced model exhibit fractal behavior.

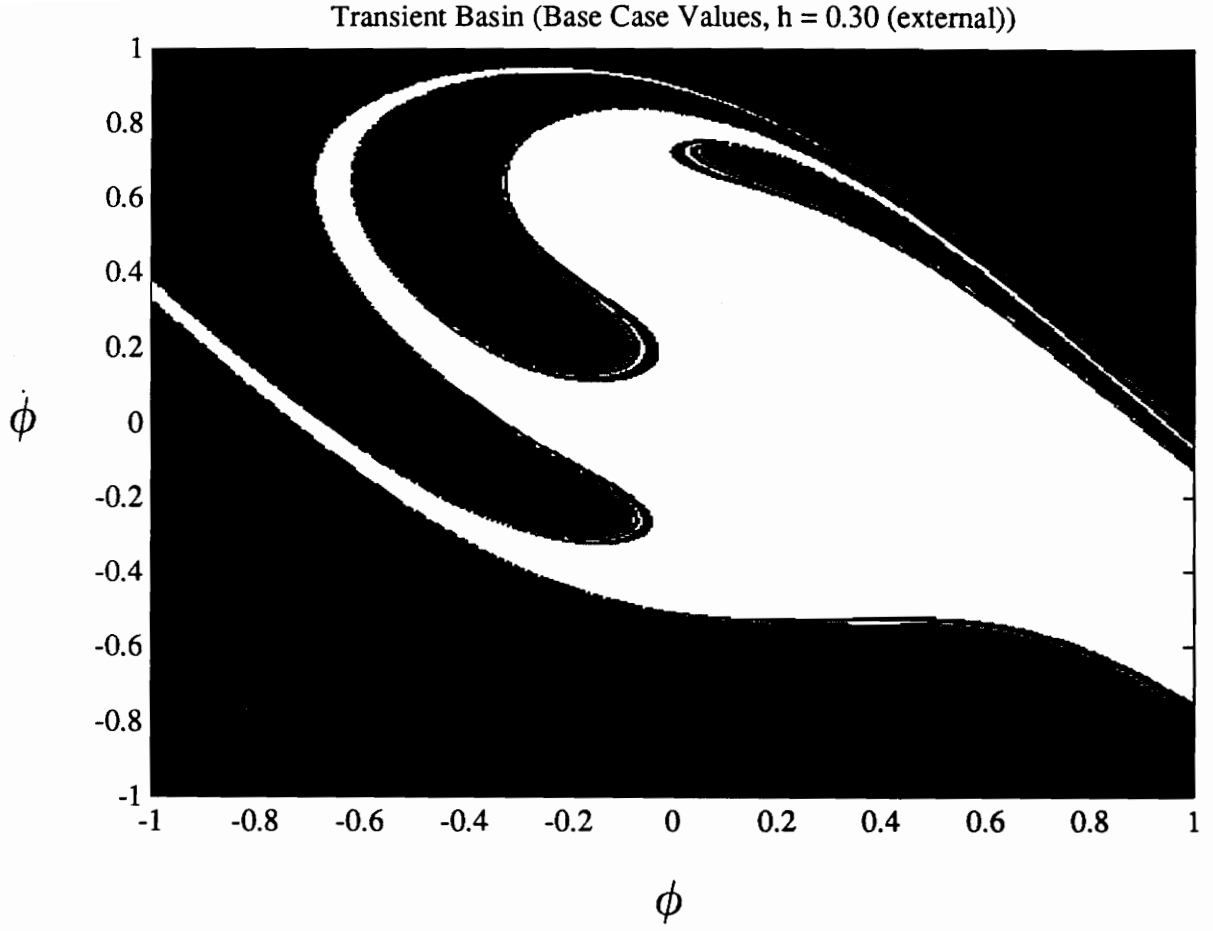

Figure 5.23. Transient Basin for External Forcing (Base Case, h = 0.30): As the forcing is increased, the external model shows an abrupt, catastrophic penetration of the safe region by fractal structures.

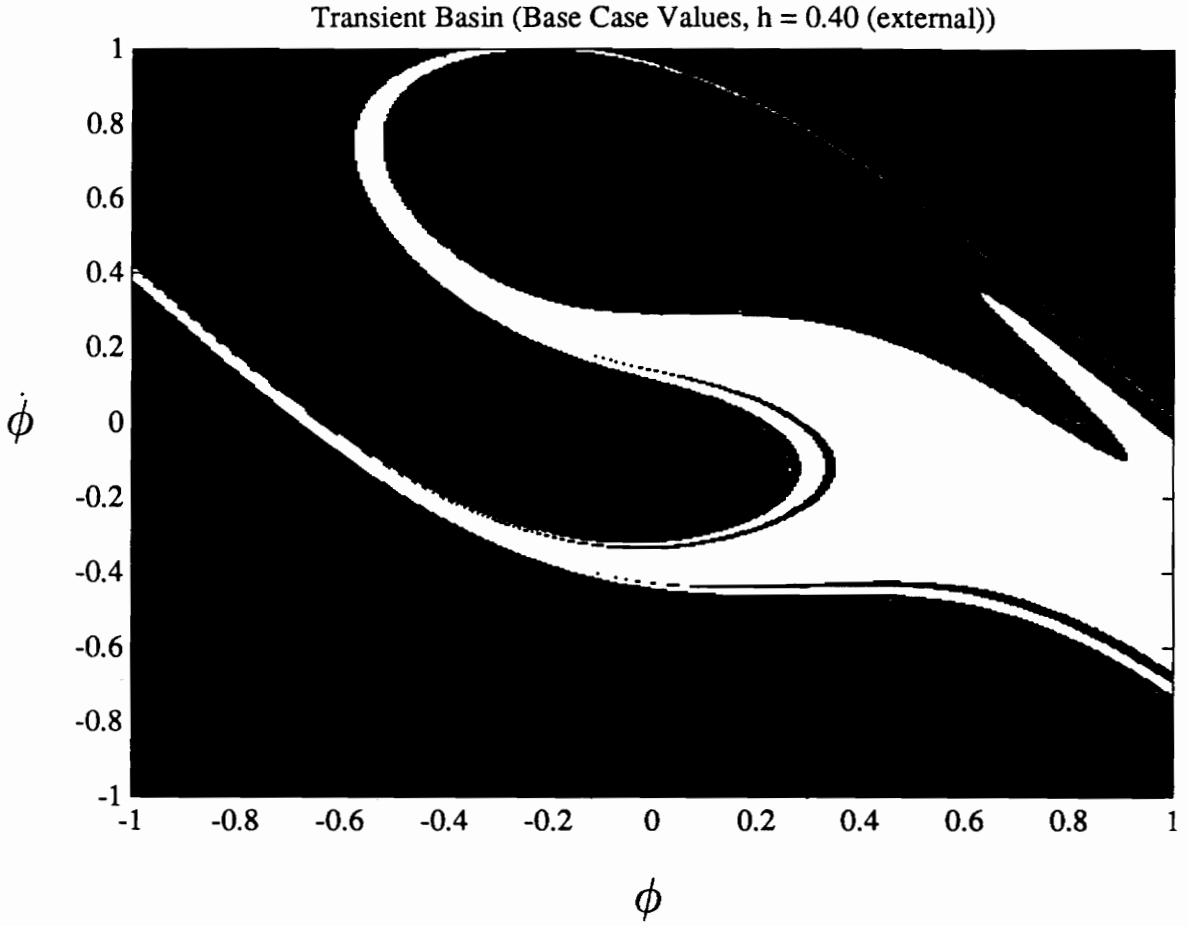

Figure 5.24. Transient Basin for External Forcing (Base Case, h = 0.40): At an even higher forcing level, the safe basin is completely destroyed.

We lastly consider the presence of both types of excitation to see if the decrease in stable area is accelerated. Physically, such a situation could occur in a beam sea (Blocki [1980]). We treat only a single example: a parametric amplitude of 0.25 and an external amplitude of 0.20. Both of these values are smaller than the respective critical h values determined earlier when only a single forcing term was examined. The resulting transient basin in Figure 5.25 exhibits a large fractal area near the origin. Solely from this example, we conclude that combined external-plus-parametric forcing is a potentially problematic situation deserving further attention.

5.2 *Parameter Study*

Having established the viability of Melnikov's method as a predictor of transverse manifold intersections for the single-degree-of-freedom ship-roll model, we employ the method in examining the effects of varying the characterstic parameters of the system. Beforehand, it should be noted that we verified Melnikov's method for the *base case*, which comprises specific values of the restoring-moment and damping coefficients. We have yet to justify the use of Melnikov's method for the various combinations of parameter values considered in the following analysis. For clarity, the evidence that Melnikov's method correctly predicts manifold intersections for these other cases is deferred until Section 5.2.4.

Each of the four parameters of interest (α_3, α_5, μ_1, and μ_3) is varied independently from its base-case value. For each new value of a parameter, the forcing amplitude at which transverse manifold intersections first occur (we term this value h_c) is computed using Melnikov's method. We obtain four curves that indicate the dependence of the critical value h_c on each of the four parameters. Note that while one particular parameter is varying, all others remain fixed at their base-case values.

After establishing these four relationships, two other combinations of parameters are considered: a "high" set and a "low" set. Each set is determined from the high and low parameter

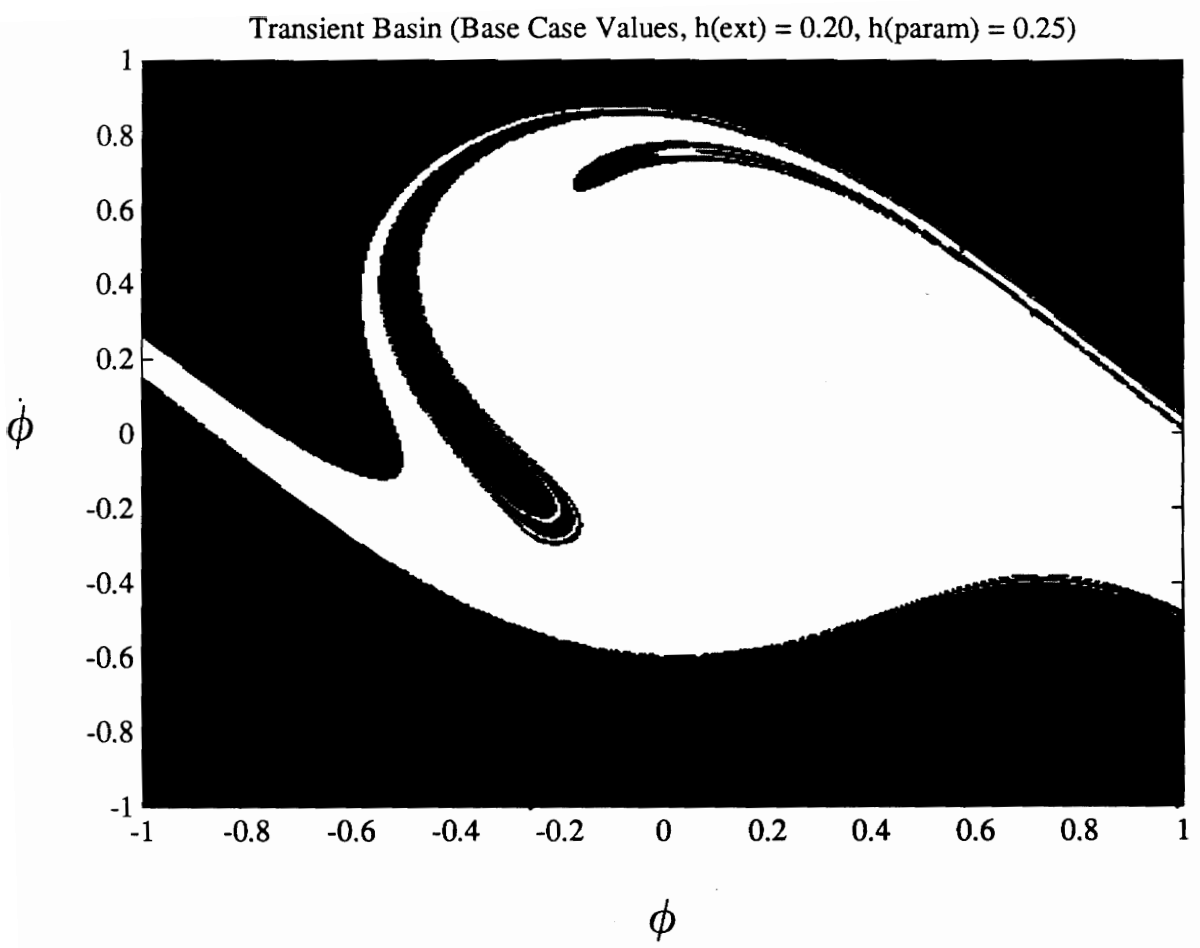

Figure 5.25. Transient Basin for Combined Forcing (Base Case, h(e) = 0.20 and h(p) = 0.25): For combined external-plus-parametric excitation, significant erosion of the safe basin occurs even when each parameter is lower than its independent critical level.

magnitudes appearing in the curves generated in the previous procedure. Then an analogous group of four curves is produced for both the high and low sets of parameter values. This analysis yields critical excitation levels for a rather large variety of parameter combinations; a similar study using invariant-manifold calculations would take a far greater amount of computational time.

5.2.1 Base-Case Values

As just described, the restoring-moment and damping coefficients are fixed at their base-case values and then varied independently to determine their effects on h_c. The results are presented graphically in the plots of Figures 5.26-5.29. As might be expected, the cubic restoring-moment coefficient (Figure 5.26) has a more significant impact on h_c than the quintic restoring-moment coefficient (Figure 5.27), yielding a wider range of critical excitation levels. In a similar way, the linear damping constant (Figure 5.28) is more influential than the cubic damping constant (Figure 5.29).

Perhaps more interesting is the nature of the relationships. The two involving damping constants are *linear*. This result is potentially useful: the value of h_c for any damping value may be quickly calculated if the other parameters are specified and two h_c values are known. The two plots involving α_3 and α_5 are not linear, but instead tend to flatten out as the independent variable decreases, apparently approaching some limiting value asymptotically. The shape of these two curves is best understood by digressing to look at the way in which α_3 and α_5 must relate. In order for our ship-roll model to exhibit two saddle points, as desired, the unperturbed equation must have five fixed points. As shown in Chapter 2, the equilibrium roll angles for the conservative system are given by

$$x_{c_1} = 0, \pm \sqrt{\frac{-\alpha_3 \pm \sqrt{{\alpha_3}^2 - 4\alpha_5{\omega_0}^2}}{2\alpha_5}} \qquad [5.6]$$

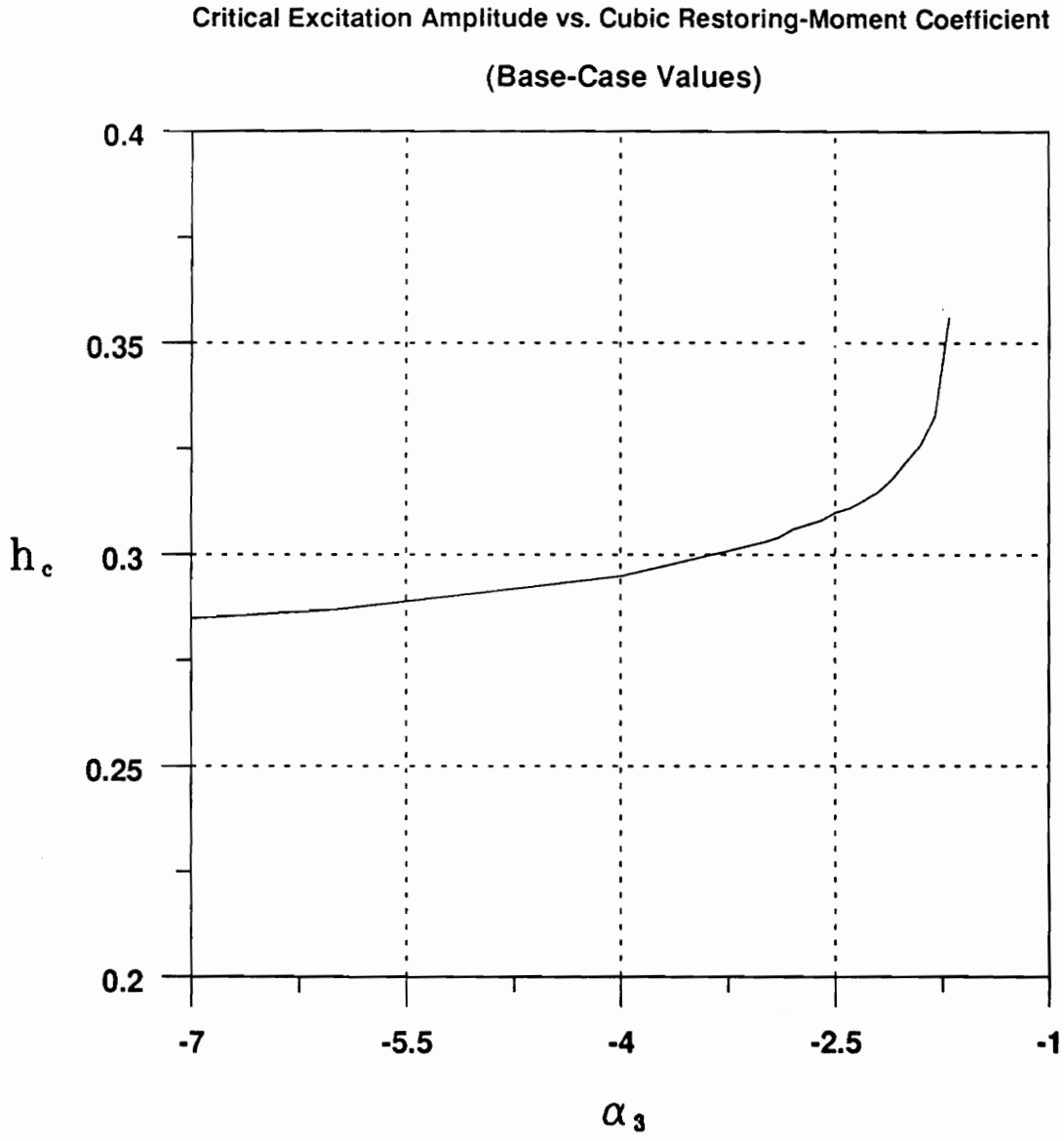

Figure 5.26. **Effect of the Cubic Restoring-Moment Coefficient (BC):** For base-case values, the critical forcing level h_c is shown as a function of the cubic restoring-moment coefficient while all other parameters are held constant.

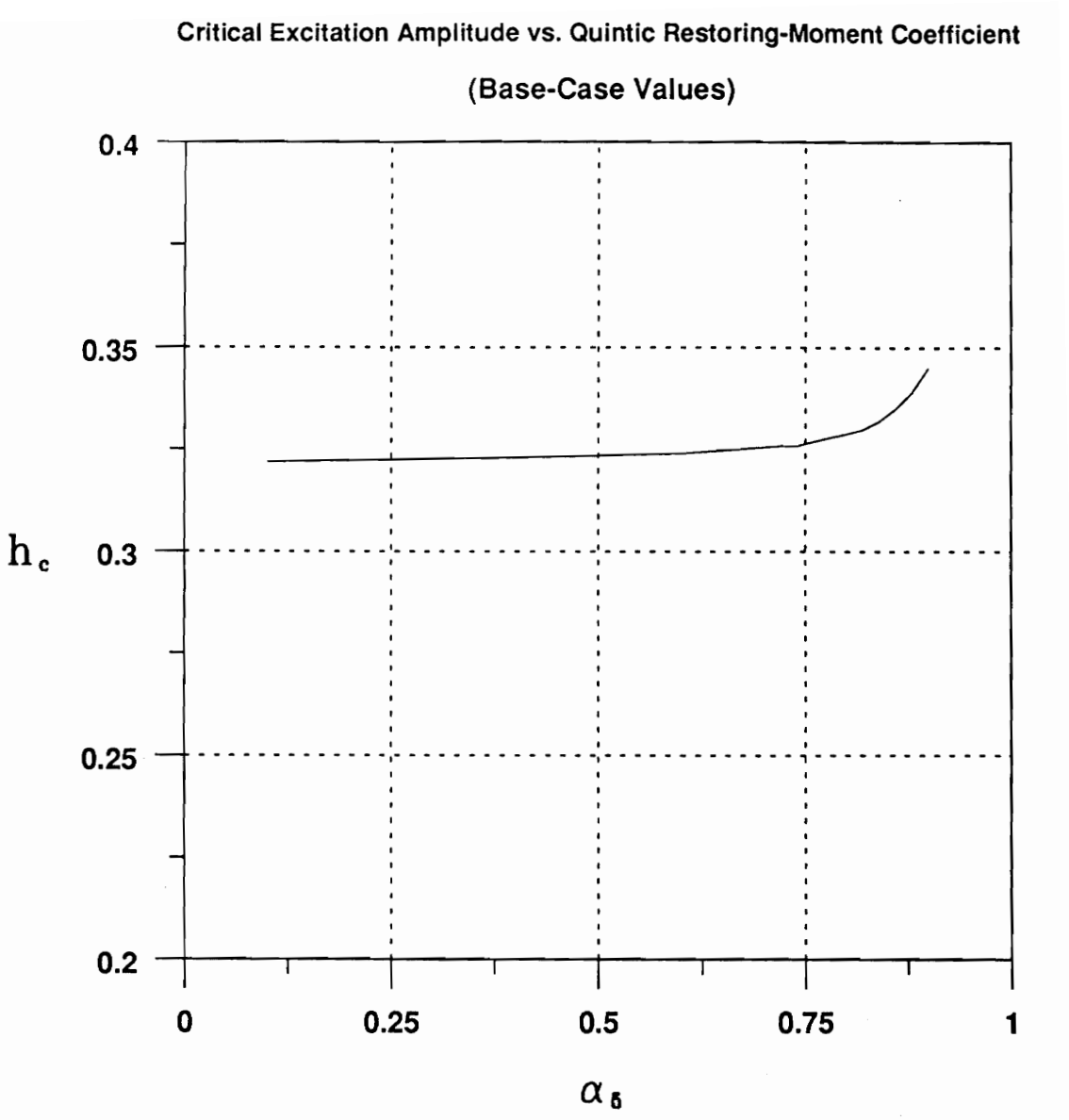

Figure 5.27. Effect of the Quintic Restoring-Moment Coefficient (BC): For base-case values, the critical forcing level h_c is shown as a function of the quintic restoring-moment coefficient while all other parameters are held constant.

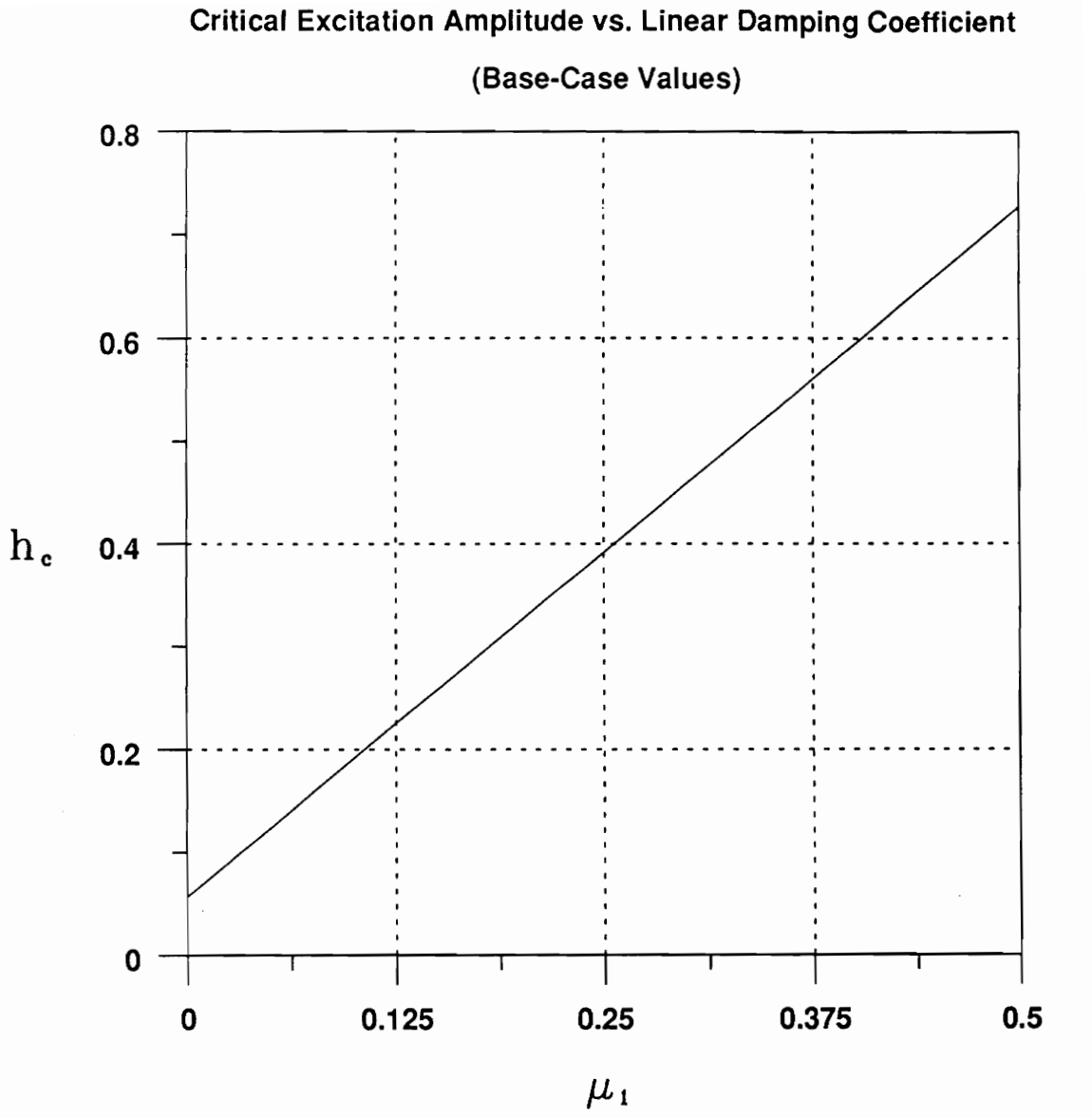

Figure 5.28. Effect of the Linear Damping Coefficient (BC): For base-case values, the critical forcing level h_c is shown as a function of the linear damping coefficient while all other parameters are held constant.

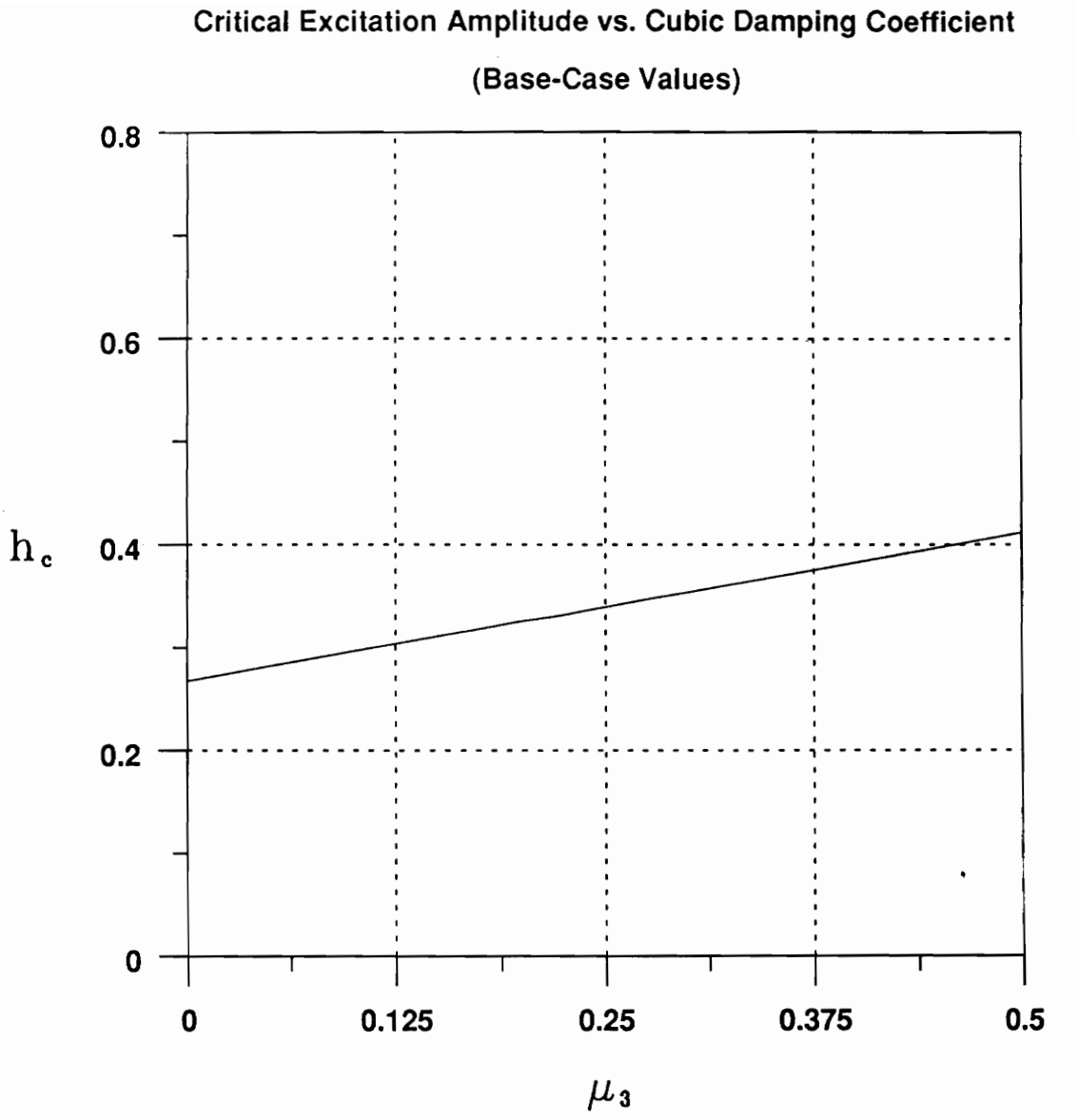

Figure 5.29. Effect of the Cubic Damping Coefficient (BC): For base-case values, the critical forcing level h_c is shown as a function of the cubic damping coefficient while all other parameters are held constant.

For five real roots to exist, α_3 must be negative, α_5 must be positive, and the following must be satisfied:

$$\alpha_3^2 \geq 4\alpha_5\omega_0^2 \qquad [5.7]$$

At this point, the graphs in Figures 5.26 and 5.27 begin to make sense. The rapid changes in slope in each figure occur when the parameter in question approaches the value that makes the expression in Equation [5.7] an equality. Thus, when each parameter is far from that crucial value, it has relatively little bearing on the critical excitation h_c.

5.2.2 Low Values

In the last section, each parameter was varied from its base-case value. Now we choose a different set of values at which each parameter is initially fixed. The values are determined by selecting low magnitudes in the graphs of Figures 5.26-5.29. Thus, both damping coefficients are set equal to 0.1, the cubic coefficient to -1.7, and the quintic coefficient to 0.1. This group of values is analogous to the base case; each parameter is in turn varied to produce plots similar to those generated in the last section.

The graphs that result appear in Figures 5.30-5.33. The most important feature of these relationships is their qualitative similarity to the curves generated from base-case values, meaning it is likely that *any* combination of fixed values will yield linear curves for the damping parameters and asymptotic curves for the restoring-moment coefficients. It is also noteworthy that the ranges of values for h_c are shifted downward in comparison to the curves of Section 5.2.1. The precise cause of this change is unclear because all four parameter values were altered. However, the lowering of both damping coefficients would be expected to have such an effect.

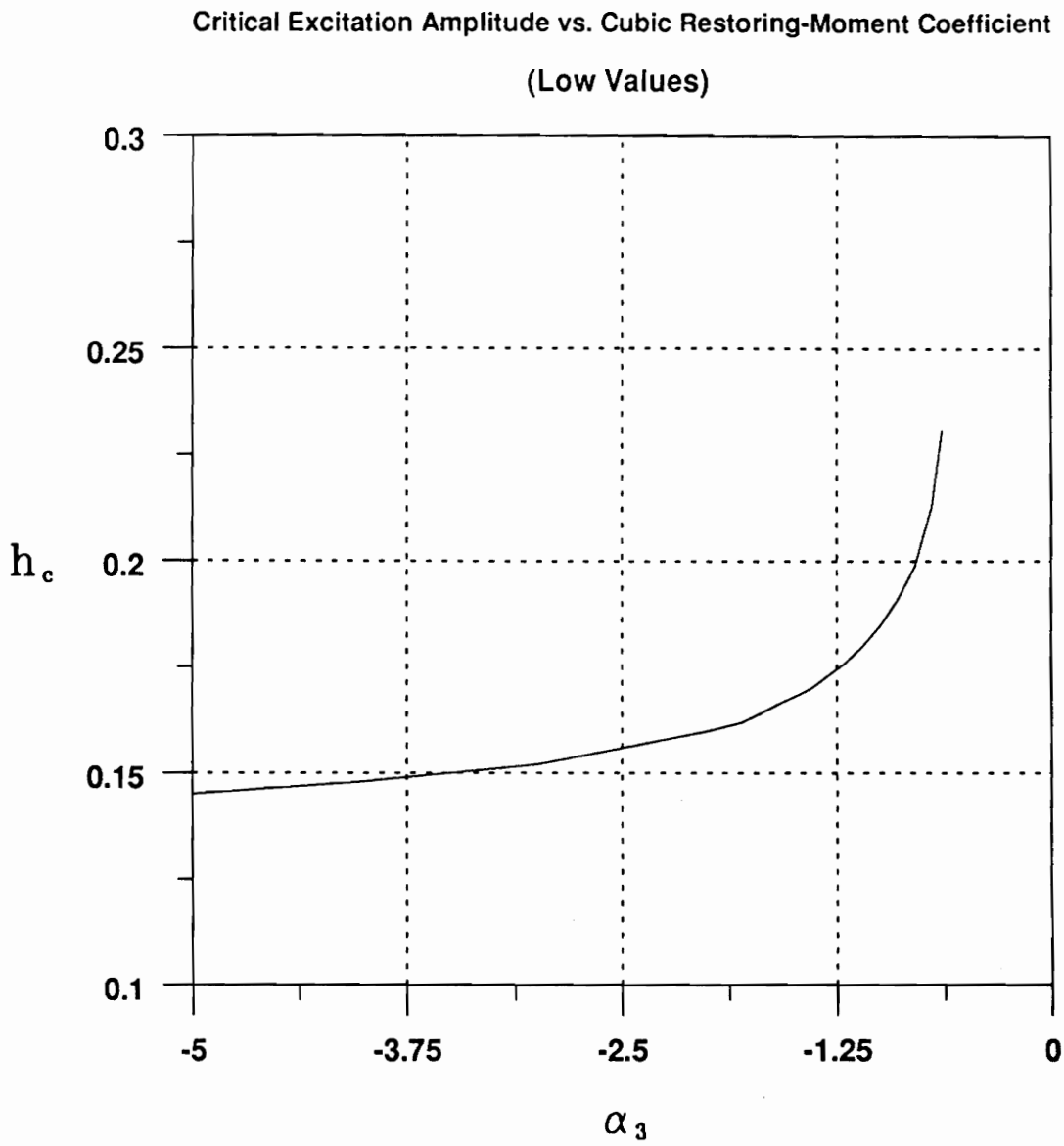

Figure 5.30. Effect of the Cubic Restoring-Moment Coefficient (LOW): For low values, the critical forcing level h_c is shown as a function of the cubic restoring-moment coefficient while all other parameters are held constant.

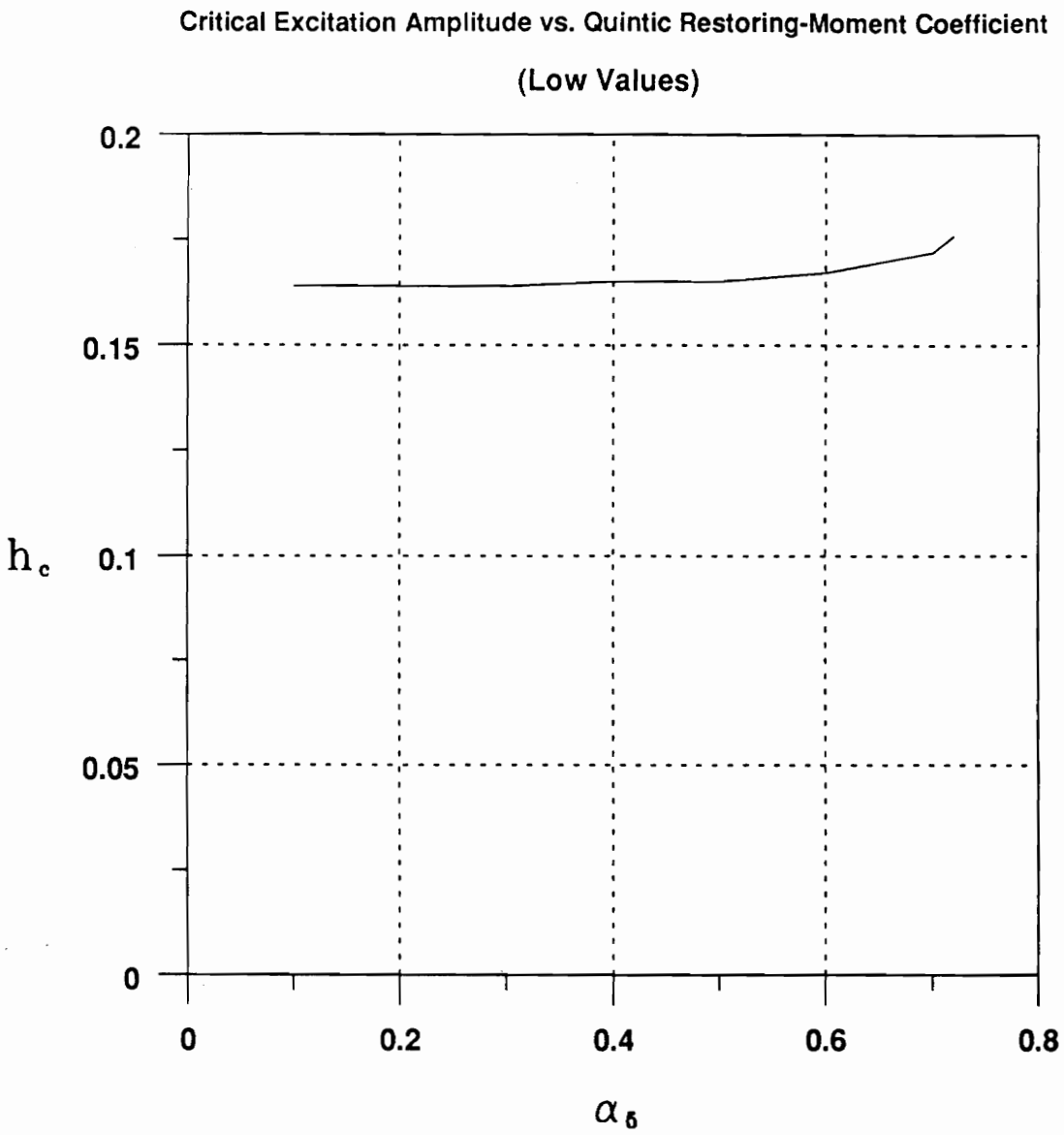

Figure 5.31. Effect of the Quintic Restoring-Moment Coefficient (LOW): For low values, the critical forcing level h_c is shown as a function of the quintic restoring-moment coefficient while all other parameters are held constant.

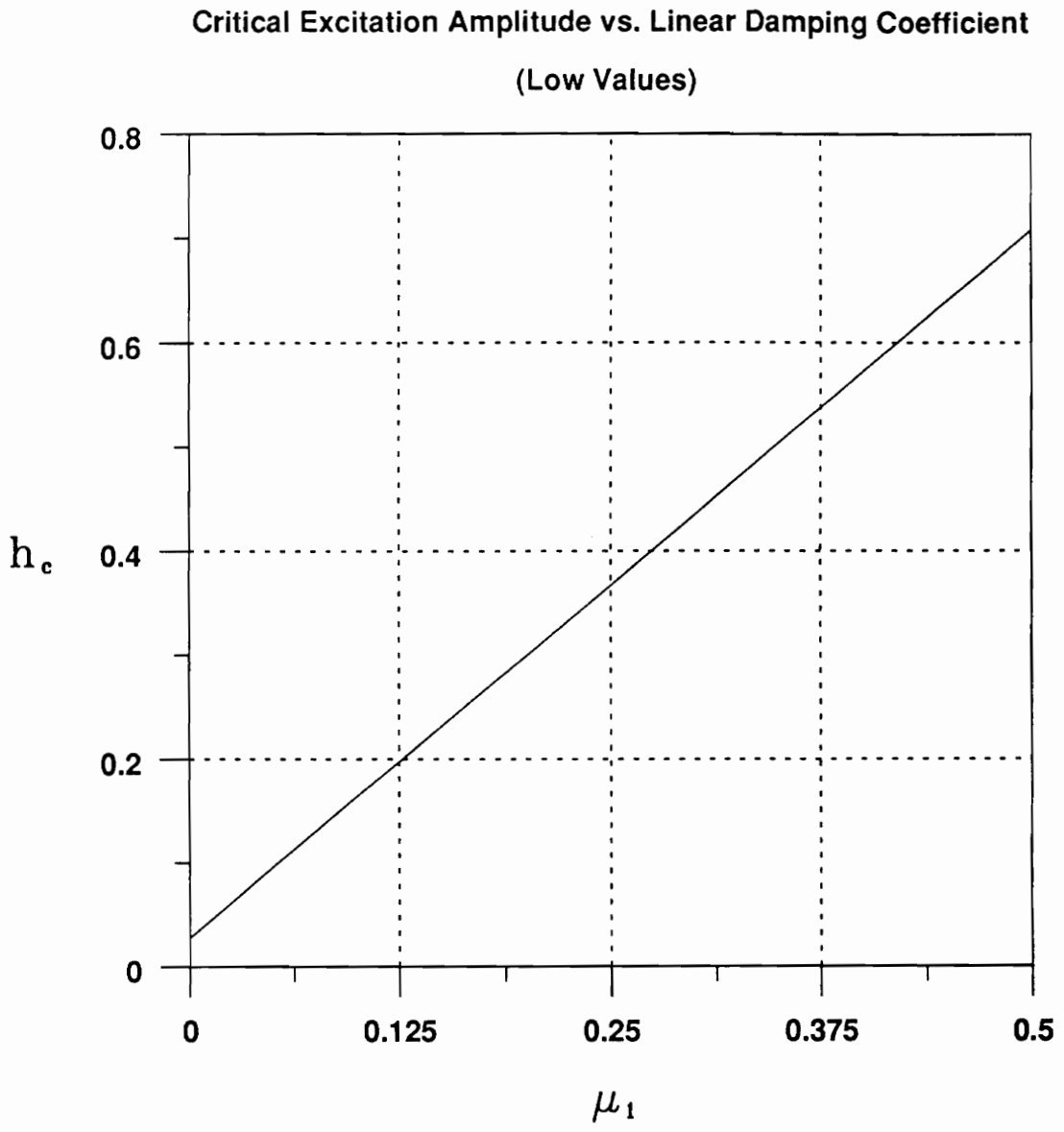

Figure 5.32. Effect of the Linear Damping Coefficient (LOW): For low values, the critical forcing level h_c is shown as a function of the linear damping coefficient while all other parameters are held constant.

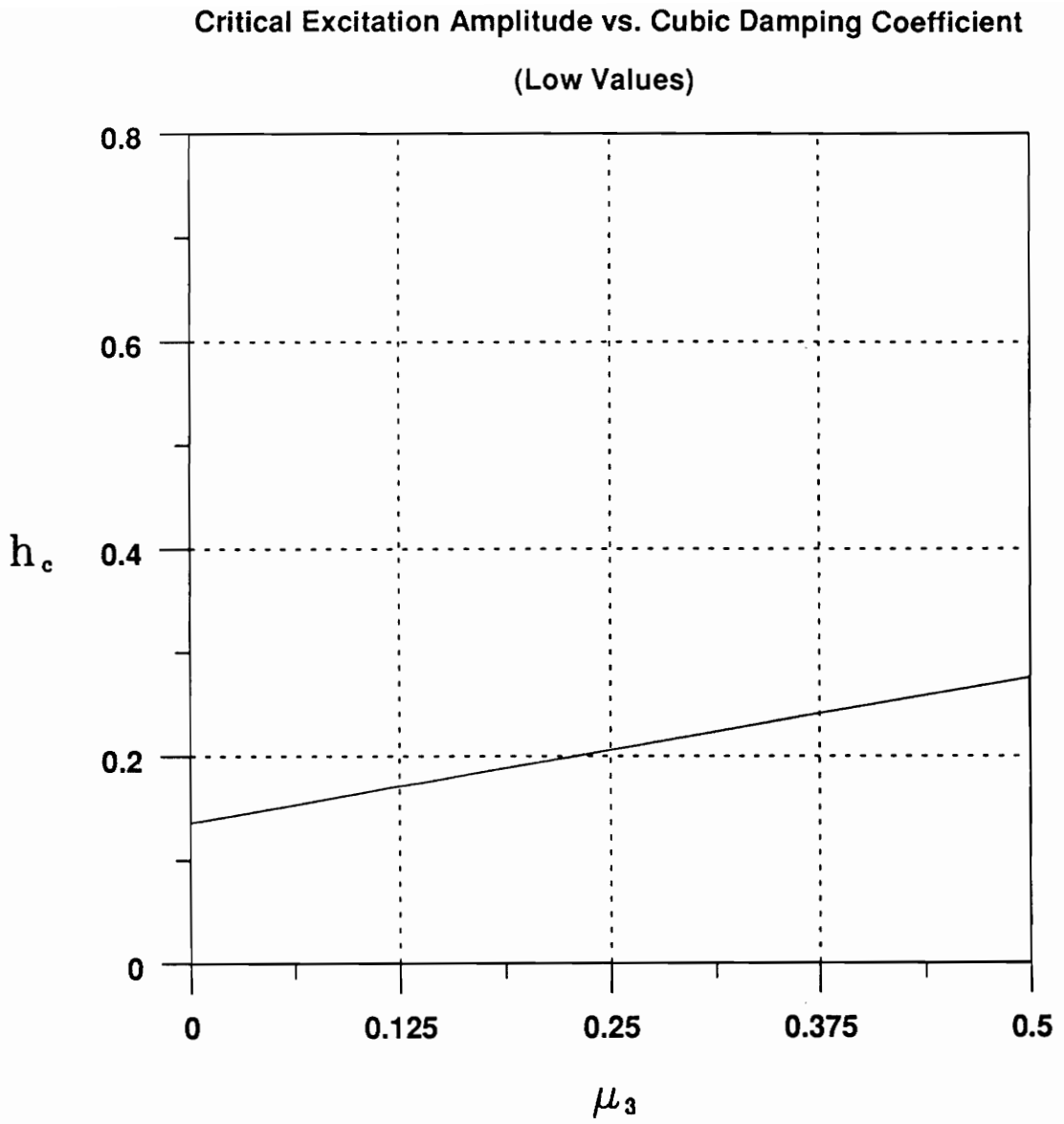

Figure 5.33. Effect of the Cubic Damping Coefficient (LOW): For low values, the critical forcing level h_c is shown as a function of the cubic damping coefficient while all other parameters are held constant.

5.2.3 High Values

Finally, a set of high parameter values is selected in a way similar to that used for selecting the low values: from the largest parameter magnitudes appearing in the plots of Section 5.2.1. The results are summarized in Figures 5.34-5.37. The pictures are qualitatively identical to the other two cases, with linear plots for the damping constants and asymptotic plots for α_3 and α_5. Predictably, the ranges for critical excitation are shifted upward compared to the other cases, probably because of the generally higher damping.

5.2.4 Verification of Parameter Study

Although we validated Melnikov's method for the base case, there is no direct evidence that the technique works for other combinations of parameter values, such as those treated in the past two sections. To this end, we examine the transient basins for both the low and high parameter sets. For each of these combinations, the transient basin should exhibit the onset of fractal areas at the appropriate excitation level. The Melnikov prediction for h_c when the equation parameters are set to the low values is 0.164. Thus, the transient basin is calculated for h values of 0.15 and 0.18; the two corresponding diagrams appear in Figures 5.38 and 5.39. As for the base case, forcing below h_c results in a continuous boundary between stable and unstable regions while an excitation larger than the critical value results in small fractal bands. For the high set of parameter values, the pattern remains the same. Melnikov's approximation for h_c is 0.738. Transient basins for h values of 0.73 and 0.77, depicted in Figures 5.40 and 5.41, respectively exhibit continuous and fractal boundaries. Although not conclusive, these graphical results indicate that Melnikov's method very likely predicts the onset of transverse manifold intersections accurately for most if not all parameter combinations in Equation [2.19]. Consequently, the parameter study in Section 5.2 can with some confidence be considered validated.

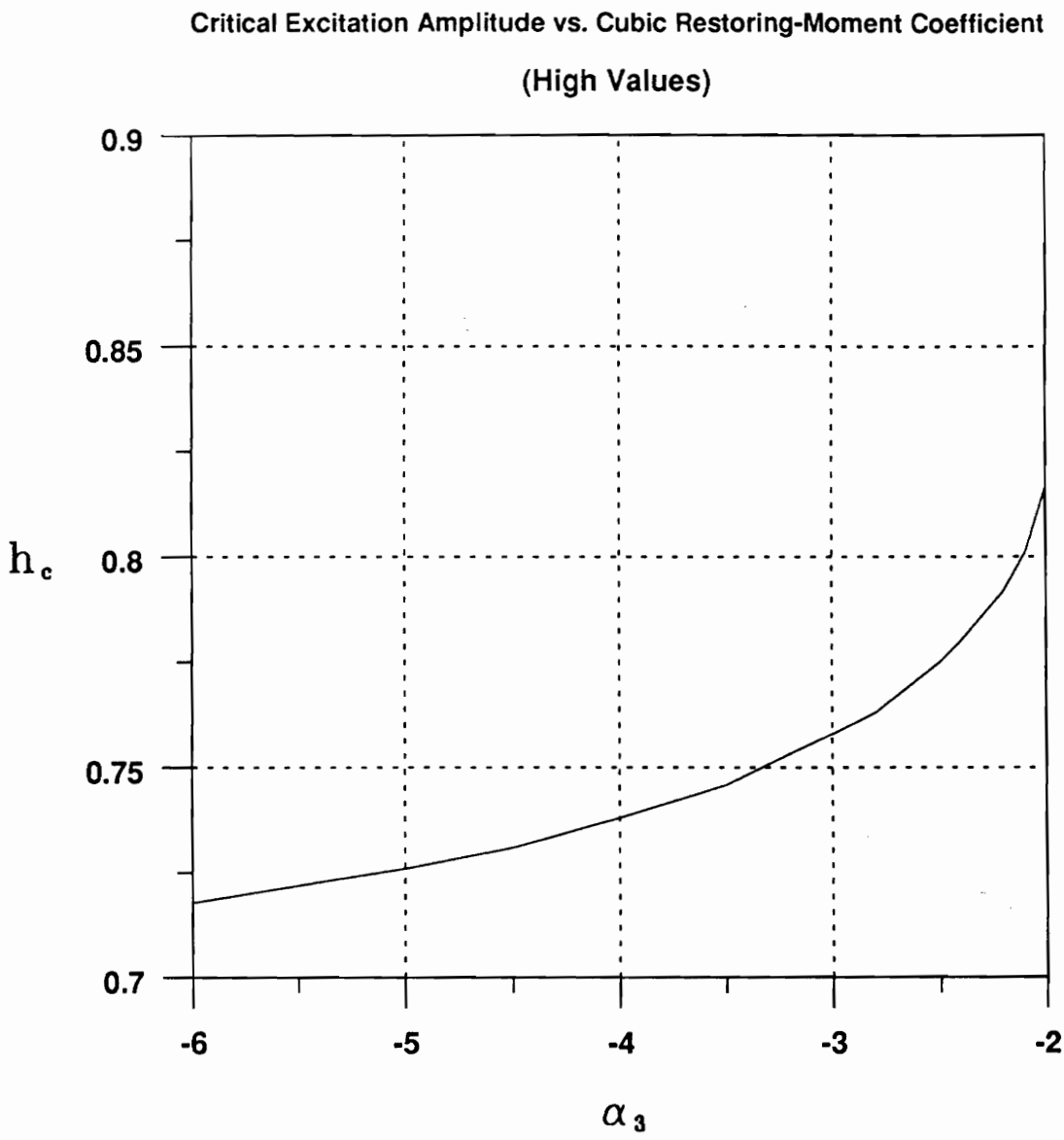

Figure 5.34. Effect of the Cubic Restoring-Moment Coefficient (HIGH): For high values, the critical forcing level h_c is shown as a function of the cubic restoring-moment coefficient while all other parameters are held constant.

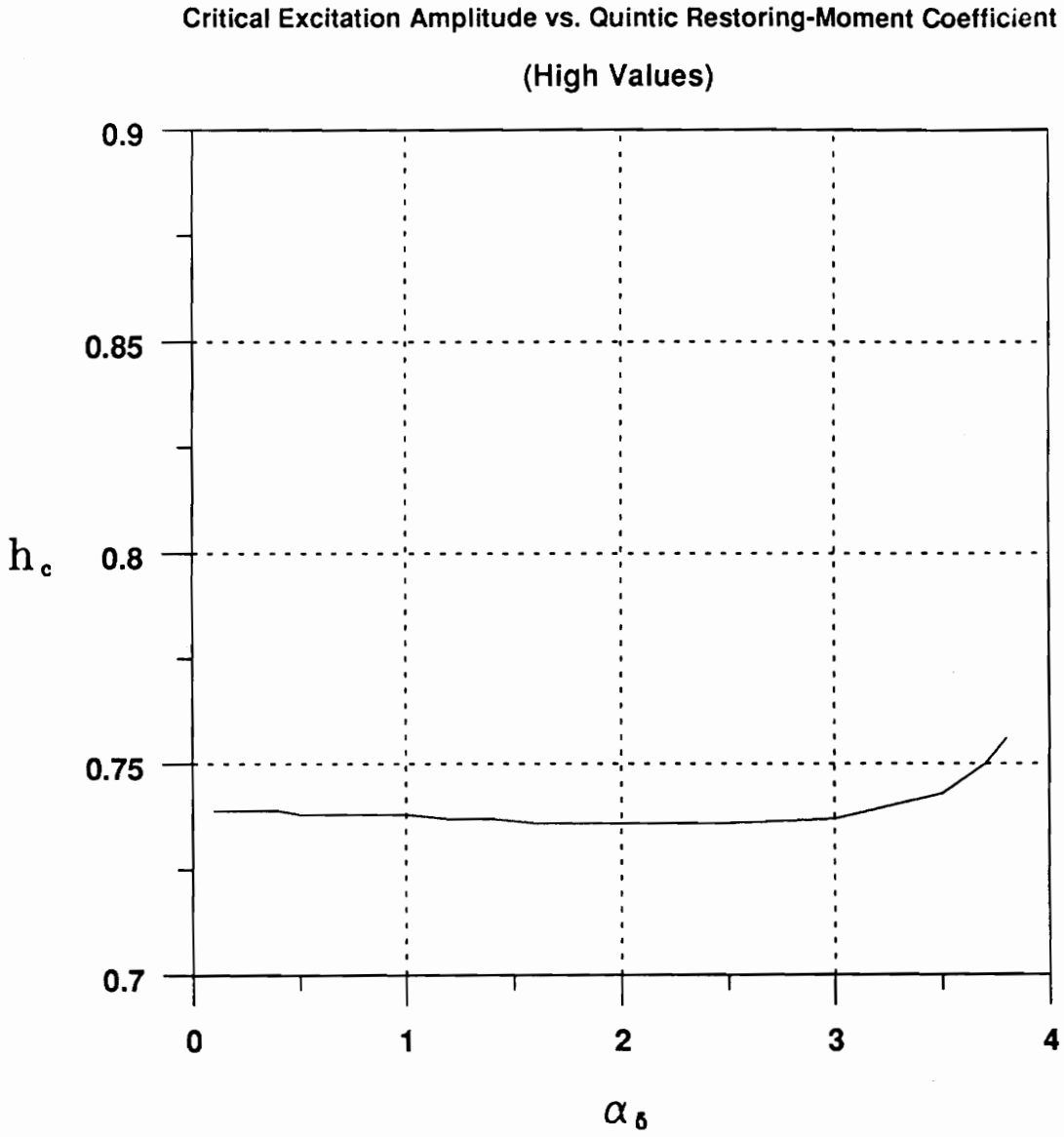

Figure 5.35. Effect of the Quintic Restoring-Moment Coefficient (HIGH): For high values, the critical forcing level h_c is shown as a function of the quintic restoring-moment coefficient while all other parameters are held constant.

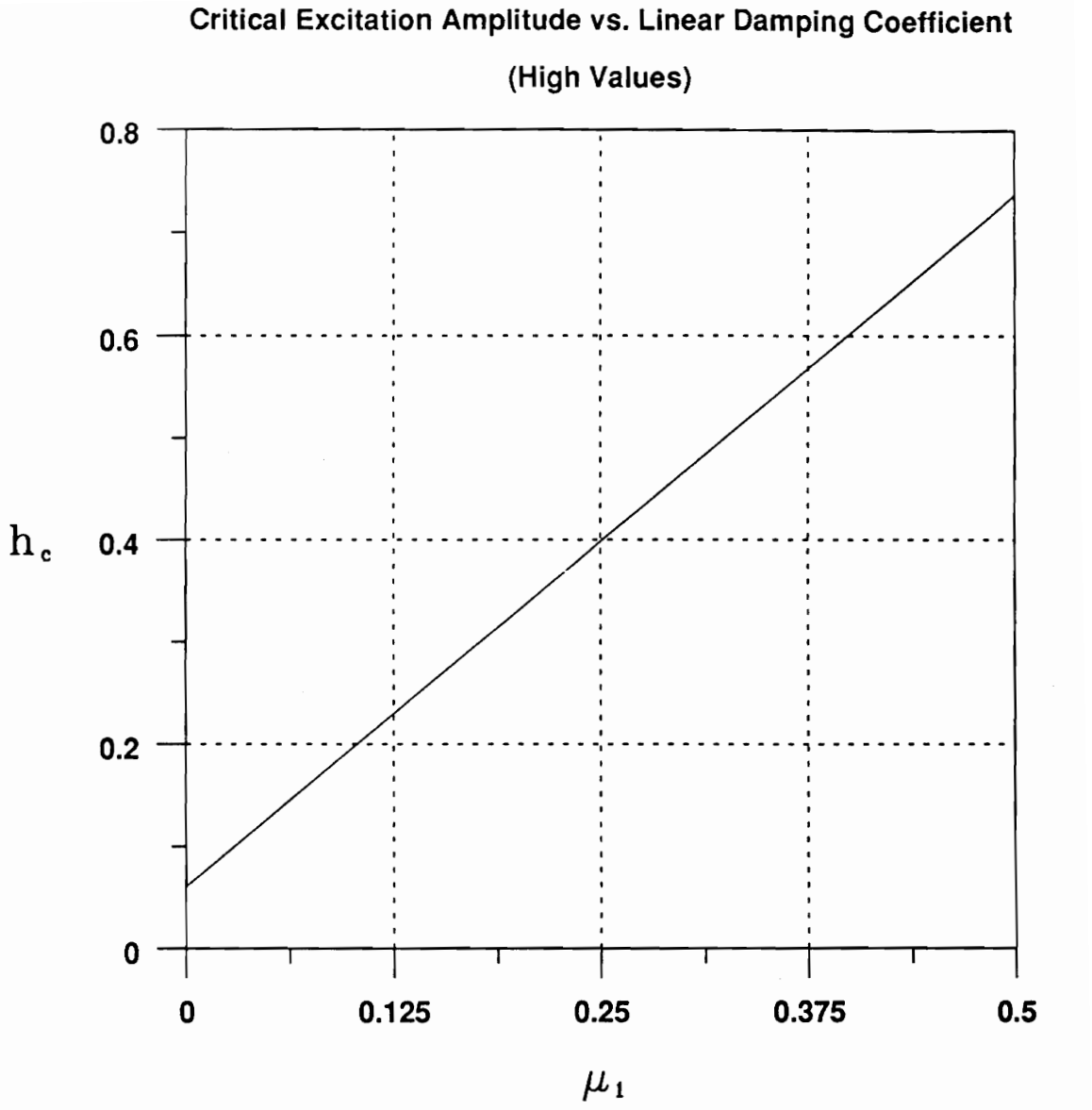

Figure 5.36. Effect of the Linear Damping Coefficient (HIGH): For high values, the critical forcing level h_c is shown as a function of the linear damping coefficient while all other parameters are held constant.

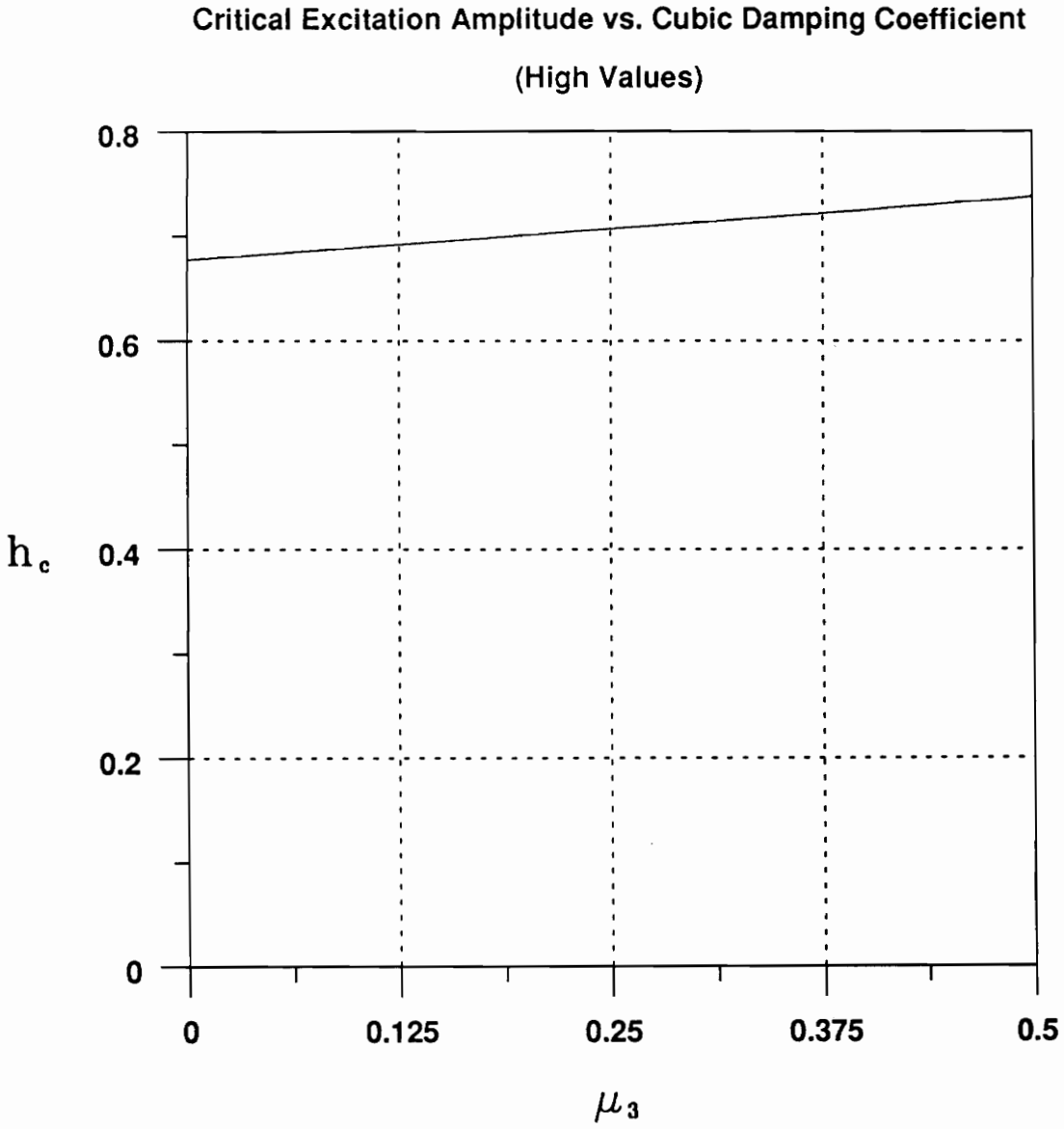

Figure 5.37. Effect of the Cubic Damping Coefficient (HIGH): For high values, the critical forcing level h_c is shown as a function of the cubic damping coefficient while all other parameters are held constant.

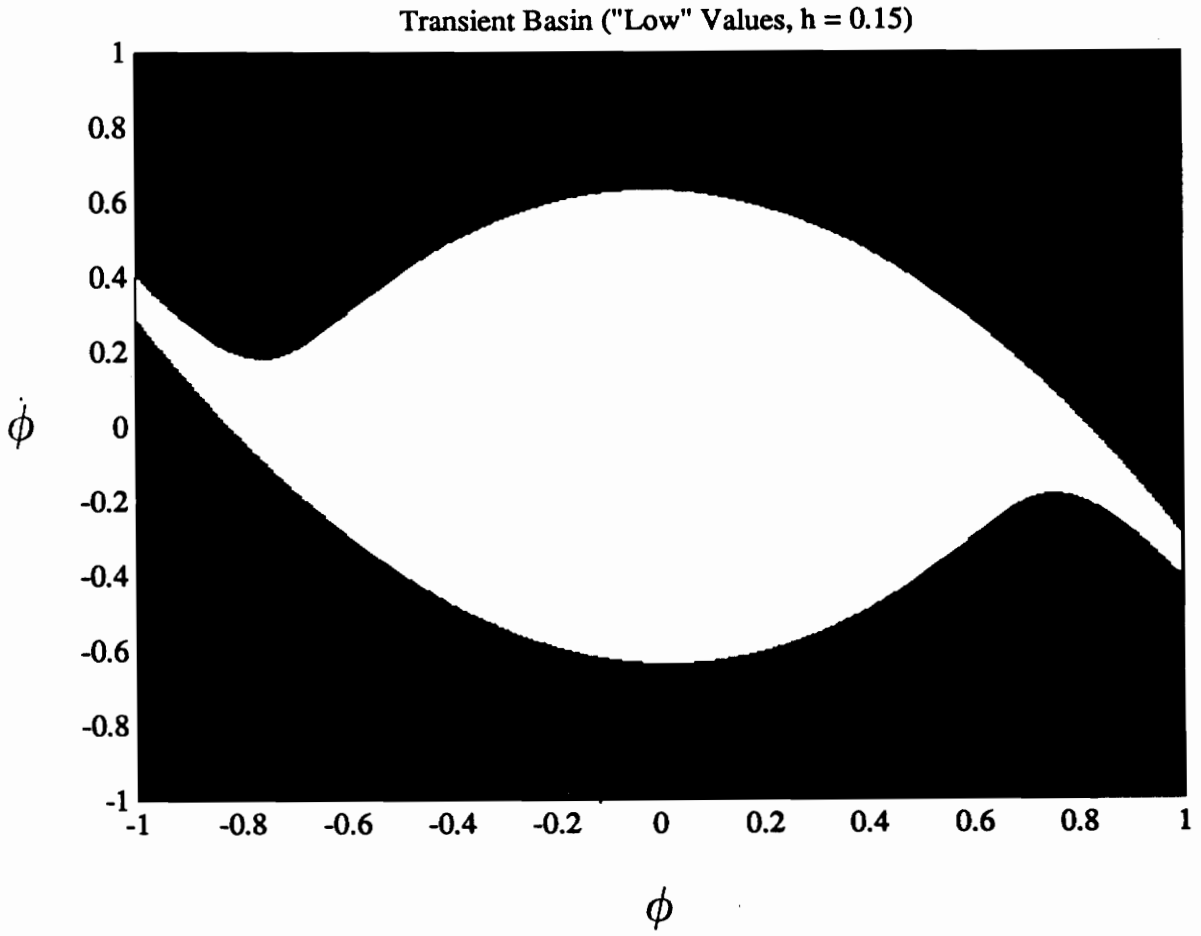

Figure 5.38. Heteroclinic Transient Basin (Low Values, h = 0.15): The transient basin prior to manifold intersections is, as for the base case, characterized by continuous boundaries.

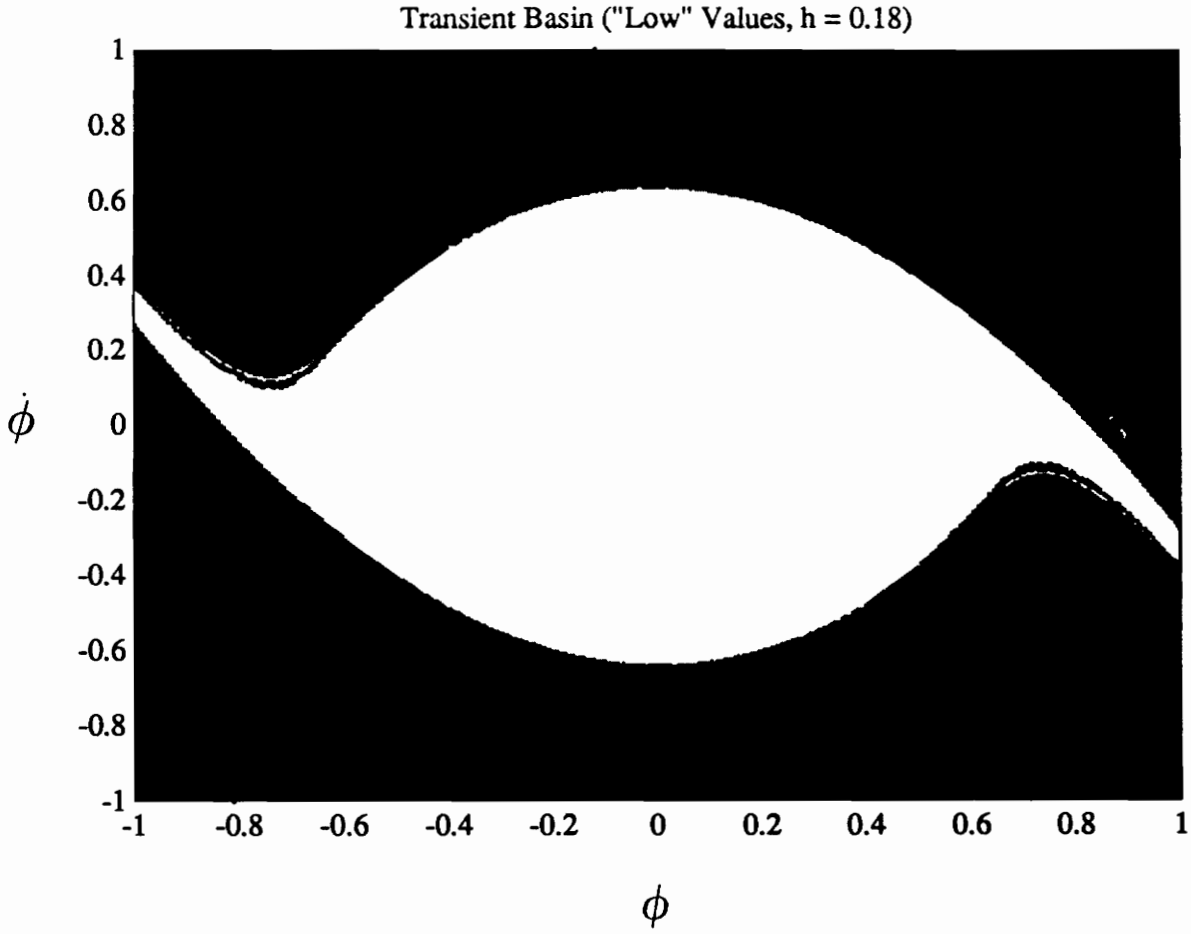

Figure 5.39. Heteroclinic Transient Basin (Low Values, h = 0.18): After the onset of manifold tangles, the transient basin for the low parameter values has small fractal bands around the safe region.

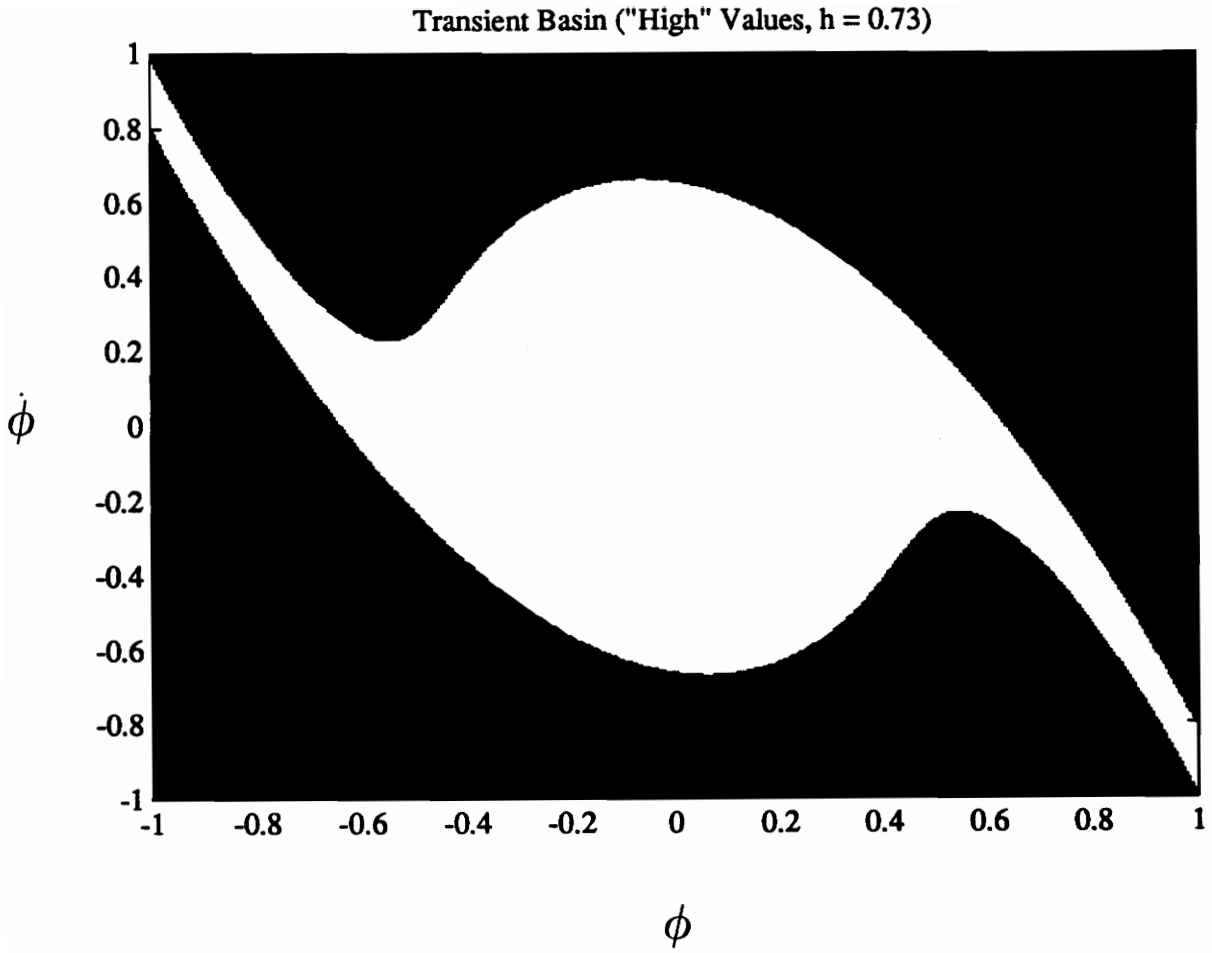

Figure 5.40. **Heteroclinic Transient Basin (High Values, h = 0.73):** Just before the manifolds intersect, the safe-unsafe boundary is again sharply defined.

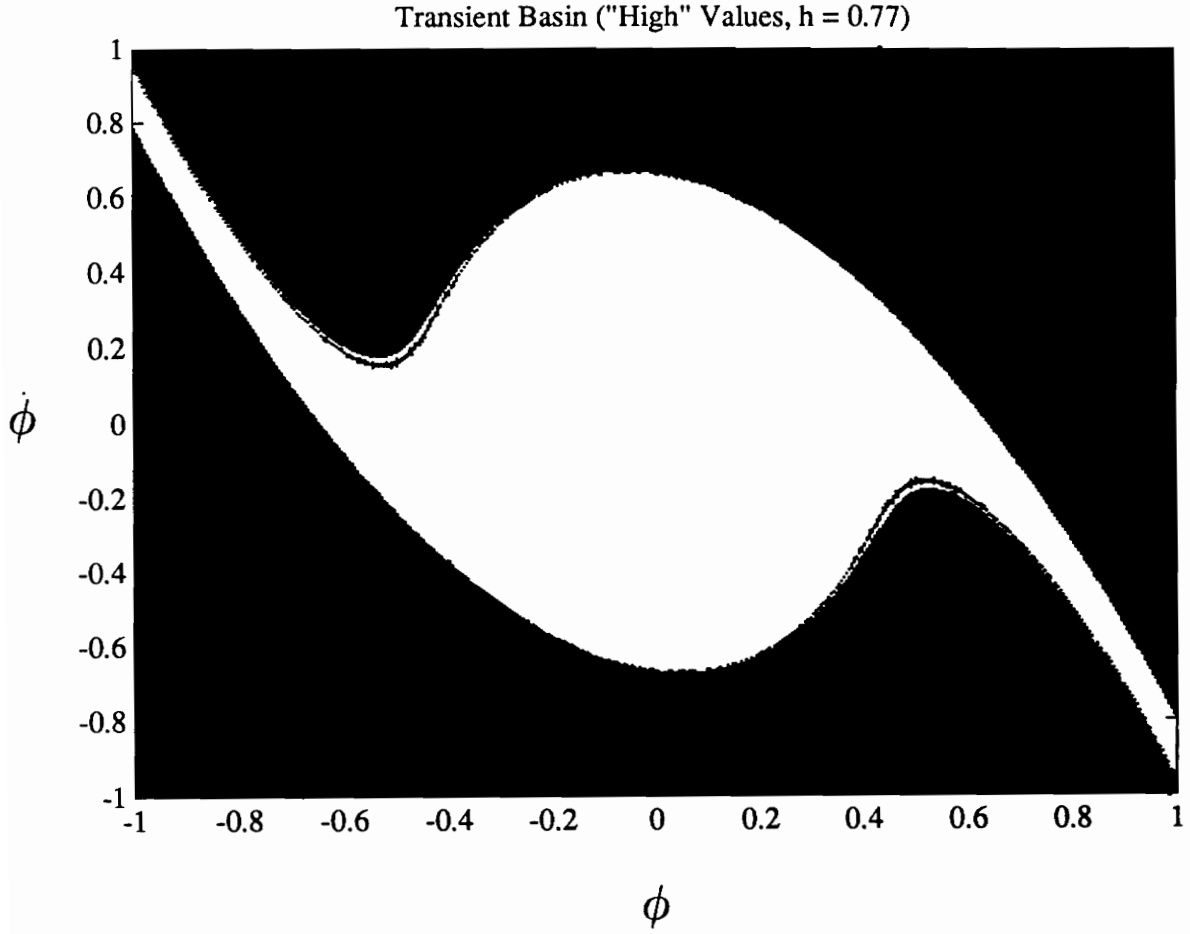

Figure 5.41. Heteroclinic Transient Basin (High Values, h = 0.77): Manifold intersections also induce fractal areas for the high parameter values.

6. Review and Conclusion

A numerical approach for using invariant manifolds and Melnikov's method to analyze a parametrically forced, single-degree-of-freedom equation modelling ship roll was developed and implemented. Computer codes were written to accurately approximate the saddle points of a Poincaré map describing the damped, forced equation and to compute the invariant manifolds of those saddles. Other numerical schemes were written to calculate Melnikov's function for predicting three types of manifold intersection: homoclinic, heteroclinic, and mixed. All of the numerical routines were applied to a ship-roll equation with an odd, quintic restoring moment, linear-plus-cubic damping, and parametric, periodic forcing. For a selected combination of parameter values (a "base case"), invariant manifolds were calculated, revealing transverse intersections. The accuracy of Melnikov's method was tested by using it to predict these intersections. Transient basins were calculated to ascertain the impact of these manifold intersections on global ship stability. Finally, a parameter study was carried out in order to ascertain how changes to the various constants in the equation affect the onset of manifold intersections as predicted by Melnikov's method.

6.1 *Results and Implications*

For the base case, it was determined that Melnikov's technique provides quite accurate estimates of the excitation amplitudes at which manifold intersections first occur. The method was used successfully to predict not only homoclinic intersections, but also heteroclinic crossings and mixed (homoclinic-heteroclinic) tangles.

However, in Chapter 5 it was discovered that only the heteroclinic intersections appear to have any predictive value regarding ship stability. The corresponding transient basins indicate that the boundary between safe and unsafe regions of phase space changes from continuous to fractal when the excitation level exceeds the critical level necessary to cause transverse manifold intersections (h_c). For the base case, the fractal behavior was confined to a small strip surrounding the safe region; no significant erosion of the safe phase space was observed. Even at excitation levels well above h_c, the safe region of the phase space (although smaller) appears only slightly affected by fractal erosion. In addition, all of these basins were symmetric with respect to the origin. The symmetry and the enduring integrity of the safe region prompted us to consider external forcing in place of the parametric term in Equation [2.19]. The transient basins for the externally forced system exhibit a drastic decrease of the safe region above the critical excitation level, indicating that the type of forcing determines the presence of significant fractal behavior. Furthermore, the basins for the external case exhibit no symmetry, supporting the conclusion that an odd form of the roll equation causes symmetric transient basins. To conclude the transient-basin analysis, we briefly examined combined external-plus-parametric excitation, noting the possibility for a greater threat to ship stability than for either type of forcing applied independently.

The parameter study, consisting of independent Melnikov analyses of both restoring-moment coefficients (α_3, α_5) and both damping coefficients (μ, μ_3), revealed some potentially valuable trends. The critical excitation level h_c was found to vary linearly with the damping coefficients, both for the base case and for two other cases. The implication of this result is that h_c varies linearly with damping for all combinations of restoring-moment parameter values. Confirmation is provided by

Bikdash, Balachandran, and Nayfeh [1992], who showed analytically that the damping terms contribute linearly to the Melnikov function. Thus, the value of critical excitation for a ship with a specified restoring-moment curve may be quickly calculated for a wide range of damping functions after only two computations of the Melnikov function, which are necessary to define the linear relationship.

In contrast, the dependence of h_c on each of the restoring-moment coefficients is asymptotic in nature. As explained in the last chapter, the critical excitation amplitude remains near a limiting value when either of the restoring-moment coefficients is varied in a neighborhood far from the value which would make an equality of Equation [5.7]. This behavior is not as quantitatively useful as the linear relationships exhibited with the damping coefficients. Yet the fact that h_c remains nearly constant over large intervals of α_3 and α_5 is helpful qualitatively: no large deviations from a single calculated value are likely.

Although we noted that no catastrophic erosion of the safe area occurs for the parametrically forced system, the h_c values available from a parameter study like the one in Section 5.2 may be useful as upper bounds on acceptable forcing amplitudes for ship operation. At excitation levels above h_c, the safe region decreases in size, but in a more predictable and less catastrophic fashion. Nevertheless, such a value might be useful as a loose criterion for safe dynamic operation in the presence of parametric excitation.

In concluding this section, we review the primary contributions of this research. First, a workable algorithm was developed to accurately locate the saddle points of a Poincaré map associated with a dynamically forced system, a problem of surprising difficulty that must be solved before computing the accompanying invariant manifolds. The algorithm is not limited to the ship-roll equation, but may be applied to any two-dimensional Poincaré map. Second, the validity of Melnikov's method was established for predicting nascent transverse manifold intersections, including homoclinic, heteroclinic, and mixed homoclinic-heteroclinic tangles, yielding an approximate upper bound for safe ship operation in the presence of parametric excitation. Third, various transient basins describing the parametric ship-roll model were used to characterize Equation [2.19]: for even large amplitudes of excitation, the safe region remains essentially

unaffected by fractal erosion. A brief comparison with an externally forced equation strongly suggests that external forcing is necessary to cause catastrophic erosion of the safe area. Finally, a parameter study revealed the dependence of the critical parametric excitation level h_c on four of the system parameters.

6.2 *Recommendations for Further Study*

With regard to the specific techniques used in this thesis, several suggestions for improvement come to mind. The search algorithm for approximating the saddle points, although generally effective, is tedious to implement. Because the programmer must adjust several parameters iteratively, the code cannot be run independently, but must be continually monitored until success is achieved. Perhaps a more robust algorithm can be developed, or the existing one made more reliable and/or efficient. Such an accomplishment would greatly facilitate the computation of the invariant manifolds of the saddle points in a discrete map (e.g., a Poincaré map) and would probably be of considerable interest to mathematicians as well as dynamicists. Another recommendation is that the mixed Melnikov function be more rigorously tested. For the parametrically forced ship-roll problem, the physical significance of mixed tangles is lacking; application of the technique to a three-well potential system for which homoclinic-heteroclinic intersections are meaningful would provide a suitable medium for evaluating the mixed Melnikov prediction. Finally, the trends observed in the transient basins of the parametrically forced ship-roll model may be subject to the length of integration or the definition of stability. Various combinations of these parameters should be examined with the intent of verifying the results presented here.

While these specific enhancements will be helpful, the general single-degree-of-freedom model for ship roll (Equation [2.18]) should be more thoroughly evaluated. The one transient basin computed for combined external-plus-parametric forcing indicates the potential for a wealth of

significant dynamics. Further, the conditions for which the single-equation model is valid can be more rigorously established with the aid of more research. Specifically, experimental studies could be utilized to test the adequacy of the polynomial approximations to the restoring moment and the damping. Additional experiments could be designed to improve the mathematical modelling of the forcing function and to determine when the other degrees of freedom cannot be ignored.

References

1. Abkowitz, M.A., "Lectures on Ship Hydrodynamics, Steering, and Maneuverability," Hydrodynamics Department, Hydro-og Aerodynamisk Laboratorium, Lyngby, Denmark, 1964.

2. Arrowsmith, D.K. and Place, C.M., **An Introduction to Dynamical Systems**, Cambridge University Press, 1990, Chapter 3.

3. Avriel, M., **Nonlinear Programming: Analysis and Methods**, Prentice-Hall, 1976, Chapter 9.

4. Bikdash, M., Balachandran, B., and Nayfeh, A., "Melnikov Analysis for a Ship with a General Roll-Damping Model," submitted for publication, 1992.

5. Blagoveshchensky, S.N., **Theory of Ship Motions**, Dover Publications, 1962.

6. Blocki, W., "Ship Safety in Connection with Parametric Resonance of the Roll," *International Shipbuilding Progress*, Vol. 27, 1980, p. 36.

7. Falzarano, J.M., *Predicting Complicated Dynamics Leading to Vessel Capsizing*, Ph.D. Dissertation at The University of Michigan, Department of Naval Architecture and Marine Engineering, 1990.

8. Falzarano, J.M. and Troesch, A.W., "Application of Modern Geometric Methods for Dynamical Systems to the Problem of Vessel Capsizing with Water-on-deck," *Fourth International Conference on the Stability of Ships and Ocean Vehicles*, Naples, Italy, September 1990.

9. Féat, G. and Jones, D., "Parametric Excitation and the Stability of a Ship Subjected to a Steady Heeling Moment," *International Shipbuilding Progress*, Vol. 28, 1981, p. 263.

10. Froude, W., "On the Rolling of Ships," *Transactions of the Institution of Naval Architects*, Vol. 2, 1861, p. 180.

11. Haddara, M.R., "A Note on the Effect of Damping Moment Form on Moment Response," *International Shipbuilding Progress*, Vol. 31, 1984, p. 285.

12. IMSL Math/Library, **FORTRAN Subroutines for Mathematical Applications**, Vol. 2, 1989, p. 633.

13. Kane, T.R., Likins, P.W., and Levinson, D.A., **Spacecraft Dynamics**, McGraw-Hill, 1983, Appendices I and II.

14. Li, G.X. and Moon, F.C., "Criteria for Chaos of a Three-Well Potential Oscillator with Homoclinic and Heteroclinic Orbits," *Journal of Sound and Vibration*, Vol. 136, 1990, p. 17.

15. Melnikov, V.K., "On the Stability of the Center for Time Periodic Perturbations," *Transactions of the Moscow Mathematical Society*, Vol. 12, 1963, p. 1.

16. Moser, J., **Stable and Random Motions in Dynamical Systems**, Princeton University Press, 1973.

17. Myrhaug, D., "A Note on the Effect of Roughness on the Frictional Roll Damping," *International Shipbuilding Progress*, Vol. 28, 1981, p. 128.

18. Nayfeh, A.H. and Khdeir, A.A., "Nonlinear Rolling of Ships in Regular Beam Seas," *International Shipbuilding Progress*, Vol. 33, 1986a, p. 40.

19. Nayfeh, A.H. and Khdeir, A.A., "Nonlinear Rolling of Biased Ships in Regular Beam Waves," *International Shipbuilding Progress*, Vol. 33, 1986b, p. 84.

20. Parker, T.S., and Chua, L.O., **Practical Numerical Algorithms for Chaotic Systems**, Springer-Verlag New York, 1989, Chapter 6.

21. Paulling, J.R., "The Transverse Stability of a Ship in a Longitudinal Seaway," *SNAME Journal of Ship Research*, March 1961, p. 37.

22. Paulling, J.R., Kastner, S., and Schaffran, S., "Experimental Studies of Capsizing of Intact Ships in Heavy Seas," Department of Transportation, National Technical Information Service, 1972.

23. Paulling, J.R. and Rosenberg, R.M., "On Unstable Ship Motions Resulting from Nonlinear Coupling," *SNAME Journal of Ship Research*, June 1959, p. 36.

24. Rawson, K.J. and Tupper, E.C., **Basic Ship Theory**, Longman Group Ltd., 1976, Chapter 2.

25. Roberts, J.B., "Effect of Parametric Excitation on Ship Rolling Motion in Random Waves," *Journal of Ship Research*, Vol. 26, 1982, p. 246.

26. Sánchez, N.E., *Stability of Nonlinear Oscillatory Systems with Application to Ship Dynamics*, Ph.D. Dissertation at Virginia Polytechnic Institute and State University, Department of Engineering Mechanics, 1989.

27. Sánchez, N.E. and Nayfeh, A.H., "Nonlinear Rolling Motions of Ships in Longitudinal Waves," *International Shipbuilding Progress*, Vol. 37, 1990, p. 247.

28. Thompson, J.M.T.,"Transient Basins: A New Tool for Designing Ships Against Capsize," *Dynamics of Marine Vehicles and Structures in Waves*, 1991, p. 325.

29. Thompson, J.M.T, Rainey, R.C.T., and Soliman, M.S., "Ship Stability Criteria Based on Chaotic Transients from Incursive Fractals," *Philosophical Transactions of the Royal Society of London*, Vol. 332, 1990, p. 149.

30. Tondl, A. and Nabergoj, R., "Model Simulation of Parametrically Excited Ship Rolling," *Nonlinear Dynamics*, Vol. 1, 1990, p. 131.

31. Wiggins, S., **Introduction to Applied Nonlinear Dynamical Systems and Chaos**, Springer-Verlag New York, 1990.

32. Wright, J.H.G. and Marshfield, W.B., "Ship Roll Response and Capsize Behaviour in Beam Seas," *Transactions of the Royal Institute of Naval Architects*, Vol. 122, 1980, p. 129.

Appendix A. Saddle-Point Algorithm: Pseudo-Code

The following pseudo-code parallels the description in Section 3.3.2 of the algorithm for approximating the saddle points of a Poincaré map. Although not intended to be complete, the pseudo-code illustrates the essential elements of the code used in this work. The main program is no more than a control structure; the important facets of the algorithm are contained in the subroutines. The routine ITERATE applies the Hooke-Jeeves search algorithm to random guesses in order to identify the necessary saddle approximations. INLTZ serves only to give initial values to some crucial variables, while HJ contains the main steps in the Hooke-Jeeves search. For reference, the notation "()" indicates a vector quantity; in this case, all vectors are one-dimensional with 2 components.

The algorithm was implemented on an Apollo 10000 workstation.

Main Program

set $\alpha_3, \alpha_5, \mu_1, \mu_3, \omega_0, \Omega, T, h$ to selected values

for each saddle point:

$\underline{x}_t \leftarrow$ linearized approximation

for $\varepsilon = 0,1,\text{step}$

call ITERATE (subroutine that implements the Hooke-Jeeves search)

end for

write the saddle approximations to a file

end for

Subroutine ITERATE

```
call INTLZ (initializes variables)
CNTR() ← x_c (locate center of box)
while # of random guesses < max. allowable # of guesses (to be input to the HJ routine)
1       reinitialize some variables (for the next call of HJ)
        while # of exploratory-move pattern-move sequences < max allowable #
                # sequences = # sequences + 1
2               call HJ (returns an acceptable new base point T2())
                if Δ is too small, reset it and start over at 1 with a new random guess
                if F(T2()) < F(CNTR()) then CNTR() ← T2()
                if F(T2()) < tolerance then
                        if ε < > 1 then use T2() as initial guess for the next value of ε and return
                        if ε = 1 then
                                compute the eigenvectors of the Jacobian J(T2())
                                compute Δη1, Δη2 of P(T2()) - T2()
                        end if
                        if T2() is an acceptable saddle approximation then
                                if all saddles are found then return
                                otherwise, go to 2, reset variables, and search for the others
                        end if
                        reset # sequences to 0
                end if
                go to 2
        end while
        reset # sequences to 0
```

```
        pick a new random guess inside box
end while
```

Subroutine INTLZ

set # sequences to 0

assign initial values to

box size

initial step size Δ

first base point BASE() used by HJ (set to $\underline{x}_t$)

center of box CNTR() (set also to $\underline{x}_t$)

tolerance for convergence of the Hooke-Jeeves search

compute $P(\underline{x}_t)$

old base point OBASE() $\leftarrow \underline{x}_t$ (used in HJ)

old distance DOLD $\leftarrow \|P(\underline{x}_t) - \underline{x}_t\|$ (used in HJ)

Subroutine HJ

input the point INIT() (the result of the last pattern move OR the next random guess)

define the vectors $\Delta_1()$, $\Delta_2()$ to be $(\Delta,0)$ and $(0,\Delta)$

compute P(INIT()), P(INIT() + $\Delta_1()$)

compute DPTRN = distance btwn. INIT() and its iterate under P

compute DPLUS1 = distance btwn. INIT() + $\Delta_1()$ and its iterate under P

if DPLUS1 < DPTRN then

$t^h() = INIT() + \Delta_1()$

DT1 = DPLUS1

else

compute P(INIT() - $\Delta_1()$)

compute DMNUS1 = distance btwn. INIT() - $\Delta_1()$ and its iterate under P

if DMNUS1 < DPTRN then

$t^h() = INIT() - \Delta_1$

DT1 = DMNUS1

else

$t^h() = INIT()$

DT1 = DPTRN

end if

end if

compute $P(t^h() + \Delta_2())$

compute DPLUS2 = distance btwn. $t^h() + \Delta_2()$ and its iterate under P

if DPLUS2 < DT1 then

$T2() = t_h() + \Delta_2()$

DT2 = DPLUS2

else

compute $P(t_h() - \Delta_2())$

compute DMNUS2 = distance btwn. $t_h() - \Delta_2()$ and its iterate under P

if DMNUS2 < DT1 then

T2() = $t_h() - \Delta_2$

DT2 = DMNUS2

else

T2() = $t_h()$

DT2 = DT1

end if

end if

if the exploratory-move sequence failed, then reduce Δ and start over

if the new base point has a higher F than the previous one, start over from the old base point

make a pattern move: INIT() = BASE() + (BASE() - OBASE())

OBASE() ← BASE()

DOLD ← DPTRN

Vita

Marc Alan Kreider was born in Wilmington, Delaware on March 1, 1968. After graduating from Archmere Academy in Claymont, Delaware in 1986, he matriculated at Virginia Polytechnic Institute and State University, earning a Bachelor of Science in Engineering Science and Mechanics in May 1990. He continued to study mechanics at Virginia Tech by pursuing a Master of Science in the same department.